

Ιατρική Σχολή Πανεπιστημίου Κρήτης  
Εργαστήριο Ιατρικής Απεικόνισης  
Εργαστήριο Υπολογιστικής Ιατρικής, ΙΤΕ

## Διδακτορική Διατριβή

*Πολυπαραμετρική ανάλυση των ποσοτικών δεικτών  
διαφορετικών μη συμβατικών τεχνικών μαγνητικής  
τομογραφίας στη μελέτη των ασθενών με σκλήρυνση κατά  
πλάκας και κλινικά μεμονωμένο σύνδρομο*

**ΚΟΝΤΟΠΟΔΗΣ ΕΛΕΥΘΕΡΙΟΣ**

Ηράκλειο 2020

*Επιβλέπουσα: Παπαδάκη Ευφροσύνη*

*Συνεπιβλέπων 1: Μαριάς Κώστας*

*Συνεπιβλέπων 2: Ζαγανάς Ιωάννης*



Medical School, University of Crete  
Medical Imaging Department  
Computational Bio-Medicine Laboratory, FORTH

## Doctoral Thesis

*Multi-parametric analysis of quantitative indexes, using different non-conventional MRI techniques in a study related to patients with Multiple Sclerosis and Clinically Isolated Syndrome*

**KONTOPODIS ELEFThERIOS**

Heraklion 2020

*Supervisor: Papadaki Efrosini*

*Co-supervisor 1: Marias Kostas*

*Co-supervisor 2: Zaganas Ioannis*



## **Acknowledgments**

This research thesis was carried out in the Medical Imaging department, Medical School of the University of Crete as well as in the Computational Bio-Medicine Laboratory, Institute of Computer Science of foundation of Research and Technology of Heraklion. Furthermore, this work was supported by the Hellenic Foundation for Research and Innovation (HFRI) and the General Secretariat for Research and Technology (GSRT), under the HFRI PhD Fellowship grant (GA. no. 130189/I2/31-7-2017).

I would like to thank my supervisors Prof. Efrosini Papadaki, Prof. Kostas Marias and Prof. Ioannis Zaganas for their guidance and their support during all these years. Their scientific contribution was a significant factor towards the completion of this thesis. I would like also to thank Prof. Thomas Maris, Prof. Apostolos Karantans, Prof. Akis Simos and Prof. Panayiotis Mitsias for their insightful comments and encouragement.

Many thanks to my colleagues from the Computational Bio-Medicine Laboratory, FORTH, Georgios Manikis, Katerina Nikiforaki, Karatzanis Ioannis, Ioannidis Giorgos, Giannakakis Giorgos, Papadakis Giorgos and Spanakis Kostas for the fruitful scientific collaborations we had, for their support and discussions on issues raised.

Finally, I would like to thank my family and my friends for their continuous support all these years.

## Contents

Abstract .....	7
Περίληψη.....	11
Part A: Theoretical Background.....	16
1 Introduction.....	16
2 MULTIPLE SCLEROSIS.....	17
2.1 Epidemiology.....	17
2.2 Pathogenesis .....	18
2.3 Clinical manifestations .....	21
2.3.1 Clinical symptoms.....	23
2.3.2 Diagnosis of multiple sclerosis .....	23
2.3.3 Quantitative assessment of the clinical disability .....	24
2.4 MS Pathology.....	25
2.4.1 The Active lesion.....	26
2.4.2 Mechanisms of axonal loss.....	26
2.4.3 Pathological Heterogeneity in lesions .....	27
2.4.4 Chronic Lesions.....	28
2.4.5 Remyelination.....	28
2.4.6 Grey Matter involvement.....	28
2.5 The Blood Brain Barrier (BBB) .....	28
2.5.1 Transport across the BBB .....	32
2.5.2 Pathological BBB disruption in MS .....	32
3 Conventional MR imaging in MS .....	35
3.1 T1 sequences in MS.....	37
3.2 Using T2 sequences .....	39
3.3 Contrast Enhanced lesions .....	40
4 Contribution of MRI in the Diagnosis of MS.....	44
5 Perfusion Imaging in MS.....	48
5.1 DSC-Perfusion MRI .....	48
5.2 DCE perfusion MRI.....	53
6 Pharmacokinetic (PK) analysis of perfusion MRI studies .....	60
6.1 Reliability of pharmacokinetic (PK) biomarkers .....	61
6.2 Estimation of contrast agent concentration .....	62
6.3 Arterial Input Function (AIF).....	63
6.4 Quantitative Models.....	66
6.4.1 Tofts (TM) and Extended Tofts Model (ETM).....	69

6.4.2 Adiabatic Tissue Homogeneity Model (ATH).....	70
6.4.3 Two Compartment Exchange Model (2CXM).....	70
6.4.4 Distributed-Capillary Adiabatic Tissue Homogeneity Model (DCATH).....	71
6.4.5 Gamma Capillary Transit Time model (GCTT) .....	72
6.5 Model Free Analysis .....	73
6.6 Conclusion .....	75
7 Research motivation and thesis goals .....	76
Part B: Disease oriented research methodology and clinical application.....	79
8 PK quantitative analysis for clinical research .....	80
8.1 DCE–MRI quantification .....	80
8.1.1 Data Preparation .....	81
8.1.2 Signal to Contrast Conversion .....	86
8.1.3 Arterial Input Function .....	87
8.1.4 Models.....	89
8.2 Visualization .....	90
9 Testing our computational tools for predicting tumor treatment response outcome .....	92
9.1 Materials and Methods .....	93
9.1.1 Patient and protocol information.....	93
9.1.2 Image analysis methods .....	94
9.1.3 Statistical and predictive analysis.....	96
9.2 Results .....	98
9.3 Discussion .....	102
9.4 Conclusion .....	103
10 Extended-time perfusion protocol (SNAPS) and assessment of permeability in MS lesions .....	104
10.1 Materials and Methods .....	104
10.1.1 Patient information and Imaging protocol.....	104
10.1.2 PK models .....	108
10.1.3 Statistical Analysis .....	109
10.2 Results .....	110
10.3 Discussion .....	114
10.4 Conclusion .....	119
11 Application of DCE perfusion MRI in CIS and MS patients and correlation of PK parameters with neuropsychiatric measures. ....	120
11.1 Introduction.....	120
11.2 Methods .....	122

11.2.1 Participants.....	122
11.2.2 Neuropsychological assessment.....	124
11.2.3 Scanning and data processing .....	125
11.3 Results .....	128
11.3.1 Neuropsychiatric status of patients with CIS and RR-MS.....	128
11.3.2 k-Trans and vp in lesions vs NAWM using the Snap as compared to the NoSnap method .....	129
11.3.3 Comparison of clinical groups on k-trans and vp .....	131
11.3.4 K-trans and vp as a function of lesion type .....	132
11.3.5 Clinical correlates of k-trans and vp values in NAWM .....	134
11.3.6 Neuropsychiatric status as a function of k-trans values in NAWM.....	135
11.4 Discussion .....	138
11.5 Conclusion .....	140
12 Correlation of T1 (DCE) with T2* (DSC) perfusion parameters .....	142
12.1 Introduction.....	142
12.2 Methods .....	143
12.3 Results .....	144
12.4 Discussion .....	149
12.5 Conclusion .....	150
13 Added value and future work.....	151
REFERENCES .....	153

## Abstract

Multiple Sclerosis (MS) is a chronic inflammatory demyelinating disease of the central nervous system (CNS), commonly affecting young adults. Although the etiology of MS is largely unknown, it is considered primarily an autoimmune disease, in which activated myelin-specific T-cells migrate from the periphery to the CNS, by crossing the blood brain barrier (BBB), and induce inflammatory demyelinating lesions. Recent studies, involving the quantitative analysis of perfusion MRI data, emphasized the crucial role of BBB dysfunction in the pathogenesis of MS. However, the quality of perfusion MR imaging data and post-processing techniques highly influence the accuracy and precision of the derived quantitative maps. As a result, design of imaging protocols and analysis methods dedicated to the needs of specific pathologies are of great importance in clinical practice.

The main objective of this dissertation is to provide a robust research methodology for applying MR perfusion protocols in MS and CIS patients. For this purpose, the following research methodology was developed:

- 1) A novel Dynamic Contrast Enhanced (DCE) T1 perfusion MRI protocol was designed. This novel protocol tripled the time of perfusion observation, by minimally extending the MR acquisition time. Due to the extra cost for a commercial Pharmacokinetic (PK) analysis software and the inability to modify the existing computational platforms to process newly developed protocols, an in-house PK analysis computational tool was also developed.

- 2) The in-house computational software was validated in a cohort with breast cancer, by predicting the therapy outcome at baseline and in the early stages of

treatment. Results indicated that the aforementioned quantitative analysis software platform was able to predict the neoadjuvant chemotherapy (NAC) response at baseline and in the early treatment stages. The best pathological complete response (pCR) predictors at first follow-up, achieving high AUC and sensitivity and specificity more than 50%, was the median value of transfer constant from extracellular - extravascular space (EES) to the plasma space,  $k_{ep}$  (AUC 73.4%), while the 80th percentile of the fractional volume of EES,  $v_e$ , achieved the highest pCR prediction at baseline with AUC 78.5%.

3) Both the novel time extended (Snaps) and the conventional Dynamic Contrast Enhanced (DCE) protocols were applied in a cohort of MS patients to investigate several protocol and PK analysis factors for the accurate quantification of active demyelinating lesions. According to the results of these studies, Snaps protocol achieved better quantification of the active lesions, by detecting 49% more enhancing pixels on average, compared to the conventional DCE protocol. Furthermore, through an extensive comparative analysis it was demonstrated that extended Tofts model (ETM) was the best PK model for active MS and CIS lesion quantification.

4) The novel time extended and the conventional DCE protocol, were applied in a cohort of MS and CIS patients to quantify PK parameters, such as the volume transfer constant from plasma space to EES ( $k_{trans}$ ) and the fractional volume of vascular space ( $v_p$ ) values, of NAWM areas and demyelinating lesions. The PK parameters stemming from the proposed time extended protocol, achieved more accurate characterization of the different lesion types, and better discrimination from NAWM compared to the conventional DCE protocol.

5) Although cognitive impairment is common in MS its underlying pathophysiology is largely unknown, while conventional MRI techniques do not provide strong correlations with clinical variables or neuropsychological deficits. For this purpose, this dissertation examined the correlation of DCE derived PK parameters with several clinical variables, such as illness duration and the expanded disability status scale (EDSS), in MS and CIS patients. Preliminary results from a subgroup of patients, indicate moderate correlations between  $k_{trans}$  in frontal, parietal and occipital NAWM and EDSS. Even more, strong correlations were found between permeability values in NAWM areas and scores on verbal and delayed retention indices, as well as with semantic verbal fluency tests. Associations are reported also among the permeability values and the fine motor efficiency through the Grooved Pegboard test completion time.

6) DCE and Dynamic Susceptibility Contrast perfusion MRI, provide information regarding BBB disruption and cerebral hemodynamics respectively. The correlation of quantitative parameters derived from the application of these two different perfusion techniques in patients of MS and CIS have not been previously studied in the literature. For this purpose, in the context of this dissertation we examined the underlying relationship among the DSC and DCE quantitative maps in a sub cohort of patients and found moderate correlations, while the overall results in the entire patient dataset will be published in the near future. More specifically, positive correlations were found between  $k_{trans}$ , CBF and CBV in NAWM areas when using the NoSnaps protocol, however these were not driven by values in a single group of patients.

In summary, the present dissertation provides a novel, time-extended DCE protocol with minimal increment of the MR acquisition time, along with a PK analysis software platform, which achieved to quantify active lesions of MS and CIS patients more accurately in comparison with the conventional protocol. Furthermore, preliminary results demonstrate that the novel time extended protocol provided more accurate classification of MS lesions (iso, mild, severe), and revealed correlations with clinical variables and specific neuropsychological deficits. Future work will aim towards further validation of these preliminary results, by applying the novel DCE protocol in a larger cohort of CIS and RRMS patients, and investigation of the correlation of DCE derived quantitative indices with neuropsychiatric measures, as well as, with the DSC derived hemodynamic parameters.

## Περίληψη

Η σκλήρυνση κατά πλάκας (ΣΚΠ) είναι μία χρόνια φλεγμονώδης απομυελινωτική νόσος του κεντρικού νευρικού συστήματος (ΚΝΣ), η οποία προσβάλλει κυρίως νέους. Αν και η ακριβής αιτιολογία της ΣΚΠ παραμένει κατά κύριο λόγο άγνωστη, είναι μία αυτοάνοση νόσος στην οποία τα ενεργοποιημένα Τ-κύτταρα περνώντας τον αιματοεγκεφαλικό φραγμό μεταφέρονται από την περιφέρεια στο ΚΝΣ, προκαλώντας τον σχηματισμό φλεγμονωδών απομυελινωτικών εστιών. Σε πρόσφατες έρευνες οι οποίες εξετάζουν την ποσοτική ανάλυση δεδομένων αιμάτωσης ΑΜΣ, έχει δειχθεί ο κρίσιμος ρόλος που έχει η δυσλειτουργία του αιματοεγκεφαλικού φραγμού στην παθολογία εστιών ΣΚΠ. Η ακρίβεια των δεδομένων αιμάτωσης καθώς και οι τεχνικές επεξεργασίας επηρεάζουν κατά πολύ την ακρίβεια των παραμετρικών χαρτών. Για τον λόγο αυτό, η σχεδίαση απεικονιστικών πρωτοκόλλων και μεθόδων ανάλυσης, προσαρμοσμένων στις ανάγκες των συγκεκριμένων παθολογιών, είναι υψηλής σημασίας στην κλινική πράξη.

Ο κύριος σκοπός της παρούσας διατριβής είναι να προσφέρει μια ενδεδειγμένη ερευνητική μεθοδολογία για την εφαρμογή τεχνικών αιμάτωσης ΑΜΣ σε ασθενείς με ΣΚΠ και κλινικά μεμονωμένο σύνδρομο (ΚΜΣ). Για αυτό τον σκοπό, αναπτύχθηκε η ακόλουθη ερευνητική μεθοδολογία:

1) Σχεδιάστηκε ένα νέο πρωτόκολλο Αιμάτωσης ΑΜΣ με Δυναμική ενίσχυση σκιαγραφικής ουσίας (DCE). Αυτό το νέο πρωτόκολλο κατάφερε να τριπλασιάσει το χρονικό παράθυρο παρατήρησης, με ελάχιστη επιβάρυνση στον χρόνο απεικόνισης. Εξαιτίας του επιπλέον κόστους για την απόκτηση εμπορικού λογισμικού φαρμακοκινητικής (ΦΚ) ανάλυσης καθώς και την τροποποίησης αυτών των

πλατφορμών για να αναλύσουν νέα πρωτόκολλα, υλοποιήθηκε και παραμετροποιήθηκε λογισμικό ανάλυσης ΦΚ δεδομένων.

2) Το υπολογιστικό λογισμικό ελέγχθηκε σε μια ομάδα ασθενών με καρκίνο του μαστού, προβλέποντας το αποτέλεσμα της θεραπείας πριν από την έναρξη της θεραπείας καθώς και νωρίς στον θεραπευτικό κύκλο. Η καλύτερη παράμετρος πρόβλεψης στην πρώτη επαναληπτική εξέταση, η οποία είχε υψηλό εμβαδόν κάτω από την καμπύλη (AUC) και ευαισθησία και ειδικότητα πάνω από 50%, ήταν η μέση τιμή της σταθεράς ανταλλαγής μεταξύ του εξωκυττάριου – εξωαγγειακού χώρου και του αγγειακού χώρου, *kep* (AUC 73,4%), ενώ το 80° εκατοστημόριο του εξωκυττάριου – εξωαγγειακού, *ve*, είχε την υψηλότερη ακρίβεια πριν από την έναρξη της θεραπείας με AUC 78,5%.

3) Με το νέο χρονικά αυξημένο καθώς και με το συμβατικό πρωτόκολλο δυναμικής ενίσχυσης σκιαγραφικής ουσίας απεικονίστηκε μια ομάδα ασθενών με ΣΚΠ με σκοπό την διερεύνηση των παραμέτρων του πρωτοκόλλου και των ΦΚ παραμέτρων για την ακριβέστερη ποσοτικοποίηση ενεργών απομυελινωτικών εστιών. Σύμφωνα με τα αποτελέσματα, το χρονικά αυξημένο πρωτόκολλο ποσοτικοποίησε με καλύτερη ακρίβεια τις ενεργές εστίες, ανιχνεύοντας κατά μέσο όρο 49% περισσότερα εικονοστοιχεία που προσλαμβάνουν σκιαγραφική ουσία, σε σύγκριση με το συμβατικό πρωτόκολλο. Επίσης, μετά από ενδελεχή συγκριτική ανάλυση αποδείχθηκε ότι το επιμηκυσμένο μοντέλο του Τοφτς ήταν το καλύτερο ΦΚ μοντέλο για την ποσοτικοποίηση ενεργών εστιών ΣΚΠ και ΚΜΣ.

4) Το νέο χρονικά εκτεταμένο πρωτόκολλο καθώς και το συμβατικό πρωτόκολλο δυναμικής ενίσχυσης σκιαγραφικής ουσίας, εφαρμόστηκαν σε μια ομάδα ασθενών

με ΣΚΠ και ΚΜΣ, με σκοπό να υπολογιστούν οι ΦΚ παράμετροι, όπως η σταθερά ανταλλαγής από τον αγγειακό χώρο στον εξωκυττάριο – εξωαγγειακό χώρο,  $k_{trans}$ , και ο εξωαγγειακός χώρος,  $v_p$ , σε περιοχές φυσιολογικά απεικονιζόμενης λευκής ουσίας και απομυελινωτικές πλάκες. Οι ΦΚ παράμετροι που προέρχονται από το νέο πρωτόκολλο κατάφεραν καλύτερο χαρακτηρισμό των διαφόρων τύπων ιστών και καλύτερο διαχωρισμό αυτών από την φυσιολογικά απεικονιζόμενη λευκή ουσία σε σύγκριση με το συμβατικό πρωτόκολλο.

5) Επίσης, αν και η γνωστική έκπτωση είναι κοινή στην ΣΚΠ, η υποκείμενη παθοφυσιολογία είναι κατά κύριο λόγο άγνωστη, ενώ οι συμβατικές τεχνικές ΑΜΣ δεν παρέχουν ισχυρές συσχετίσεις με νευροφυσιολογικές διαταραχές. Για αυτό τον λόγο, η παρούσα διατριβή εξέτασε την συσχέτιση των ΦΚ παραμέτρων από τα δεδομένα με δυναμική ενίσχυση σκιαγραφικής ουσίας σε ασθενείς με ΣΚΠ και ΚΜΣ με πολλαπλές κλινικές μεταβλητές, όπως διάρκεια ασθένειας και το σκορ διευρυμένης κλίμακας κατάστασης αναπηρίας EDSS. Τα αρχικά αποτελέσματα σε μια υποομάδα ασθενών, αναφέρουν ότι υπάρχουν μέτριες συσχετίσεις μεταξύ αυτών του  $k_{trans}$  και του EDSS στον μετωπιαίο, βρεγματικό και ινιακό λοβό. Επίσης, βρέθηκαν ισχυρές συσχετίσεις μεταξύ των τιμών της διαπερατότητας στην φυσιολογικά απεικονιζόμενη λευκή ουσία και επιδόσεων σε δοκιμασίες μνήμης επεισοδίων, λεκτικής και κινητικής ευχέρειας (λεπτή κινητικότητα). Επιπλέον συσχετίσεις βρέθηκαν μεταξύ των τιμών διαπερατότητας και της αποδοτικότητας χειρισμών ακριβείας μέσω του χρόνου ολοκλήρωσης του τεστ Grooved pegboard.

6) Η δυναμική ενίσχυση σκιαγραφικής ουσίας και η δυναμική με αντίθεση μαγνητικής επιδεκτικότητας (DSC) τεχνικές αιμάτωσης, παρέχουν πληροφορίες για

την ρήξη του αιματοεγκεφαλικού φραγμού και τις εγκεφαλικές αιμοδυναμικές παραμέτρους αντίστοιχα. Η συσχέτιση ποσοτικών παραμέτρων οι οποίες προέρχονται από την εφαρμογή των δύο αυτών πρωτοκόλλων αιμάτωσης σε ασθενείς με ΣΚΠ και ΚΜΣ δεν έχουν μελετηθεί μέχρι σήμερα. Για τον σκοπό αυτό, η παρούσα διατριβή εξέτασε τη σχέση μεταξύ παραμετρικών χαρτών DSC και DCE σε μια υποομάδα ασθενών και βρήκε ότι υπάρχουν συσχετίσεις, ενώ τα συνολικά αποτελέσματα στην πλήρη ομάδα ασθενών θα δημοσιευθούν στο άμεσο μέλλον. Πιο συγκεκριμένα, θετικές συσχετίσεις βρέθηκαν μεταξύ του  $k_{trans}$ , του CBF και του CBV σε περιοχές φυσιολογικά απεικονιζόμενης λευκής ουσίας με την χρήση του συμβατικού πρωτοκόλλου, αλλά αυτές δεν χαρακτηρίζουν μεμονωμένα τις κλινικές ομάδες.

Συνοψίζοντας, η παρούσα διατριβή παρουσίασε ένα νέο χρονικά επιμυκησμένο πρωτόκολλο DCE το οποίο επιβάρυνε ελάχιστα τον συνολικό χρόνο απεικόνισης, καθώς επίσης και ένα λογισμικό ΦΚ ανάλυσης, το οποίο κατάφερε να ποσοτικοποιήσει με ακρίβεια ενεργές εστίες ασθενών με ΣΚΠ και ΚΜΣ σε σχέση με το συμβατικό πρωτόκολλο. Επίσης, τα αρχικά αποτελέσματα της διατριβής δείχνουν ότι το νέο χρονικά εκτεταμένο πρωτόκολλο πέτυχε καλύτερο διαχωρισμό των εστιών ΣΚΠ, και βρέθηκαν μέσω αυτού συσχετίσεις με κλινικές μεταβλητές και ειδικές νευροψυχολογικές διαταραχές. Μελλοντική δουλειά αυτής της διατριβής, στοχεύει στην επιπλέον τεκμηρίωση των πρώιμων αποτελεσμάτων, εφαρμόζοντας το πρωτόκολλο δυναμικής ενίσχυσης σκιαγραφικής ουσίας σε μια μεγαλύτερη ομάδα ασθενών με ΣΚΠ και ΚΜΣ, καθώς και την διερεύνηση των συσχετίσεων των παραγόμενων ποσοτικών παραμέτρων δυναμικής ενίσχυσης σκιαγραφικής ουσίας με

νευροψυχιατρικές μετρήσεις, όπως επίσης και με τις αιμοδυναμικές παραμέτρους του πρωτοκόλλου με δυναμική αντίθεση μαγνητικής επιδεικτικότητας.

## Part A: Theoretical Background

### 1 Introduction

Multiple Sclerosis (MS) is a chronic, inflammatory, demyelinating disease of the Central Nervous System (CNS) commonly affecting young adults. It usually begins as a relapsing-remitting process (RR-MS), predominantly characterized by inflammatory demyelination that secondarily evolves to a progressive stage with neurodegeneration, gliosis and accumulating disability. Although the precise etiology of MS is largely unknown, it is considered primarily an autoimmune disease in which activated myelin-specific T-cells migrate from the periphery to the CNS, by crossing the blood brain barrier and induce the formation of new inflammatory demyelinating lesions (1, 2). The BBB is a complex organization of cerebral endothelial cells, pericytes and their basal lamina, which are surrounded and supported by astrocytes and perivascular macrophages. Dysregulation of the BBB and transendothelial migration of activated leukocytes are among the earliest cerebrovascular abnormalities seen in MS (1, 2). Histopathological and Magnetic Resonance Imaging (MRI) studies reported BBB abnormalities not only in acute active inflammatory MS lesions, but in inactive, non-enhancing lesions and the normal appearing white matter (NAWM), as well (3-5). According to research studies concerning the development of drug therapies in MS, the leukocyte passage across the BBB is very important for disease pathophysiology (6, 7) and resolution of inflammation along with protection of BBB function is the therapeutic target for many proposed MS treatments (1, 2). So, the development of quantitative MRI techniques that detect and quantify the BBB permeability is of paramount importance in understanding pathophysiology, determination of disease activity and estimation of treatment efficacy in MS.

Dynamic Contrast Enhanced T1 perfusion MRI (DCE-MRI) is a quantitative MRI technique able to detect and quantify the disruption of the BBB. It comprises of the dynamic acquisition of multiple T1-w images before, during and after the administration of a paramagnetic contrast agent (CA), resulting in a dynamic signal intensity (SI) over time for every lesion that enhances CA (8, 9). Many compartmental models have been proposed to quantify the CA pharmacokinetics (PK), from very simple implementations that assume a single compartment, to complex models incorporating multiple compartments in which CA is being transferred. PK analysis of DCE data, was first proposed by Tofts (10) for MS active lesions, and afterwards widely applied in clinical practice, especially to brain tumors (9).

According to previous studies MS lesions are characterized by low BBB permeabilities compared with tumors (11-13), inducing the requirement of perfusion studies with increased acquisition time. In particular, longer scan times implies increased number of measurements (samples) and thus more time for the CA to extravasate to the measured tissue. This indicates higher tissue concentrations that is of major importance when trying to measure subtle BBB disruptions. Furthermore, considering the necessity of minimizing the patient examination time in the MR system, it is of great importance to provide new methods that extend the time of perfusion observation without charging the examination time.

## 2 MULTIPLE SCLEROSIS

### 2.1 Epidemiology

MS is the most common demyelinating disease, with variable incidence among different countries. It is reported that there is a prevalence of more than 100/100.000 in North America and Europe compared to the low rates (2/100.000) in Eastern Asia

and sub-Saharan Africa, (14), while its prevalence worldwide has been, also, increasing over time, probably due to prolonged survival (15). In fact, the median prevalence of MS globally, increased from 30/100.000 in 2008 to 33/100.000 in 2013.

The aforementioned geographical distribution of MS incidence can be attributed to environmental, as well as, genetic factors. Environmental factors that may trigger the disease onset include the exposure to sunlight, ultraviolet radiation, vitamin D, or Epstein-Barr virus (EBV). Genetic factors are supported by reports that estimate the risk of developing MS to be 1 / 1000 in normal population, while it increases to 1 / 4 in identical twins, when one twin is affected (16). Finally, concerning the gender related incidence of MS, it has been reported that women have double prevalence rates compared to men in France (17) Norway (18) and Australia (19).

## 2.2 Pathogenesis

The causing factor of MS is generally unknown. It is speculated that there is genetic predisposition to the disease, while the initialization of the symptoms is stimulated from environmental factors. The genetic predisposition of the disease is assumed by the familial preponderance in many cases, the increased frequency in identical twins and the increased prevalence in certain races. The probability that a first-degree relative will be affected from MS is 1-4%, 20-40 times greater than the corresponding frequency on the general population.

At this time, a widely accepted theory describes that MS is expressed under a certain combination of exogenous factors in people with genetic predisposition and leads to chronic inflammation, autoimmune reaction and demyelinating plaques in the WM of the CNS. There are several genes that confer susceptibility to MS. Among

the most important are genes of the major histocompatibility complex like HLADRB1\*1501 allele, HLA DQA1\*0102 allele or HLA DQB1\*0602 allele, responsible for 50% genetic risk for MS. It has also been found that HLA DRB1 1501 allele is linked to disease severity. Other genes that have been identified code for receptors of interleukin 2 and interleukin 7 (20). The human leukocyte antigen (HLA) gene cluster on chromosome 6p21 is, also, highly associated with high MS risk (21). Unlike the aforementioned genes, HLA-C554 and HLADRB1\*11 have protective effects.

In the past it was thought that vaccinations, in specific for hepatitis B, can increase the probability of developing MS, but more recent studies have rejected this hypothesis (22). Leitner et al. (23) reported that the pathology of NAWM, axonal loss, remyelination and the progress of focal inflammatory loss, are based on the dysregulation of neurosteroid synthesis, leading to disturbance on myelin and increased vulnerability of the myelin sheath, phagocytosis of myelin debris and processing of myelin antigen by microglia.

MS is considered primarily an immune-mediated disease of the CNS in which auto-aggressive T-cells are thought to cross the BBB inflicting demyelination and axonal loss and eventually leading to progressive disability (Figure 1). Despite intensive research, the etiology of MS is largely unknown, but recent developments in MS drug therapies have emphasized leukocyte passage across the BBB, as being of paramount importance for disease pathophysiology. Histopathological studies as well as MRI findings have reported abnormalities of this barrier in inactive MS lesions and NAWM (24, 25). Inflammation of the white and gray matter tissues in the CNS due to

focal immune cell infiltration and their cytokines are the incipient cause of damage in MS.

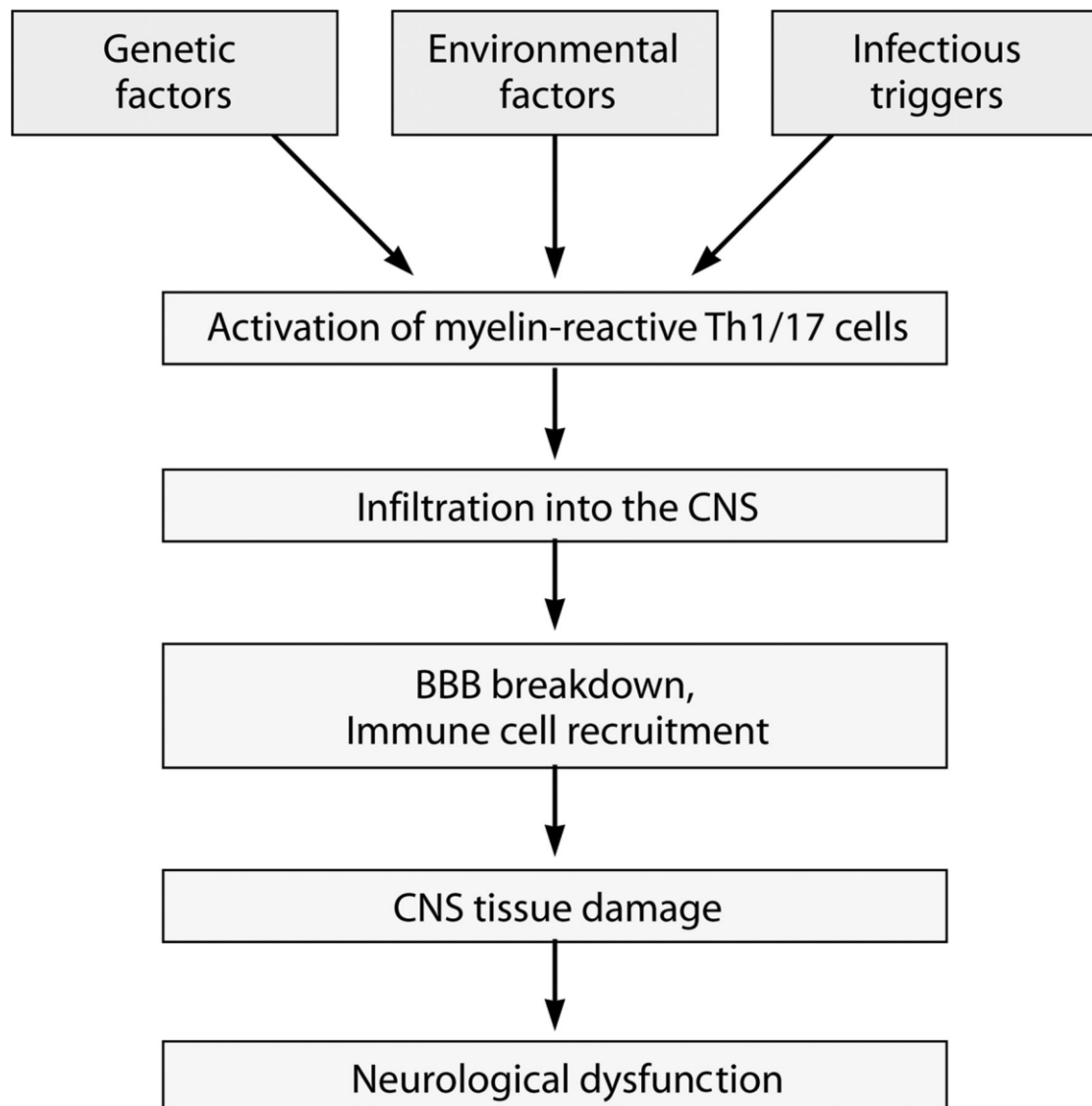


Figure 1. Pathophysiology of multiple sclerosis: potential triggering factors that activate myelin-reactive T cells and sequential events in disease progression (from Kremtsov et al. Molecular and Cellular Biology 2013)

Many studies have suggested that CD4+ T cells immune responses, initiated by interaction between antigen presenting cells (APCs) with T lymphocytes, play an important role in the initiation and progression of MS (26, 27). Pathogen-associated molecules simultaneously bind to toll-like receptors on APCs and induce production of specific cytokines, that include interleukin (IL)-12, IL-23 and IL-4. These cytokines

induce CD4+ T cell differentiation into Th1, Th2, or Th17 phenotypes which release in turn other (Interferon gamma (IFN $\gamma$ ) or type II interferon, tumor necrosis factor alpha (TNF- $\alpha$ )) pro-inflammatory cytokines critical for innate and adaptive immunity. These cytokines are produced by Th1 cells, and promote inflammation by suppressing Th2 differentiation. Th2 cells secrete the anti-inflammatory cytokines, IL-4 and IL-13. Th17 is another CD4+ T cells which induces a large number of cytokines (IL-17, IL-21, IL-22 and IL-26) which are capable of promoting inflammation (Figure 2).

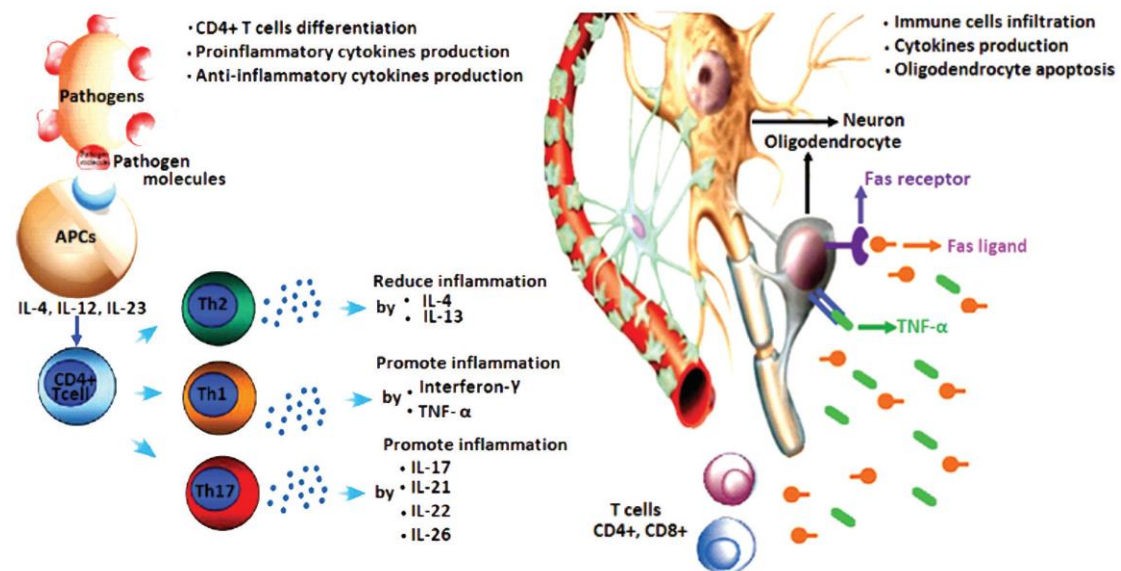


Figure 2. Immune cells and their cytokines which involved in the pathogenesis of MS (from Ghasemi N, et al. Cell J. 2017; 19(1): 1-10).

### 2.3 Clinical manifestations

MS clinical symptoms present initially at mean age of 30 years, most frequently in 23-24 years (28). The onset of the disease is observed in subjects 20 to 40 years in 70% of the cases, older than 40 years in 20% of the cases, and finally 10% of the cases in ages smaller than 10 years old. Nevertheless, there have been cases with initial disease symptoms in infants about 15 months after birth or in adults older than 50 years old (29, 30).

There are four subtypes of MS: relapsing remitting MS (RRMS), primary progressive MS (PPMS), secondary progressive MS (SPMS) and progressive relapsing MS (PRMS). RRMS is the most common subtype (approximately 87%) characterized by unpredictable acute inflammatory attacks on myelin and nerve fibers followed by periods of remission (31). Approximately 10-15% of MS patients are diagnosed with PPMS, which largely affects the spinal cord. Nearly 65% of patients with RRMS will subsequently develop SPMS which is considered the second phase of this disease. Finally, PRMS is the least common type of MS that occurs in approximately 5% of patients (Figure 3).

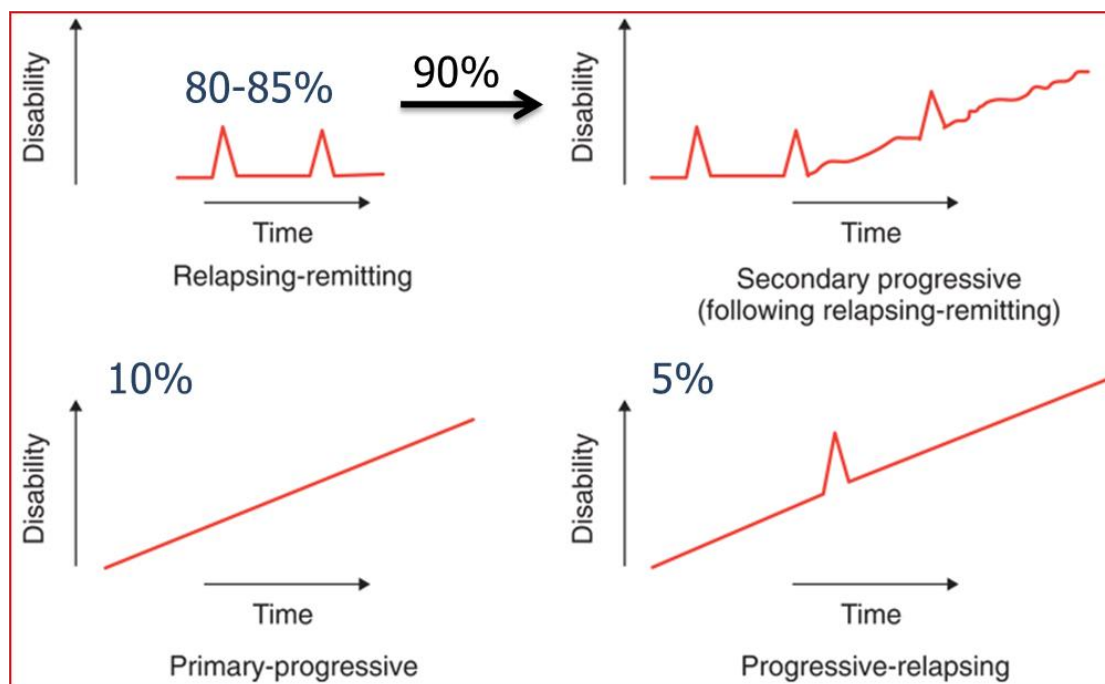


Figure 3. The clinical subtypes of MS

Clinically isolated syndrome (CIS) is a term that describes a clinical episode of at least 24 hours, suggesting of an inflammatory demyelinating disorder of the CNS. It usually occurs in young adults and represents a monophasic episode, isolated in time, and usually isolated in space, affecting optic nerves, the brainstem, or the spinal cord,

while there are no signs of fever or infection. Although patients usually recover from their presenting episode, CIS is often the first manifestation of MS. The course of MS after CIS is variable: after 15–20 years, a third of patients have a benign course with minimal or no disability and a half will have developed secondary progressive MS with increasing disability (32-35). Prediction of the long-term course at disease onset is unreliable, while disease-modifying treatments delay the progression from CIS to MS, having the potential to prevent or delay demyelination and axonal loss (36).

### 2.3.1 Clinical symptoms

MS focal alterations can be found in many different CNS locations, implying a variety in clinical symptoms. According to Gebhardt (37), neurological symptoms at the onset of the disease could be paresis, paresthesias and numbness, ataxia, visual disturbances, neuro-urological dysfunction, neuropsychological deficits, and fatigue. Symptoms that could be observed in any stage of the disease, in more than 50% of the cases, are fatigue, vision problems, numbness and tingling, muscle spasms, stiffness and weakness, mobility problems, pain, problems with thinking, depression and speech difficulties.

### 2.3.2 Diagnosis of multiple sclerosis

The diagnosis of MS is based on medical history and neurological examination, application of imaging techniques such as magnetic resonance imaging (MRI), lumbar punctures (LP) for cerebrospinal fluid (CSF) analysis, evoked potentials, and blood samples analysis (38, 39). Conventional MRIs of the brain and the spinal cord can identify focal demyelinating lesions, as well as, parenchymal atrophy, in chronic cases. Visual, brain stem, auditory, and somatosensory evoked potentials tests offer information about demyelination in the optic nerve and respective CNS areas. In

addition, CSF analysis for determination of myelin basic protein and IgG and blood sample analysis for detection of vitamin deficiencies are of vital importance for the diagnosis of MS.

### 2.3.3 Quantitative assessment of the clinical disability

For a better clinical, prognostic and therapeutic approach, the utilization of an objective classification system of the clinical functional status of MS patients is mandatory. The first system for the classification of clinical disability, both in the clinical practice and in research studies, is the expanded disability status scale (EDSS) according to Kurtzke (40). In that scale, the clinical - functional status scale starts from 0 (absence of functional disorders) up to 10 (death from disease) with incremental steps of 0.5, while the score system considers 8 functional systems (pyramidal, cerebellar, brain stem, sensory, bowel and bladder, visual, cerebral total, and cerebral mentation), Table 1.

*Table 1. Expanded Disability Status Scale (EDSS)*

Grade	Clinical Functional Status
0	Normal neurological examination
1	No disability, minimal signs in one FS
1.5	No disability, minimal signs in more than one FS At
2	Minimal disability in one FS
2.5	Mild disability in one FS or minimal disability in two FS
3	Moderate disability in one FS, or mild disability in three or four FS. No impairment to walking
3.5	Moderate disability in one FS and more than minimal disability in several others. No impairment to walking
4	Significant disability but self-sufficient and up and about some 12 hours a day. Able to walk without aid or rest for 500m
4.5	Significant disability but up and about much of the day, able to work a full day, may otherwise have some limitation of full activity or require minimal assistance. Able to walk without aid or rest for 300m
5	Disability severe enough to impair full daily activities and ability to work a full day without special provisions. Able to walk without aid or rest for 200m
5.5	Disability severe enough to preclude full daily activities. Able to walk without aid or rest for 100m

6	Requires a walking aid – cane, crutch, etc. – to walk about 100m with or without resting
6.5	Requires two walking aids – pair of canes, crutches, etc. – to walk about 20m without resting
7	Unable to walk beyond approximately 5m even with aid. Essentially restricted to wheelchair; though wheels self in standard wheelchair and transfers alone. Up and about in wheelchair some 12 hours a day
7.5	Unable to take more than a few steps. Restricted to wheelchair and may need aid in transferring. Can wheel self but cannot carry on in standard wheelchair for a full day and may require a motorized wheelchair
8	Essentially restricted to bed or chair or pushed in wheelchair. May be out of bed itself much of the day. Retains many self-care functions. Generally has effective use of arms
8.5	Essentially restricted to bed much of day. Has some effective use of arms retains some self-care functions
9	Confined to bed. Can still communicate and eat
9,5	Confined to bed and totally dependent. Unable to communicate effectively or eat/swallow
10	Death due to MS

In EDSS system, different functional abilities of the patient are represented by different weights, for example there is a lot of significance in mobility problems (level 4-8), while learning and behavioral disorders are not being handled with the same importance, a pitfall of the method. Another drawback is the subjective classification of the patients and the medium correlation of the results when classifying the same patient, a fact that constitutes this method less reliable.

Moreover, EDSS score is more frequently used during the onset of the disease, and in disease types characterized by progressive course. For this reason, the integrated disability status scale (IDSS) was developed, in which the area under the curve (AUC) of successive EDSS measurements is computed, and this represents the neurological dysfunctionality of the patient (11).

## 2.4 MS Pathology

The presence of demyelinating plaques in the CNS, is the pathological hallmark of MS. White matter (WM) lesions is the main field of interest in MS, due to the better contrast and detectability on MRI. It is speculated that high field MRI will further

facilitate the research in gray matter (GM) lesions. Main pathological features of MS are a) inflammation b) demyelination c) axonal loss and d) variable gliosis.

WM lesions have a characteristic perivenular distribution and tend to appear on specific brain regions, located around the ventricles, periaqueductal sites, and optic nerves, while cord lesions have frequently subpial position. There is a little knowledge regarding the mechanisms of periventricular distribution but there are indications that these are related to disability (41).

#### 2.4.1 The Active lesion

Acute, active MS lesions are characterized by acute inflammation, BBB disruption and demyelination. Relevant events can be assumed the rise of circulating cytokines (TNF $\alpha$  and IFN $\gamma$ ) that stimulates endothelial cells in the post capillary venules and may precede the lesion formation (42, 43). Moreover, inflammatory mediators stimulate the BBB dysfunction resulting in edema in the perivascular cuff. Myelin and oligodendrocytes form myelin sheaths are opsonized, while oligodendrocyte loss is strongly correlated with the number of macrophages in histology (44).

#### 2.4.2 Mechanisms of axonal loss

Although the most visible features on MS lesions are the myelin sheath damage and the oligodendrocyte death, axonal loss has been described, also, with adequate accuracy (45, 46). The degree of axonal loss can vary among different patients and different lesions (47). A stable marker of axonal damage is the Amyloid precursor protein (APP), reported as an index with increased levels in active lesions (48, 49). Concentrations of APP correlate with severity of inflammation measured by the amount of microglia and VD8 T-cells (47). Moreover, the extent of axonal loss is

correlated with disability in Extrinsic Allergic Encephalomyelitis (EAE) (50) and with spectroscopic markers of axonal integrity in MS patients (51, 52), while there is also a correlation among axonal damage and disorders to the local vasculature through edema and vessel inflammation.

#### 2.4.3 Pathological Heterogeneity in lesions

Heterogeneity in MS pathologic phenotype has been proved in histological research studies on active MS lesions, consistent with observations of disease diversity (53). Acute lesions have 4 different pathological patterns, as shown in Table 2, partitioned from the degree of T-cell involvement, oligodendroglial dysfunction and complement activation (54).

*Table 2. Patterns of lesion pathology (Lucchinetti et al., 2000)*

Subtype	Immunology	Oligodendrocytes	Border
I 18%	CD8 T cells and macrophage mediated demyelination	Survival of oligodendrocytes with rapid remyelination	Sharp Centred around Venules
II 56%	As in I, plus antibody & complement deposition	Survival of oligodendrocytes with rapid remyelination	Sharp
III 24%	Microglial activation	Oligodendrocyte destruction Distal oligopathy and dystrophy. Early myelin loss Axonal damage	Indistinct Not centred around Venule
IV 2%	Macrophages and T cells. Only seen in PPMS	Primary oligodendrocyte degeneration. Axonal damage	Sharp, perivenous

Inflammatory infiltrate is obvious in every lesion pattern. Moreover, patterns I and II are characterized by an intense perivenous immune reaction with areas of inflammation and demyelination, while pattern II has an additional association of IgG deposition. It is apparent that types III and IV result from primary oligodendroglial dysfunction and apoptosis with demyelination. Patterns I and II are in every disease subtype, while pattern III is highly observed in patients with disease duration less than 2 months. Pattern IV, is the most rare pattern, and it has been observed in primary progressive types of the disease.

#### 2.4.4 Chronic Lesions

The main pathological characteristic of the chronic lesions is variable degree of demyelination, axonal loss and gliosis. In a study from Kuhlmann et al. (49), it is reported that the inflammatory cellular infiltrate is associated with demyelination reduction over time. Although there are oligodendrocyte precursors, there is a variable presence of oligodendrocytes and remyelination, while ongoing inflammation and neuronal damage is still occurring at chronic lesions (47).

#### 2.4.5 Remyelination

It has been reported that remyelination appears in 13-42% of MS lesions (55), a procedure that may occur early in the lesion genesis and is more evident in lesions with great number of macrophages and oligodendrocytes (56). Plaques under remyelination are frequently described with the term “shadow plaques” (57) and they display minimal axonal loss (58). Factors that are able to regulate remyelination are not yet fully explained, but they include the presence of signaling factors in the environment, as well as the proximity of viable oligodendrocytes that are able to effectively remyelinate the lesion (59).

#### 2.4.6 Grey Matter involvement

Demyelinating lesions can also be found in the deep and cortical GM (60, 61). The cortical lesions can be adjacent to subcortical lesions (type 1), restricted within the cortex (type 2) or they can even include the pial surface (type 3) (61). Moreover, these are associated with decreased number of inflammatory cells compared to WM lesions, and they may exhibit great amounts of axonal loss.

### 2.5 The Blood Brain Barrier (BBB)

The BBB and the blood cerebrospinal fluid barrier (BCB) represent a complex vasculature network that forms a continuous cellular barrier between the CNS and the

systemic circulation. Most of the important metabolic exchanges critical to CNS homeostasis occur through this tightly regulated network. Its role is to control the transfer of chemical elements between the brain and the blood, in order to keep under control the influx of neurotransmitters and protein toxins from the blood to the brain. The BBB is a membranous barrier that separates the brain tissue of the circulating blood. In the CNS, blood capillaries are structurally different from the capillaries of other tissues and covered by special endothelial cells without pores and sealed with tight junctions. The BCB is located in the choroid plexus along with the arachnoid layers of the meninges. Due to its location and the direction of the flow of CSF, choroid plexus epithelium is considered the most important part of the BCB. It seems that the permeability in the choroid plexus is greater than that of the tight junctions of the endothelium of the BBB (1).

BBB was first reported from Ehrlich, by using intravital tracers, able to change their colors according to their oxidate state. (62). Later, Lewandowsky reported that the brain capillaries suppress specific molecules from entering the brain (63). The properties that were rendered the cerebral vasculature were not clear, since the electron microscopy demonstrated that the endothelial barrier is consisted by tight junctions between the endothelial cells (64). Afterwards, Crone and Olesen (65) reported that trans-endothelial electrical resistance is increased in the BBB compared to the endothelium in capillaries, due to the low permeability of charged particles. Moreover, studies concerning electrical resistance was utilized to determine the BBB integrity in the endothelium, by studying the BBB development in neonatal rats (66).

In a study from de Vries et al. (67) it was reported that the BBB is existed in more than 99% of brain capillaries covering an area that is up to  $180\text{cm}^2/\text{g}$  of brain tissue. In some locations the BBB is substituted by a blood-CSF barrier, which also prevents the entry of blood compounds in the CSF. The capillaries in the brain are composed of an endothelial layer which is covered by a basement membrane called the basal lamina. Astrocytes can communicate with this component with the astrocytic foot process as shown in Figure 4. The neurovascular unit is a dynamic functional unit that represents the intimate contact among the astrocytes, pericytes, microglia, blood vessels and neurons and their signaling interactions.

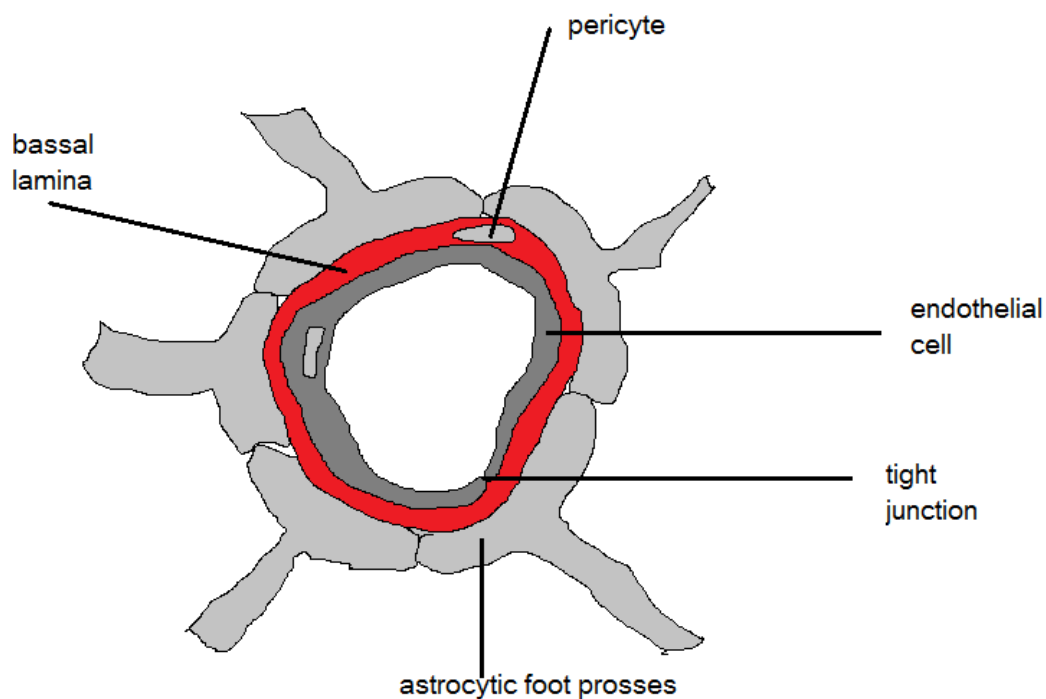


*Figure 4. Schematic of a cross section of brain capillary*

More specifically, the endothelium, a single layer of endothelial cells, is of great importance in the control of blood fluidicity, platelet aggregation and vascular tone. The main difference among the endothelial cells in the brain and the body is the profusion of transmembrane protein complexes, which are responsible for the

endothelial cell adhesion. These complexes are called junctional complexes and their two main subcategories are: a) the adherens junctions, speculated to be responsible for the modulation of cell polarity, cell to cell interaction and paracellular permeability, and b) the tight junctions that form the anatomical basis for the BBB, together with the endothelial cell layer.

Pericytes cover the brain vessels and capillaries, being, also, in close proximity to astrocytes and neurons. Sherpo et al. estimated the ratio of pericytes to endothelial cells and reported that the endothelial are triple compared to the pericytes (68). Moreover, pericytes seems to have a key role in the BBB formation by utilizing multiple signal pathways, as well as, by controlling the cerebral blood flow through the regulation of the capillaries diameter (69).

Astrocytes can interact with microvascular endothelial cells and pericytes by endfeet protrusions. These interactions may also take place with the smooth muscle cells at the arterioles. The role of astrocytes is highly important for the conservation of the BBB, as well as in the homeostasis of extracellular concentration of transmitters, metabolites, ions and water (70).

Basal lamina is a thin assembly of extravascular matrix proteins that supports the muscle cells, the nerve cells and the epithelia outside the CNS. It is a network of protein polymers that form a layer under epithelia. Its structure is composed of three layers, the endothelial layer, the astrocytic layer and an intermediate layer consisting of collagen type IV.

### 2.5.1 Transport across the BBB

The control of substances that transit the BBB, among the brain parenchyma and the blood, is of great importance for the normal brain function. This is achieved by a number of mechanisms, depending on the fat-solubility of the substances. The exchange of lipid soluble gases takes place through diffusion across the BBB, depending on the corresponding concentrations in the brain and the blood. Water soluble and lipophobic molecules pass the BBB through specific carrier-mediated systems. For amino acids three different carrier systems are existing, namely the L, A and ASC. Each of them is able to transport different sets of amino acids, depending on their polarity and their size.

### 2.5.2 Pathological BBB disruption in MS

BBB breakdown is taking place in tumor (71), trauma (72) and a number of neurological diseases including amyotrophic lateral sclerosis (ALS) and MS (73-75). Considering the BBB disruption in MS, the most intense phase takes place in the early stages of lesion formation, but there is evidence of persisting BBB leakage, in long-lasting visibly non-enhanced lesions (76).

Concerning the BBB disruption on active MS lesions, histological studies reported that edema, lymphatic infiltration and extravascular fibrin disposition are suggestive of breakdown (77). Studies that have been performed using T1 Gd-enhanced MRI, reported that BBB is found on new or actively inflammatory lesions (78, 79). BBB breakdown in acute MS lesions is speculated to be the result of migration, proliferation and activation of leucocytes, inducing release of cytokine (80). The release of cytokines compromises the BBB by phosphorylation of occludin, resulting to the dissociation from cytoskeleton and tight junction breakdown. Minagar

et al. reported that when the exposure of the endothelium to cytokines results in reduced tight junction expression and trans-endothelial resistance (80). In MS the breakdown of the BBB is thought to be transient, although recurrence may be observed at the same or different locations within interval of weeks, months or even years. The subsequent progress and lesion development is irregular and involves additional phases of BBB leakage, immunologically mediated demyelination and various degrees of axonal transection (Figure 5) (1).

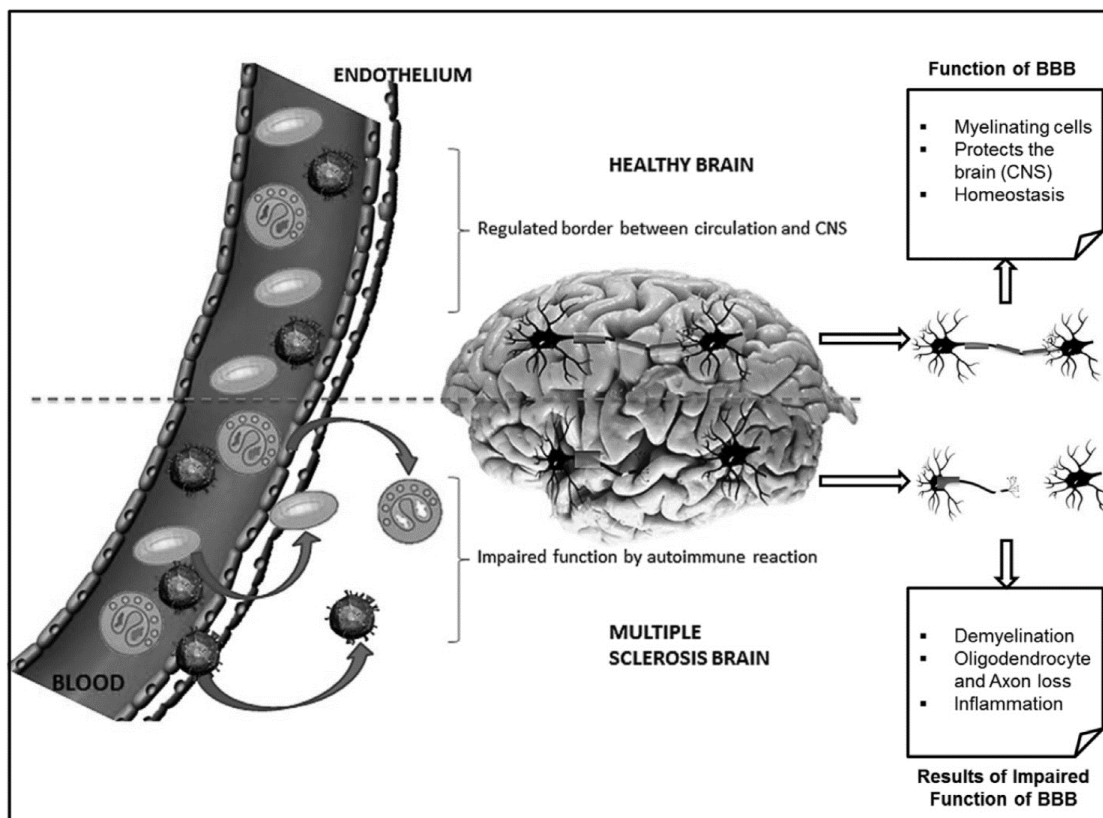


Figure 5. BBB in healthy brain and in MS brain (from Ortiz et al. 2014).

BBB breakdown has also been reported in non-active MS lesions. Leech et al. reported abnormal tight junctions in lesions without active inflammation, by using confocal laser microscopy (81), while extravascular fibrin deposits were found in non-active lesions (24). Moreover, Adams et al. reported that vessels located in non-active

lesions frequently demonstrate wall thickening and fibrin disposition (77), proposing that leakage from these lesions might be due to imperfect BBB repair. Results from Claudio et al. with morphometric analysis of capillaries in non-active MS lesions that revealed reduction in mitochondria and increase in pinocytic vesicles might support this hypothesis (24).

### 3 Conventional MR imaging in MS

MRI is the modality of choice in MS patients for diagnosis and monitoring the disease course (82-84), due to the increased sensitivity in detecting the MS lesions (85). These lesions appear as focal white matter areas of increased signal intensity on T2-w sequences in more than 90% of the examined patients (86-88). MR sensitivity in highlighting MS plaques is increased, compared with Computed Tomography imaging, in which sensitivity can be up to 80% while specificity is up to 90% (89).

Periventricular MS lesions very often are distributed along the deep medullary veins, resulting in a typical perpendicular orientation of their main axis to the lateral ventricles. Their shape is ovoid when they are depicted on the axial plane and this is defined as the Dawson's finger morphology. This typical morphology and orientation help to differentiate between MS Lesions and periventricular lesions found in other pathologies, including migraine (90), ischaemic small-vessel disease (91) and neuromyelitis optica spectrum disorders (92) (Figure 6).

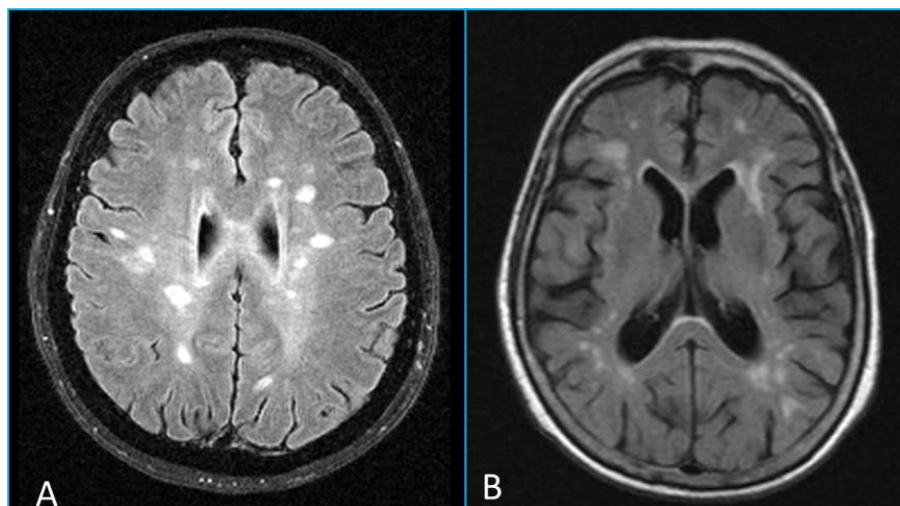


*Figure 6. Typical ovoid white matter lesions, perpendicular to the lateral ventricles, in a patient with RRMS (A). Their typical configuration permits differential diagnosis from white matter lesions due to small vessel disease (B).*

MS plaques commonly appear in the periventricular, subcortical or juxtacortical WM, but, also, the deep gray matter, the corpus callosum, brainstem, cerebellum, spinal cord and cranial nerves (78), (Figure 7). By implementing specific MR sequences or High field MRI cortical lesions might, also, be detected (Figure 8).

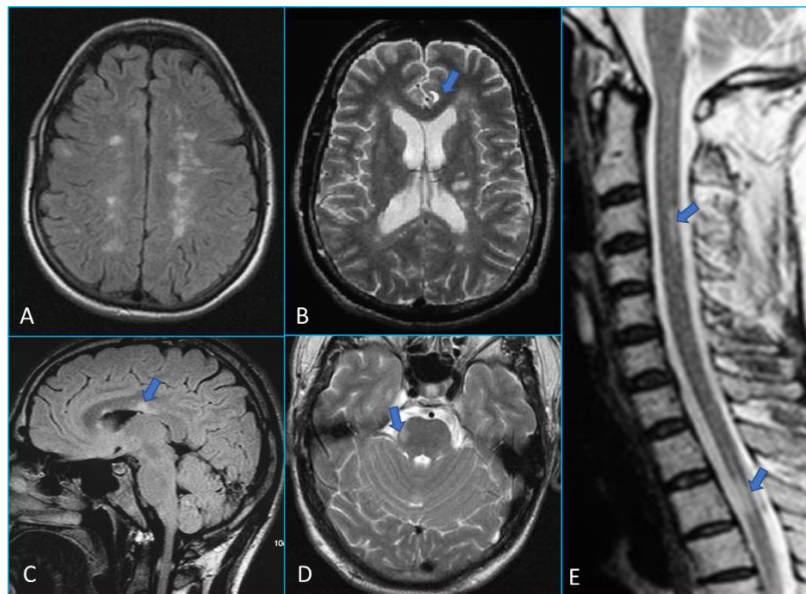


Figure 7. Multiple demyelinating lesions in a patient with RRMS at the periventricular and subcortical WM (A, B), juxtacortical WM (B, arrow), corpus callosum, lateral portion of the pons (D) and spinal cord (E)

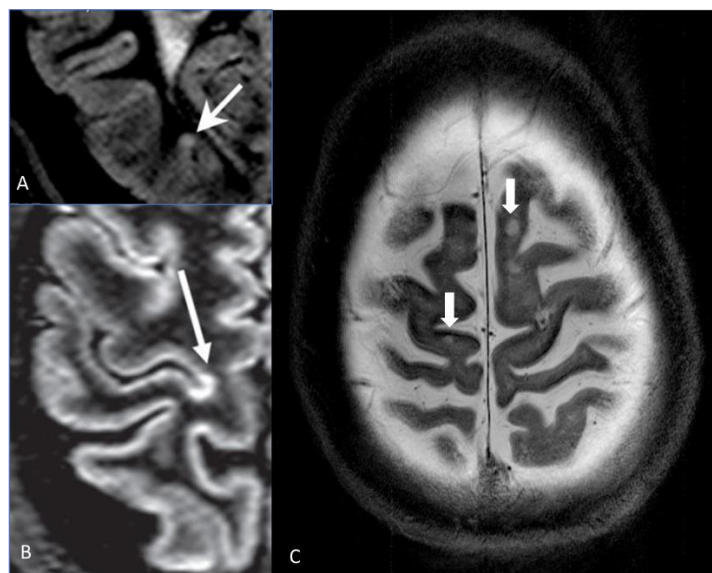
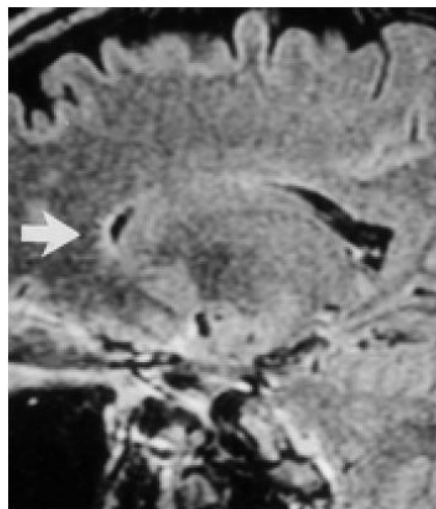


Figure 8. Intracortical demyelinating lesions using DIR sequence at 3T MR scanner (A, B), and T2-w sequence at 7T MR scanner.

MS plaques located in the corpus callosum, and more specifically in the calloseseptal interface, as shown in Figure 9, which is a typical finding of the disease with high sensitivity (93%) and specificity (96%) (93). It is postulated that the presence of edema and demyelination along the subependymal veins results in a striated depiction in the corpus callosum (subcallosal striation), which represents an early imaging finding indicative of corpus callosum involvement (94), as shown in Figure 9.



*Figure 9. Subcallosal striation at the calloseseptal interface, representing an early imaging finding of corpus callosum involvement in a patient with RRMS.*

### 3.1 T1 sequences in MS

MS lesions have variable signal intensity (SI) on T1 sequences, mainly depending on the amount of demyelination that inversely correlates with the decrease of SI (95) (Figure 10). Decrease of SI in MS plaques results, also, from: a) the presence of extracellular edema, due to inflammation, in acute lesions and b) axonal loss and gliosis, in chronic lesions (96). Bruck et al. described 4 stages of MS lesion evolution, based on pathological criteria, which correlate with their signal intensity on T1 MR sequences (78):

- 1) early active lesions, having equal or slightly decreased SI compared with the adjacent WM, and enhancing after Gadolinium administration,
- 2) newly form active lesions, with increased signal intensity,
- 3) demyelinating plaques depicted with decreased SI and absence of Gadolinium enhancement,
- 4) remyelinating plaques with slightly decreased signal and Gadolinium enhancement.

Severe demyelinating lesions, having SI similar to that CSF, are characterized as “black holes” (22).

Moreover, the rate of SI decrease in MS lesions is correlated with the degree of axonal damage (47), possibly due to the consequent increased levels of the extracellular fluid, resulting in T1 relaxation time elongation (97, 98). This finding has been confirmed in Magnetic Resonance Spectroscopy studies that correlate the SI of MS lesions on T1 sequences with the decrease of NAA (N-acetyl aspartate), index of neuronal integrity (96, 99).

In many cases, a hyperintense ring is detected at the periphery of MS lesions on T1 sequences. This ring has been attributed to the presence of free radicals in the adjacent parenchyma, but might be, also, the result of lipids due to demyelination or even micro-petechial hemorrhages (97).

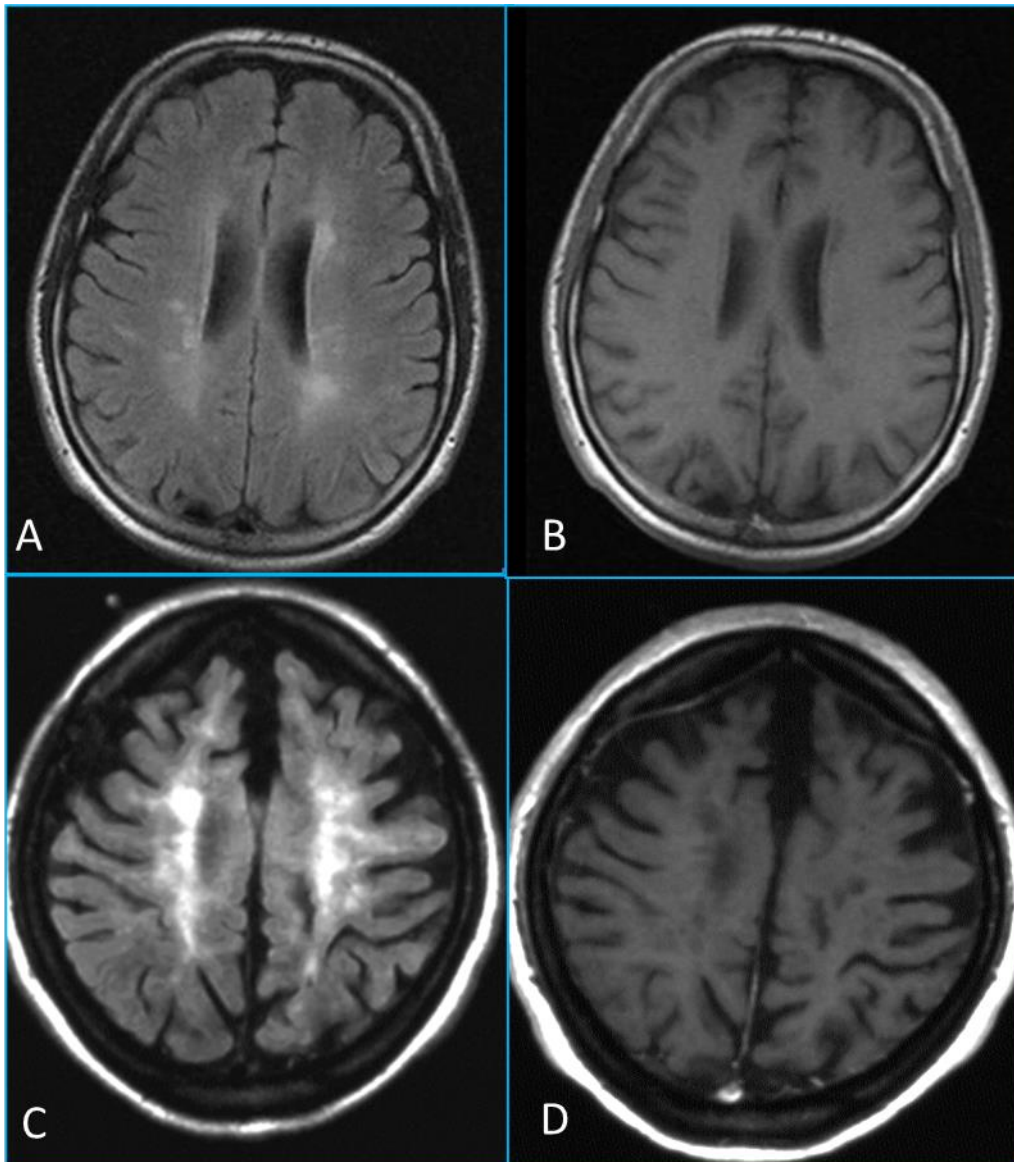


*Figure 10. Multiple demyelinating lesions in a patient with RRMS (A,B), appearing as hyperintense foci on FLAIR sequence (A) and variable SI on T1-w sequence (B), according to the degree of demyelination and axonal loss. In another patient with SPMS the demyelinating lesions appear as coalescent lesions in corona radiata, hyperintense on FLAIR (C) and severe hypointense (“black holes”) on T1-w (D)*

### 3.2 Using T2 sequences

MS lesions are depicted with increased SI on T2-w images, due to the increased water content, a finding that can be confirmed in every stage of plaque evolution, (Figure 10). The increased water contents in acute lesions is due to inflammatory edema, while in chronic lesions this can be attributed in demyelination and axonal

damage, resulting to increased levels of extracellular fluid, as well as in gliosis that increases the intracellular fluid (47). Demyelination and the implying local absence of lipids results in an hydrophilic environment that increases the T2 relaxation time, but this cannot be assumed the main reason of increased SI of MS lesions.

Focal hyperintense lesions on T2 sequences appear in almost every WM disease (ischemia, Acute Disseminated Encephalomyelitis –ADEM, Leukoencephalopathies, leukodystrophies etc.) (100). Thus T2-w sequences, although very sensitive in detecting MS pathology (100), they lack specificity.

FLAIR is a T2-w sequence with saturation of the water SI, and is very useful for the detection of MS lesions adjacent to the CSF (periventricular or juxtacortical), as well as the lesions of the corpus callosum, by using sagittal plane (101). It has been shown that more MS lesions were detected on FLAIR sequence, compared to the conventional T2-w sequences (102) (Figure 10).

The amount and the size of MS lesions (103) identified on T2-w sequences( T2 lesion “load”), vary among clinical subtypes of MS. RRMS patients have in average double newly appeared lesions, compared with patients with progressive types of the disease. Patients with SPMS are characterized from increased number of lesions, as well as increased number of infratentorial lesions, compared to those that are diagnosed with benign type of the disease (104). Finally, PPMS patients have fewer and smaller focal lesions in comparison with other types of the disease (101, 105).

### 3.3 Contrast Enhanced lesions

Gadolinium-based contrast agents (GBCAs) are widely used on T1-w sequences. The corresponding increased GBCA concentration implies decreased T1

relaxation time, thus increased SI. Signal increment is representative of the GBCA uptake in brain parenchyma, and is related to the corresponding GBCA concentration that is proportionate to the disruption of the BBB, the concentration of the GBCA in the arteries and the GBCA washout (10, 106).

CA uptake from MS lesions is correlated with local disruption of the BBB. The presence of inflammation on MS lesions is considered to be a prerequisite for CA uptake, considering that non-inflammatory demyelination with BBB disruption (107) has not been described, while in experimental allergic encephalomyelitis studies, the CA uptake was correlated with the number of inflammatory cells inside the lesions and the activity of the macrophages (107, 108). Thus, CA uptake from MS lesions can be attributed to the local inflammation that results to BBB disruption.

Cross-sectional MRI studies on MS patients (105, 109-112) confirm CA uptake within new, acute, MS lesions in RRMS and SPMS patients. Almost every newly formed lesion, enhances (79, 113-115). The duration of the enhancement ranges between 4-8 weeks for the majority of lesions, and maximum MR signal enhancement is reached within 29 mins after CA injection (115). This enhancement is heterogeneous, related to the heterogeneous pathology of the lesions and could be described as a) nodular, usually in newly formed lesions related to inflammation in NAWM vessels or b) ring shape, related to peripheral acute inflammation in chronic lesions (116-118) (Figure 11). In cases of ring-shaped CA enhancement in large MS lesions the ring is not complete("open ring sign"), and this helps in the differential diagnosis from other ring-enhancing lesions, such as metastases (119). Uptake can change during the same imaging session from ring shaped (2-5 minutes after CA injection) to nodular (15-20

minutes after CA injection), implying a lesser degree of BBB disruption at the center of the lesion, compared to its periphery (115).

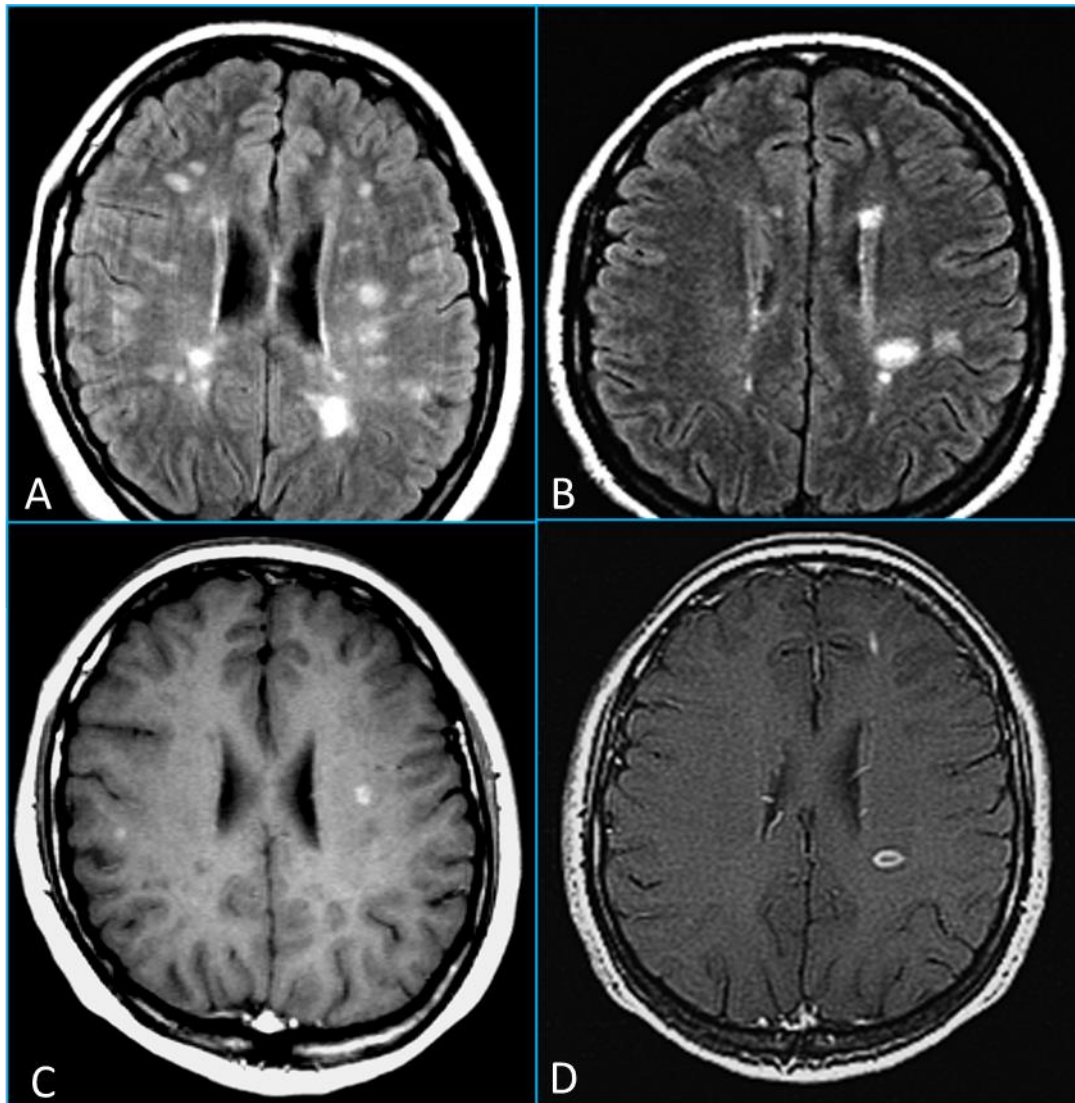


*Figure 11. Demyelinating lesions in two different cases of RRMS, appearing as hyperintense foci on FLAIR sequences (A, B). On post-Gadolinium T1-w sequences (C, D) some of the lesions enhance in a nodular, linear or ring-shape pattern, indicative of acute activity.*

The frequency of Gd enhancing MS plaques differs among the clinical subtypes of the disease. Patients with RRMS and SPMS are characterized by increased number of enhancing lesions compared with PPMS or benign MS patients (111, 120). Low uptake from PPMS patients probably is correlated with decreased inflammation, as

reported in a corresponding study (121). Moreover, the number of enhancing lesions increases before and during clinical relapses (110, 122, 123). In conclusion, contrast enhanced MRI constitutes a sensitive test for assessing disease activity and clinical evolution and for evaluating MS-treatment effectiveness.

The sensitivity of contrast enhanced MR for highlighting active lesions can be augmented by:

- a) increasing the time interval between the CA administration and the initialization of the sequence and resulting to 10-20% increased sensitivity (124, 125),
- b) administration of triple Gd dose (0.3 mmol/kg) resulting to 70-80% increased sensitivity (124, 126-128),
- c) simultaneous application of magnetization transfer imaging, which increases the sensitivity of the conventional T1-w sequence in detecting the enhancing lesions, by decreasing the signal intensity of the surrounded tissue (124, 129-131).

The aforementioned techniques indicate a heterogeneous pathological substrate of the enhancing lesions. Lesions detected only after triple dose of Gd or at later image acquisition after Gd administration, are characterized by less inflammatory elements and decreased BBB disruptions (10). Finally, the combination of the above techniques increases the sensitivity of MRI in the detection of the enhancing lesions, by 130% (124).

## 4 Contribution of MRI in the Diagnosis of MS

It has been widely recognized that MRI is more sensitive in detecting white matter abnormalities than CT. Young et al. (132) detected 19 lesions on CT and 112 more lesions on MRI in a cohort of 10 MS patients scanned at the same time with MR and CT. These lesions were characterized as MS plaques, MS lesions or WM lesions. Moreover, in the same study, as well as in a study from Runge et al. (133), it was reported that MS lesions follow different patterns of distribution, compared with other neurological conditions, mainly affecting the periventricular and infratentorial regions. The aforementioned studies recommended MRI as an imaging modality that facilitates the diagnosis of MS, and led to the development of the first diagnostic criteria for MS (134-136). Application of these MRI criteria can improve diagnosis by replacing the purely clinical criteria for dissemination in space (DIS) and time (DIT). The international panel McDonald criteria for MS diagnosis were proposed in 2001, based on results from relevant previous studies and established specific MR findings for dissemination of the lesions in space (DIS) and in time (DIT), These criteria were revised by in 2005 and 2010 (12, 137, 138) (Table 3).

*Table 3. Diagnostic criteria for multiple sclerosis: 2010 revisions to the McDonald criteria. Polman et al. Ann Neurol. 2011*

**McDonald 2010**

**Dissemination in Space**

1. Objective clinical evidence of at least 2 lesions or objective clinical evidence of 1 lesion with reasonable historical evidence of a prior attack involving a different CNS site
2. At least 1 T2 lesion in at least 2 of 4 MS-typical regions of the CNS:
  1. Periventricular
  2. Juxtacortical
  3. Infratentorial
  4. Spinal cord
  5. (Symptomatic lesions in patients with brainstem or spinal cord syndrome are excluded)

**Dissemination in Time**

3. At least 2 attacks separated by a period of at least 1 month
4. Simultaneous presence of asymptomatic gadolinium-enhancing and nonenhancing lesions at any time
5. A new T2 and/or gadolinium-enhancing lesion on follow-up MRI, irrespective of its timing with reference to a baseline scan

In 2017, new diagnostic criteria were proposed for MS in patients with a typical CIS (83, 139). These criteria are easier to apply than the McDonald 2010 criteria. The most important addition is that the new criteria allow MS diagnosis when the MRI scan meets criteria for DIS and unique oligoclonal bands (OCB) are present in CSF, even in absence of DIT on the MRI scan. The other major difference is that not only asymptomatic but also symptomatic lesions can be used to demonstrate DIS and DIT on MRI. Furthermore, cortical lesions can be used to demonstrate dissemination in space (Table 4)

*Table 4. Diagnostic criteria for multiple sclerosis: 2017 revisions to the McDonald criteria. Thomsson et al. Lancet Neurol. 2018*

**McDonald 2017**

**Dissemination in Space**

1. Objective clinical evidence of at least 2 lesions or objective clinical evidence of 1 lesion with reasonable historical evidence of a prior attack involving a different CNS site
2. At least 1 T2 lesion in at least 2 of 4 MS-typical regions of the CNS:
  1. Periventricular
  2. (Juxta)cortical
  3. Infratentorial
  4. Spinal cord

**Dissemination in Time**

1. At least 2 attacks separated by a period of at least 1 month
  2. Simultaneous presence of gadolinium-enhancing and nonenhancing lesions at any time
  3. A new T2 and/or gadolinium-enhancing lesion on follow-up MRI, irrespective of its timing with reference to a baseline scan
  4. Demonstration of CSF-specific OCBs (as substitute for demonstration of DIT)
- Abbreviations: CNS, central nervous system; CSF, cerebrospinal fluid; MRI, magnetic resonance imaging; OCB, oligoclonal bands.

In 2018 van der Vuurst de Vries RM et al evaluated the diagnostic accuracy of the 2017 criteria vs the 2010 criteria in prediction of clinically definite MS in 229 patients with a typical CIS and found that sensitivity for the 2017 criteria was higher than for the 2010 criteria, but specificity was lower (Table 5). Using the 2017 criteria (140), more MS diagnoses could be made at baseline, while in the group with at least 5 years of follow-up, 33% of patients who were diagnosed as having MS using the 2017 criteria did not experience a second attack during follow-up vs 23% when using the 2010 criteria. So, they concluded that the 2017 revision of the McDonald MS criteria leads to a higher number of MS diagnoses in patients with a less active disease course.

*Table 5. Test Characteristics for the 2010 and 2017 McDonald Criteria*

<b>Characteristic</b>	<b>DIS (n = 229)</b>	<b>DIT (n = 180)</b>	<b>DIS+DIT (n = 180)</b>
2010			
Sensitivity (95% CI)	66 (56-74)	36 (27-47)	36 (27-47)
Specificity (95% CI)	57 (47-66)	85 (76-92)	85 (76-92)
Accuracy (95% CI)	52 (45-58)	61 (54-68)	61 (54-68)

Characteristic	DIS (n = 229)	DIT (n = 180)	DIS+DIT (n = 180)
Hazard ratio (95% CI)	2.0 (1.3-2.9)	1.9 (1.2-2.9)	1.9 (1.2-2.9)
2017			
Sensitivity (95% CI)	79 (70-86)	84 (74-90)	68 (57-77)
Specificity (95% CI)	48 (39-58)	44 (34-55)	61 (50-71)
Accuracy (95% CI)	44 (38-51)	64 (57-71)	64 (57-71)
Hazard ratio (95% CI)	2.7 (1.7-4.2)	2.6 (1.5-4.6)	2.0 (1.3-3.1)

*Abbreviations: DIS, dissemination in space; DIT, dissemination in time; NPV, negative predictive value; PPV, positive predictive value (140).*

MRI is a great imaging modality for monitoring MS disease course, evaluate the response to treatment and facilitates the detection of side effects (84). Monitoring of MS disease activity by using MRI, is of great importance considering the ability to detect new, enlarged or contrast enhanced lesions. Gd administration is not mandatory but this is recommended since it simplifies the detection of newly appeared or even enlarged lesions (84). Moreover, it is strongly recommended that the MRI scans are repeated every year or when an unexpected event occurs. Considering that new immunomodulatory medicines are available which may result in serious complications, MRI is of great importance for differentiation between early Progressive Multifocal Leucoencephalopathy (PML) and new MS lesions (141).

## 5 Perfusion Imaging in MS

Perfusion is a general term for the displacement of molecules in liquids or gas stemming from a pressure gradient. In the human body perfusion is related to the transportation of blood to tissues, due to the pressure gradient from the heart, which forces the blood to circulate through the vessels, to supply tissues with oxygen and nutritional elements. Perfusion MRI is based on the measurement of hemodynamic parameters using the NMR principle (142). There are three main perfusion MRI techniques: a) Dynamic Susceptibility Contrast (DSC) (143), b) Dynamic Contrast Enhanced (DCE) (10) and Arterial Spin Labelling (ASL) (144). DSC and DCE perfusion MRI necessitate the intravenous Gadolinium injection while in ASL there is no need of CA.

### 5.1 DSC-Perfusion MRI

DSC perfusion MRI, incorporates the rapid intravenous Gd administration, while the brain is simultaneously being scanned using a dynamic imaging technique (145). At the time that Gd enters the vessels, a paramagnetic effect creates field inhomogeneities that leads to dephasing of magnetization. Signal acquisition using temporal resolution of 1-2 secs permits the measurement of Gd concentration over time, and the estimation of hemodynamic parameters, such as the cerebral blood flow (CBF), cerebral blood volume (CBV) and mean transit time (MTT). In more detail, CBF is the volume of blood passing through a given amount of brain tissue per unit of time. Most of the times CBF is difficult to be measured, and relative CBF is calculated that is normalized to WM. CBV is the volume of blood in a given amount of brain tissue, and it can be calculated through the area under the concentration curve. Due to the difficulty of direct measurement, most of the times it is calculated the relative CBV (rCBV- no units), that is normalized to an internal control area, such as contralateral

normal white matter. Finally, MTT is the average time (secs) that blood cells spend within a determinate volume of capillary circulation. The MTT is calculated as the fraction of CBV to CBF. In order to compute the DSC quantitative parameters, a deconvolution process with the pharmacokinetics of Gd in the feeding artery (arterial input function) has to take place, a procedure that is prone to errors (146), such as partial volume effects.

Typically, DSC is acquired using a fast sequence such as a gradient echo or a spin echo. The contrast agent is distributed in the tissue vasculature, in which it increases their paramagnetic effect and creates field inhomogeneities around them, that implies to accelerated dephasing of the magnetization. Through dynamic measurement of the signal, and using temporal resolution of 1-2 secs, the contrast agent concentration is being measured, and afterwards it is quantified to produce parametric maps of perfusion.

Moreover, simulations (147, 148) and image-based experiments (147) have shown that spin echo DSC is more sensitive to capillary size vessels, while gradient echo is sensitive in a wide variety of vessel size.

Imaging parameters that are typically used in gradient echo DSC are 3\*3mm voxel size and slice thickness of 3–5 mm. Considering that DSC imaging needs to capture the dynamics of CA entering and exiting the lesion, scan time duration is typically in the range of 1 to 3 mins (149-151). The TR is as short as possible, typically between 1 and 2 seconds. It is speculated that rapid using multiband MR will further decrease of MR imaging parameters, such as TR, having as a result the increased SNR,

the increased spatial resolution that reduces PVE (partial volume effects), thus the improved assessment of cortical perfusion (146).

A lot of research studies incorporated the DSC MRI technique in MS patients. Wuerfel et al analyzed Gd enhancing lesions from 20 patients with RRMS using a DSC study (152). They reported 20% increment in the CBF and CBV indices 3 weeks after the baseline imaging, while the time to peak (TTP) had 25% increase. In another study, it is reported that ring-enhancing lesions showed changes in the periphery, that consists the anatomical site of the maximal inflammation on MS (153). These findings constitute DSC perfusion MRI a highly sensitive technique to inflammatory activity, and changes to BBB are able to be depicted before and after its disruption. Moreover, some DSC studies have also shown that contrast enhancing lesions have increased CBV and CBF values compared to the NAWM regions (149, 154), while a study from Ge et al. (149) didn't found any difference on the aforementioned areas. However, T1 severe hypointense lesions (black holes), have been found to have lower CBV values compared the iso-intense and WM from healthy controls (154, 155), while T1 isointense lesions had not difference compared to healthy controls WM.

In a study from Peruzzo et al. cortical lesions of 44 RRMS patients were examined, using DSC MRI (151). It was reported that the majority of the cortical lesions have CBF and CBV values significantly lower values compared to the NAWM, while some lesions showed increased perfusion parameters, a fact that was attributes to acute inflammation.

Cross-sectional studies using DSC perfusion demonstrated statistically significantly reduced CBF or/and CBV values and increased MTT in the NAWM of MS

patients compared to healthy controls (149, 150, 156-160). A report from Rashid in 60 MS patients with various phenotypes, found increased and heterogeneous WM perfusion (161). In another study on NAWM areas of 17 RRMS patients, Law et al. (158) reported reduced CBF and increased MTT in the absence of CBV changes as compared to healthy controls.

In a number of studies, decreased perfusion values have also been found in deep and cortical GM of patients with MS compared to healthy controls (157, 160-165). Moreover, reduced perfusion in cortical areas and deep gray matter was reported in previous studies concerning early RRMS patients (157, 165). Finally, Debernard et al. (157) in a study on 25 early RRMS patients, reported that the aforementioned findings are correlated with visual and verbal memory impairment. To sum up, perfusion parameters are of great importance as imaging biomarkers of early MS as they may precede structural atrophy.

There is a lot of interest on perfusion measures in different MS phenotypes. Previous research on early RRMS cohorts reported decreased perfusion in NAWM and GM (157, 162, 165). Studies on CIS patients reported CBF decrease in periventricular NAWM or deep GM when compared with healthy controls (165, 166).

Difference in perfusion parameters among the RRMS and PPMS groups are not consistently confirmed. However, there are studies reporting decreased perfusion parameters in NAWM of PPMS compared to RRMS patients (150, 156, 161, 167). Adhya et al. (156), reported decrease on CBF and CBV values in periventricular NAWM and decreased CBV in frontal NAWM but not significant differences in other NAWM regions. This is in line with the aforementioned reports on CIS and early RRMS patients

and indicates that periventricular NAWM perfusion tends to decrease in progressive disease. It Decreased cortical GM CBF has also been reported in SPMS patients compared to RRMS, but not persisted after controlling for factors such age, sex, disease duration and T2 lesion volume (167).

Although perfusion abnormalities have been found in several MS cohorts, the correlation of these measures with indices of clinical disability and disease severity is not yet strongly established. There are no associations among the EDSS score or the disease duration and the perfusion parameters of NAWM or GM in CIS and RRMS patients, according to different studies (150, 154, 157, 160, 161, 163-166). Adhya et al (156) and Bester et al. (168) reported that there was no correlation between the EDSS and perfusion parameters (CBF, CBV) in NAWM of MS patients. In another study including 23 RRMS patients negative association among hypo perfusion in thalami and the time to complete the 9-Hole Peg test was reported (164). 9-Hole Peg Test focuses to the upper extremity motor function, although it is considered to predict disease progression with adequate accuracy (169). It is speculated that the absence of correlation among the perfusion parameters and measures of disability may be due to the low sensitivity of the latter to predict disability, while EDSS has been criticized for its high variability among examiners (170). Moreover, Gd enhancing or T2 lesions do not efficiently predicts the long-term disability, also (170). However, effectiveness of the perfusion MR parameters lies in the detection of acute inflammatory changes prior to the conventional MRI (152), and the earlier identification of symptomatic and asymptomatic disease activity. In Table 6 there is a summary of the main DSC perfusion MRI findings in MS (76, 146, 149, 154).

Table 6. Summary of DSC perfusion studies in MS (146)

	Active Lesions	Chronic Lesions	NAWM	Deep Gray Matter
<b>CBF</b>	↑ (Compared with NAWM)	↓ (Compared with NAWM and WM in controls)	↓ (Compared with WM in controls)	↓ (Compared with controls)
<b>CBV</b>	↑ (Compared with NAWM)	↓ (Compared with NAWM)	↓ (Compared with NAWM)	↓ (Compared with controls)
<b>MTT</b>	No significant change	↑ (Compared with WM in controls)	↑ (Compared with WM in controls)	↑ (Compared with controls)

## 5.2 DCE perfusion MRI

DCE-MRI is a quantitative MRI technique able to detect and quantify the disruption of the BBB. It comprises of the dynamic acquisition of multiple T1-w images before, during and after the administration of a paramagnetic contrast agent, resulting in a dynamic SI over time for every lesion that enhances CA (8, 9). Many compartmental models have been proposed in order to quantify the CA PK, from very simple implementations that assume a single compartment, to complex models incorporating multiple compartments in which CA is being transferred. PK analysis of DCE data, was first proposed by Tofts (10) for MS active lesions, and afterwards widely applied in clinical practice, especially to brain tumors (9).

Several studies examined the integrity of the BBB in MS patients utilizing the DCE-MRI technique (8, 171, 172). Considering the low-grade enhancement appearing in the MS lesions and the peripheral NAWM, some studies have been focusing on examining the acquisition and protocol parameters, as well as, the model selection, in order to have a more robust quantification of the BBB disruptions in the aforementioned areas.

Cramer et al. studied DCE-MRI exams from simulated, healthy tissue and MS patient data in order to argue about model selection, as well as temporal and total measurement duration on DCE-MRI (3). Patlak model was proved to be the

appropriate model for estimation of BBB on tissues with low permeability, while for higher permeabilities, a more complex model, such as the extended Tofts, was suggested.

Barnes et al. investigated the optimal acquisition and model parameters of DCE MRI in order to quantify small BBB leakages (173). They examined parameters such as pharmacokinetic model selection (Patlak (174), extended Tofts (175), or 2CXM (176)), scan duration, temporal resolution, signal drift and length of baseline acquisition, by analyzing both humans (n=6) and simulated time curves and defined a metric, the so-called k-CNR, as a measure of precision and contrast, for the detection of small permeabilities changes. They concluded that Patlak model results in better identification of subtle BBB disruptions, combined with long acquisition times (10-30 mins), baseline scans among 1 to 4 mins and temporal resolution less than one minute.

Jelescu et al. studied 4 RRMS patients and proposed a dual temporal resolution protocol for better quantification of the BBB permeability in active MS lesions (177). This protocol consisted of an initial part with high temporal and low spatial resolution lasting for about 1 minute, in order to better capture the first-pass bolus, and a second part with low temporal resolution and high spatial resolution, lasting for about 20 minutes, that is essential to properly detect and segment the active MS lesions. They reported that this novel protocol improved measurement accuracy and precision compared to the conventional DCE protocol, with the corresponding simulating errors on ktrans to be 7%-10% for the dual temporal resolution protocol, versus 7%-30% for the conventional DCE protocol.

To this end, and considering reports from previous studies of low BBB leakage on visibly non-enhancing MS lesions, NAWM and healthy WM on conventional T1 sequences (24, 178-180), more recent investigators tried either to quantify or just detect these subtle BBB disruptions through the usage of DCE-MRI, while some of them compared these findings with results from healthy brains. Soon et al. studied 27 RRMS patients after natalizumab therapy and 13 placebo patients with DCE-MRI data. Regions of interest were placed on non-enhancing lesions and NAWM areas, and BBB leakage was assessed based on SI changes, concluding that there is a subtle BBB leakage in visibly non-enhancing MS lesions (4). Ingrisich et al. (76) studied enhancing, non-enhancing lesions and NAWM areas in 19 MS patients using DCE MRI data, in order to examine the BBB. They found statistically significant different perfusion parameters (CBF, CBV, permeability) in enhancing lesions compared to NAWM. In non-enhancing lesions only the CBV parameter was weakly increased ( $p < 0.05$ ), compared to the NAWM.

Xiong et al. (181) studied 27 RRMS patients using DCE-MRI technique with the Patlak model (174) and focused on enhancing and non-enhancing lesions and NAWM areas. They examined the perfusion parameters, as well as their correlations with Expanded Disability Status Scale (EDSS) and disease duration. They found that the perfusion parameters were significantly higher ( $p < 0.05$ ) in enhancing lesions compared to non-enhancing lesions and NAWM areas, but no correlation was found with the EDSS scores and the disease duration. In another study Yin et al. (182) examined 30 RRMS patients using DCE-MRI and the extended Tofts model (175) and found that the perfusion parameters ( $k_{trans}$ ,  $k_{ep}$ ,  $v_e$ ,  $v_p$ , CBF and CBV) were

significantly higher in enhancing lesions compared to non-enhancing lesions and NAWM areas, but without any correlation with the EDSS scores and disease duration.

NAWM on conventional MRI sequences has been proved to be diffusely affected in MS patients. Lund et al. (183) performed a T1 relaxometry study the T1 relaxation in 59 RRMS patients and 9 healthy controls before and after the intravenous Gd administration and calculated T1 relaxation times in NAWM of the patients and the total cerebral white matter of the healthy control subjects. They found increased T1 relaxation times in NAWM of the RRMS patients compared to those of the control group, both at the baseline and after the CA administration, attributed to BBB disruption in MS. Cramer et al in investigated the BBB disruption of the NAWM in RRMS patients, using DCE-perfusion MRI (25) and comparing the periventricular NAWM and thalamic GM  $k_{trans}$  values between 27 MS patients and 24 healthy volunteers. They found that vessel permeability in the examined regions was significantly higher in MS patients compared to healthy controls. In another study Cramer et al. (184) examined 39 patients with monosymptomatic optic neuritis and 18 healthy controls with DCE-perfusion MRI. They found that increased permeability in NAWM is correlated with increased risk to MS conversion from optic neuritis.

Ingrisch et al. (5) studied DCE exams from 24 RRMS patients and 16 controls, in order to compare the perfusion parameters between the two groups. Regions of interest were placed in the frontal, periventricular, and occipital NAWM, as well as in the thalami and the pons, and perfusion parameters (CBF, CBV, Permeability Surface (PS)) were calculated using a compartment uptake model, but without establishing any significant difference.

Varatharaj et al. (185) examined the BBB leakage in 13 controls and 12 RRMS patients through quantification of DCE-MRI data, by using the Patlak model. They examined GM, NAWM and contrast enhancing MS lesions and found increased permeability ranging from NWM of controls, to NAWM of MS patients and contrast enhancing MS lesions.

Subtle BBB abnormalities in other neurodegenerative diseases, different from MS, have been quantified by DCE perfusion MRI. It is worth mentioning the study from Armitage et al., who examined the DCE-MRI exams of 60 patients with mild ischemic stroke in order to investigate whether scanner noise, drift, intrinsic tissue properties and imaging parameters affect the physiological interpretation of the perfusion results when studying subtle BBB disruptions (186). They did not find any significant differences among patients with different degree of white matter abnormalities, but they concluded that when trying to quantify subtle BBB disruptions, the influence of noise, drift, and tissue parameters should be considered. Haar et al. (187) studied 16 patients with early Alzheimer disease and 17 healthy controls using a dual temporal resolution protocol (177), in order to improve measurement accuracy and sensitivity in neurodegenerative diseases, characterized by low BBB disruption. They found that leakage rate was very low and the measurement is highly influenced by noise, resulting in overestimated permeability values at shorter scan times. Moreover, they reported that the volume fraction of detectable leaking tissue is an alternative measure to detect group differences in Alzheimer disease.

Finally, it is of great interest to report two previous studies that tried to quantify BBB abnormalities on MS, by examining also the late dynamics of the signal

enhancement after Gd administration. Gaitan et al. (188) studied 80 RRMS patients separated in 3 groups according to EDSS. T1-weighted images were acquired prior and after Gd administration, up to 60 mins and they report that enhancing lesions have 3 concentric areas: a) the central region, b) the intermediate region and c) the peripheral region, with their morphology to be consistent with antigen-specific adaptive immune reaction. Soon et al. studied 19 patients with clinical definite MS (9 secondary progressive MS, 10 RRMS), with a total of 581 visibly non-enhancing lesions (343 SPMS, 238 RRMS) and paired contralateral normal appearing brain tissue (NABT) (189) and estimated the BBB leakage in terms of changes in T1 relaxation times 20, 40 and 60 mins after Gd injection. They found that visibly non-enhancing MS lesions showed increased T1 relaxation time compared with the corresponding NABT at every time point. Shinohara et al. (190) studied enhancing lesions of 10 MS patients, using T1 weighted acquisitions up to 155 mins after Gd injection. They analyzed the lesion enhancement curves using a model free approach by performing a Functional Principal Component Analysis (FPCA) within and across subjects. Their analysis provided measures of spatiotemporal enhancement patterns in MS lesions, taking into account measures of magnitude, rate shape and dynamics.

In conclusion, DCE sequence provide physiological parameters related to the BBB disruption, and thus it seems to be a sensitive imaging method for detecting focal inflammatory activity of the brain. According to previous studies, Patlak model is the more accurate to subtle BBB disruptions, but there is a lack of accuracy in higher permeabilities. Furthermore, the reported quantification of permeability measurements follows an increasing trend from white matter areas stemming from healthy controls, NAWM areas in MS patients, non-enhancing lesions and enhancing

lesions. Most importantly, there is a subtle BBB leakage in visibly non-enhancing MS lesions. Finally, increased DCE acquisitions times may provide more accurate permeability quantification when studying subtle BBB disruptions.

## 6 Pharmacokinetic (PK) analysis of perfusion MRI studies

Imaging modalities such as MRI, PET and CT have been used to non-invasively assess tissue perfusion, by means of imaging biomarkers that can be related to pathophysiology of variable brain diseases (191).

DCE is an MRI method that has been used to assess perfusion in various anatomical regions. It is comprised of the acquisition of dynamic T1 weighted sequences before during and after the intravenous injection of a paramagnetic contrast agent (CA). The dynamics of the signal intensity in every pixel of the examined area contain tissue-specific hemodynamic information related to pathophysiology of different CNS diseases. In clinical practice main applications include differential diagnosis, grading and classification of different tumor types (192, 193). For this purpose, radiologists mainly use a subjective evaluation of the shape of the enhancement curves. Although this approach is simple and easy to be performed, it doesn't provide quantifiable markers that can be further processed and used particularly in comparative research studies. A variety of analysis techniques have been adopted in the past years for quantifying the DCE–MRI data, which range from simple measures of the SI enhancement to complex models that quantify parameters of the underlying physiology. In the following sections we examine in detail the PK modelling approach that is frequently used in order to provide objective, quantitative hemodynamic measures based on DCE data analysis. We also review the application of model free methods for the classification of tissue curves in classes that demonstrate different physiological meaning.

## 6.1 Reliability of pharmacokinetic (PK) biomarkers

Many factors might affect the reliability of the quantitative biomarkers from a DCE experiment. A first prerequisite is a well-designed DCE protocol, which implies the careful selection of appropriate parameters, such as repetition time (TR), echo time (TE), flip angle (FA) and the field of view (FOV) (194). As a general recommendation, TR should be as low as possible, to ensure an efficient temporal resolution, while TE should be minimized for the elimination of T2\* contribution in the signal of the image. The compromise among spatial and temporal resolution should also be taken in account, as well the overall acquisition time of the DCE protocol (195).

Concerning the contrast agent (CA), the selection of the type of the tracer is of major importance, as well as, the dose injected and the rate of injection (196). It should be noted that the clearance rate of the CA, which is closely related to the organ of excretion, can influence the PK analysis. Some dynamic volumes, usually 3 to 6 scans, should be acquired prior to injection to form the so-called baseline acquisitions, in order to determine the injection time accurately.

Pre-processing tasks usually include motion correction of the dynamic sequences, where co-registration is carried out with respect to the arterial phase of the DCE, due to the higher signal to noise ratio (SNR). Also, temporal smoothing of the dynamic curves per pixel can reduce signal distortions.

During the PK modeling, there several other issues that need to be addressed. The selection of Region Of Interest (ROI) for tissue and artery need to be annotated from expert radiologists, while the role of the hematocrit (HCT) should be taken in account when possible (197). Critical issues for the accurate quantification of the DCE

data include: a) the conversion of SIs of the artery and tissue to CA concentration, b) the selection of the Arterial Input Function (AIF) region of interest or the assumption of a theoretical one and c) the selection of the PK model that the data will be fitted.

## 6.2 Estimation of contrast agent concentration

In some studies, there is a direct processing of the SIs, but this can lead to erroneous results due to non-linear relationship of SI with concentration, especially in tissues with higher CA concentrations (198). These non-linearities are dependent on factors such as native T1 relaxation time of the examined tissue and MRI acquisition parameters (199). It is therefore recommended to convert both tissue and artery SIs to CA concentration for a more robust analysis. The main techniques for measuring T1 relaxation time are the inversion recovery (200), the Look-Locker method using an EPI protocol (201) and the multiple flip angles (FAs) using SPGR protocols (202). The latter method is widely used in DCE-MRI due to the high SNR and time efficiency (203) offered. It requires two or more FAs for the determination of the pre-contrast T10 relaxation time of the tissue. The CA concentration at time t is related to the change in relaxation time via the following formula:

$$C(t) = \frac{1}{r_1} \cdot \left( \frac{1}{T_1(t)} - \frac{1}{T_{10}} \right) \quad (1)$$

where  $r_1$  is the longitudinal relaxivity of the CA,  $T_{10}$  is the longitudinal relaxation time prior to CA administration, and  $T_1(t)$  is the longitudinal relaxation at time t after the injection of CA.

The MR SI from a spoiled gradient echo with echo time  $TE \ll T_2^*$  is given from the following equation:

$$S_1 = S_0 \cdot \sin(\alpha_f) \frac{1 - e^{-TR/T_{10}}}{1 - \cos(\alpha_f)e^{-TR/T_{10}}} \quad (2)$$

where  $T_{10}$  is the longitudinal relaxation time prior to CA administration, and  $\alpha_f$  is the flip angle used and  $S_0$  is the relaxed signal for a  $90^\circ$  pulse. Acquiring multiple acquisitions, two or more, using different flip angles, the longitudinal relaxation time  $T_{10}$  and the relaxed signal  $S_0$  can be estimated, and afterwards the time course of the  $T_1(t)$  can also be computed.

### 6.3 Arterial Input Function (AIF)

AIF describes the concentration of the CA during time in the artery that supplies the tissue of interest. The selection of AIF is also critical for the PK modelling procedure and affects the reproducibility and the reliability of the results (204). In almost all PK models, AIF has to be determined for an accurate analysis. This process maybe hampered by a number of issues including the partial volume effect, non-linear effects, flow artifacts and patient motion during acquisition (205). There is a variety of techniques to either directly measure or determine AIF. The most frequently used techniques are discussed below.

Intravenous measurement is the determination of CA concentration in the artery by collecting blood samples over time and analyzing them (206). This is the most reliable procedure that provides accurate measurements of CA concentration, with major drawback the invasive process and lacking of temporal resolution.

Direct measurement of plasma concentration from the field of view (FOV) of the MR image is a method that consists of measuring the AIF from an artery, or from a vein (207), close to the tissue under examination. Having the prerequisite that an artery is included in the FOV of the DCE exam, the SI from a ROI annotated from an

experienced operator is converted to CA concentration as stated in section 6.2. The reliability of the AIF measurement in this method is direct dependent on the parameters of the MRI protocol, along with the spatial and temporal resolution of the data-set. Moreover, inherent weaknesses of this procedure that can bias the resulted plasma concentration are the partial volume effects (207), inflow effects (208), blood flow pulsatility and turbulence (209). Finally, it is important to note that ideally AIF should be determined in an artery close to the tissue under examination and its diameter should exceed the resolution of the dynamic image (210).

Population based AIF is an alternative method that overcomes many of the aforementioned problems, wherein several measurements are accomplished in a cohort of subjects and the mean of the individuals' measurements is considered. There are relevant studies that compare the individualized versus the population-based AIFs in several anatomical sites and demonstrate that under several circumstances a good correspondence among these different approaches can be achieved (211, 212). A well-known approach is from Weimann et al. (213), who proved that plasma concentration follows bi-exponential decay, and the corresponding formula is:

$$C_a(t) = D \cdot (a_1 e^{-m_1 \cdot t} + a_2 e^{-m_2 \cdot t}) \quad (3)$$

where  $C_a$  is the AIF,  $D$  is the CA dose ( $\text{mM} \cdot \text{kg}^{-1}$  of body weight),  $a_1=3.99$  kg and  $a_2=4.78$  kg are the amplitudes of the exponentials,  $m_1=0.144 \text{ min}^{-1}$  and  $m_2=0.011 \text{ min}^{-1}$  are their rate constants (10).

An alternative method for the calculation of plasma concentration that overcomes the possible lack of artery in the field of view, is the reference tissue based

AIF (214). In this method AIF is extracted from reference healthy tissues with known PK parameters, by employing the reference tissue concentration and its PK parameters. This procedure can be applied to single, double or multiple reference tissues (215, 216). Another approach to evaluate tracer PK parameters is through in-silico model-based approaches, such as physiologically-based pharmacokinetic models (PBPK) (217). PBPK models integrate data by taking into account drug – dependent (i.e. physicochemical properties, lipophilicity etc.) and physiological related parameters (i.e. body weight, height, blood flow, organ volume, protein binding, kidney function, genetics etc.) as well as, their variation among individuals (218). To this respect, it could not go unnoticed their potential application in DCE-MRI and particularly for the in-silico evaluation of tracer kinetics and AIF estimation (217, 219). The evaluation of tracer kinetics through the application of PBPK models shows promising results especially for estimation of c-t profiles of CA that could be compared with the previous mentioned AIF tracking methods (Figure 12) (220).

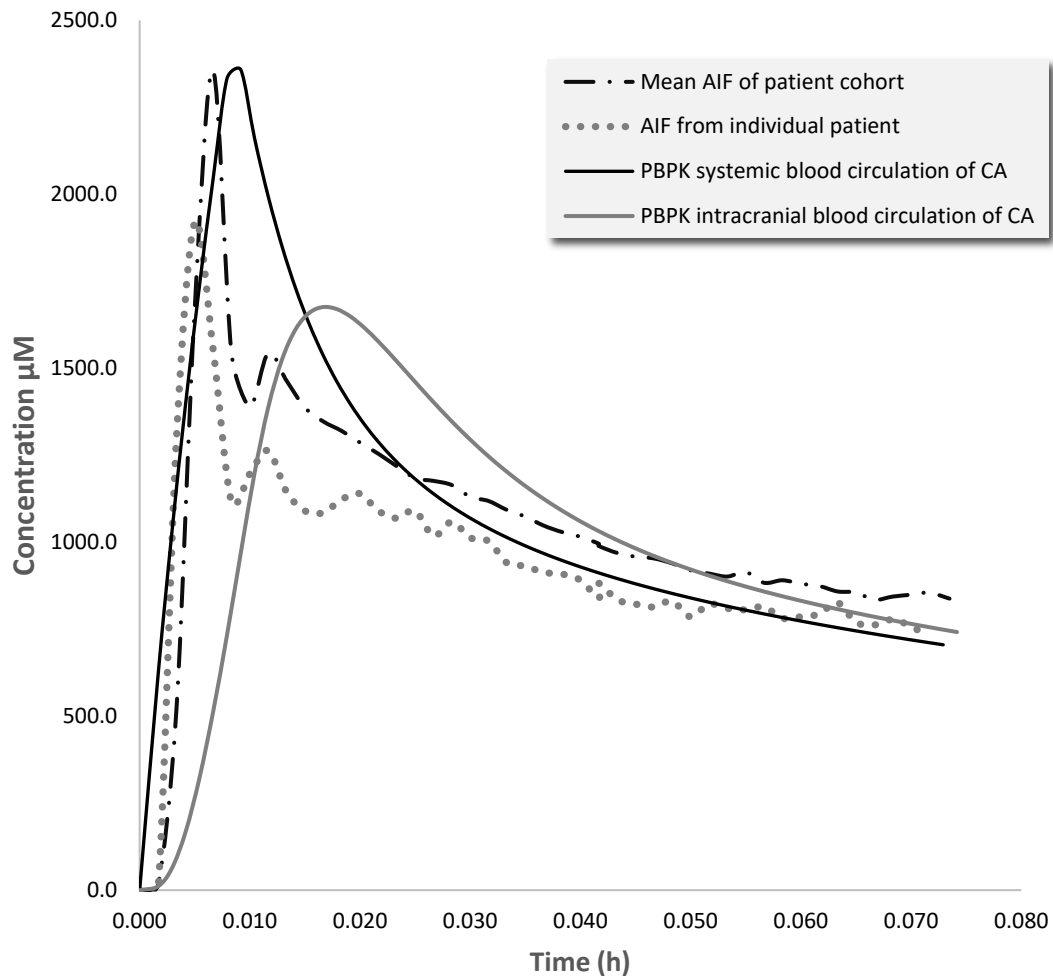


Figure 12. Concentration –time profiles of a CA. Dashed lines represent the measured AIF of a population mean (-.-) and individual patient (...) whereas straight lines represent the simulated through PBPK models c-t profiles of the same tracer regarding systemic (black line) and brain (grey) blood circulation. Simulations were generated in Simcyp® population pharmacokinetics platform ([www.certara.com/software/pbpbk-modeling/simcyp-pbpbk/](http://www.certara.com/software/pbpbk-modeling/simcyp-pbpbk/)) and were adopted from reference (221).

#### 6.4 Quantitative Models

Tracer kinetics can be described by systems theory under the assumption that tissues under examination are linear time-invariant systems. Under this assumption and considering the intravascular and the extravascular extracellular space (EES) as two distinct compartments, as shown on Figure 13, system behavior is described by the following set of equations:

$$C_v(t) = F \cdot R_v(t) \otimes C_a(t) \quad (4)$$

$$C_p(t) = F \cdot R_p(t) \otimes C_a(t) \quad (5)$$

$$C_t(t) = F \cdot (R_v(t) + R_p(t)) \otimes C_a(t) \quad (6)$$

where  $C_v(t)$  is the CA concentration in the vascular bed,  $C_p(t)$  is the CA concentration in the parenchyma,  $C_t(t)$  is the total tissue concentration,  $R(t)$  is the corresponding impulse response function and  $\otimes$  represents convolution. There are a few number of models that under several assumptions fit the DCE-MRI data into this set of equations, thus yielding quantitative measurements of tissue physiology. Tofts et al. published a standard set of names and symbols for these quantitative models (222) while comparative studies among these different approaches and thoroughly reviews concerning models can be found in the literature (9, 223). The most common models are presented and contrasted below.

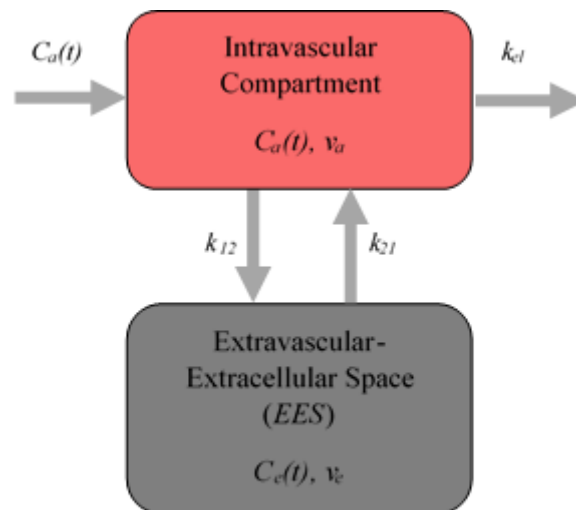


*Figure 13. A general representation of the two-compartment model. The first compartment illustrates the plasma with fractional volume  $v_a$  and the corresponding concentration  $C_a(t)$ . The second compartment represents the tissue space, which*

consists of the extravascular- extracellular space (EES), with corresponding fractional volume  $v_e$  and concentration  $C_e(t)$ .

An exemplary depiction of the PK parameters of an MS patient are depicted in Figure 14. It can be noticed the increased permeability of the active MS lesion compared to the surrounding tissue and the several anatomical regions, as well as the CA concentrations in several anatomical regions from a MS patient and a healthy control.

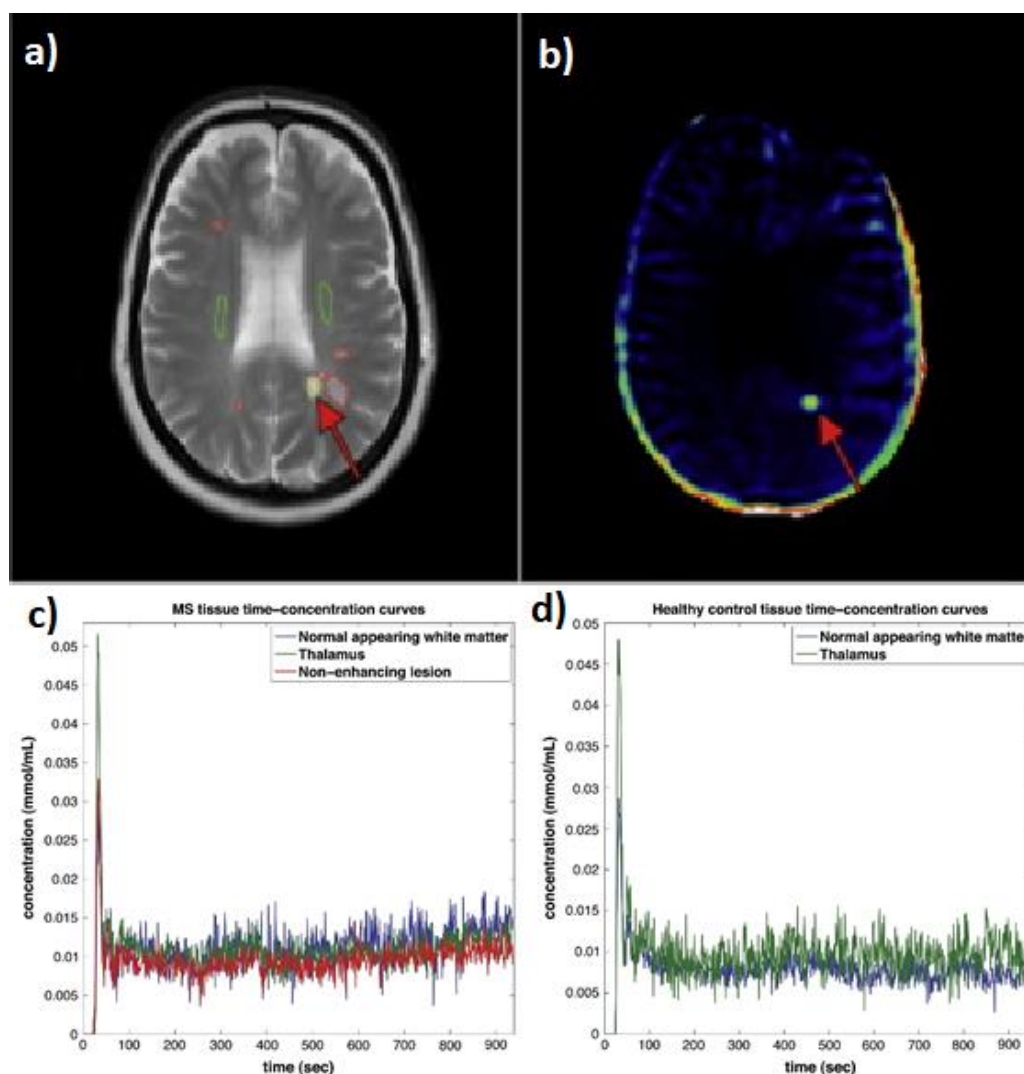


Figure 14. In a) there are depicted the regions of interest in periventricular normal appearing white matter (green), non-enhancing MS lesions (red) and contrast-enhancing MS lesions (yellow). In b) there is depicted the  $k_{trans}$  map computed by Patlak model. In c) and d) there are the concentrations over time in several anatomical regions for an MS patient and a healthy control (25).

#### 6.4.1 Tofts (TM) and Extended Tofts Model (ETM)

One of the most used models in literature is the Tofts model (TM) (10), a single-compartment model where the plasma space is ignored and the CA is moving to the parenchyma with a rate proportional to the difference of the concentrations between plasma and EES. The model is described by the following equation:

$$\frac{dC_t(t)}{dt} = k^{trans} \cdot \left( C_a(t) - \frac{C_t(t)}{v_e} \right) \quad (7)$$

Using the convolution theorem, the solution of previous equation is given next:

$$R_v(t) = 0 \quad (8)$$

$$R_p(t) = k^{trans} / F \cdot e^{-k_{ep} \cdot t} \quad (9)$$

In the above equations,  $k^{trans}$  represents the volume transfer constant from plasma space to EES,  $v_e$  is the fractional volume of EES and  $k_{ep} = k^{trans} / v_e$  is the transfer constant from EES to the plasma space. The omission of the plasma space was invalid for many tissues, resulted in erroneous PK biomarkers, thus Tofts extended the original model by introducing the vascular term as an external compartment. The result was to separate the enhancement caused by contrast leakage from that caused by intravascular contrast. The extended Tofts model (ETM) (175) is described by the following equation:

$$R_v(t) = u_p \cdot \delta(t) / F \quad (10)$$

$$R_p(t) = k^{trans} / F \cdot e^{-k_{ep} \cdot t} \quad (11)$$

where  $v_p$  is the fractional volume of vascular space. A major weakness of these models is that  $k^{trans}$  can be depicted either as plasma flow in flow-limited cases or as tissue permeability in permeability-limited cases. Another drawback is that TM is accurate

only in weakly vascularized tissues, while ETM is also accurate in highly perfused tissues, whereas in intermediate instances the validity of these models is ambiguous (224). However, what led to widespread usage of these models, is the simplicity on their interpretation and the fact that they provide useful biomarkers even in data-sets acquired in low temporal resolution.

#### 6.4.2 Adiabatic Tissue Homogeneity Model (ATH)

This model belongs to the spatially distributed kinetic models due to the fact that it accounts both temporal and spatial distribution of the CA concentration(225). The adiabatic approximation is used, which assumes that CA concentration in EES varies slow in comparison with that in intravascular space and as a result  $C_t(t)$  can be assumed as constant during small time intervals  $\Delta t$ . Using this assumption a closed form solution can be derived in the time domain, while its predecessor the tissue homogeneity (TH) (226), provides closed form solution only in Laplace space. This is a more complex model compared with TM - ETM but it also accounts plasma flow rate, extraction fraction and mean capillary transit time. The impulse response functions for the vascular and parenchyma compartments of this model are given by the following equations:

$$R_v(t) = (1 - u(t - t_c)) \quad (12)$$

$$R_p(t) = (E \cdot e^{-k_{ep}(t-t_c)} \cdot u(t - t_c)) \quad (13)$$

#### 6.4.3 Two Compartment Exchange Model (2CXM)

This is a two compartment model (227) that models plasma and EES as different compartments. Moreover, it allows for separate estimation of permeability and blood flow, thus resulting in a four-dimensional estimated vector  $[v_e, v_p, F_p, E]$ .

The model is described by the following set of equations:

$$R_v(t) = (1 - E_+) \cdot e^{-t/T_-} \quad (14)$$

$$R_p(t) = E_+ \cdot e^{-t/T_+} \quad (15)$$

where parameters  $E_+$ ,  $T_-$ ,  $T_+$  are function of  $F_p$ ,  $v_p$ ,  $v_e$  and  $PS$ . The main advantage of this model is the separate estimation of regional blood flow and capillary permeability. On the other side, the limitation of the 2CXM is the assumption of the well mixed tissue compartments, as well as the complexity of the fitting procedure due to the plethora of estimated parameters. The initial condition of the estimated vector, the temporal sampling and the SNR of the data are of major significance for the reliability of the model parameters.

#### 6.4.4 Distributed-Capillary Adiabatic Tissue Homogeneity Model (DCATH)

The DCATH model (228) considers the distribution of transit times through the multiple pathways of the tissue, while each of this pathways behaves equivalently to the ATH model. The probability of the distribution of transit times can have three different forms: a normal distribution, a corrected normal and a skewed Gaussian. This is actually the added value of the model, the quantification of the capillaries distribution by the time needed the blood to pass through the tissue. Thus, this model estimates the mean intravascular transit time as well as the distribution of transit times for each tissue pixel. The vascular and the parenchyma impulse response functions of the model are described by the following formulas:

$$R_v(t) = 1 - \int_0^t D(u) \cdot du \quad (16)$$

$$R_p(t) = E \cdot \int_0^t D(u) \cdot e^{-k_{ep}(t-u)} \cdot du \quad (17)$$

where  $D(u)$  is the regarding distribution. Further, the variability in transit times can be correlated with hypoxia, that can be related to the abnormal vascular structure of abnormal tissues (229) and the increased transit times due to the longer pathways.

#### 6.4.5 Gamma Capillary Transit Time model (GCTT)

The gamma capillary transit time (GCTT) model (230) is a generalized impulse response model that unifies four of the above models, TM, ETM, 2CXM and the ATH model. A major drawback of these models is the assumption that every pixel is a single capillary tissue with a single capillary transit time. The DCATH model overcame this by introducing a statistical distribution of the transit times in the impulse response function. However this exertion failed since unrealistic results were presented as well as a closed form solution was not feasible in every case of statistical distributions (230).

In GCTT model, the assumption that capillary transit times are described by the gamma distribution overcame the aforementioned problems and resulted in a new parameter,  $\alpha^{-1}$ , which is defined as the width of the distribution of capillary transit times and represents the heterogeneity of tissue microcirculation and microvasculature (230, 231). Mathematically, the parameter  $\alpha^{-1}$  is expressed by the following equation:

$$\alpha = \frac{t_c}{\tau} \quad (18)$$

where  $\tau$  is the scale parameter of the gamma distribution and  $t_c$  is the capillary transit time. The vascular and parenchymal impulse response functions of the GCTT model are given by the following equations:

$$R_v^{GCTT}(t) = \gamma\left(\frac{1}{\alpha^{-1}}, \frac{t}{\tau}\right) \quad (19)$$

$$R_p^{GCTT}(t) = \frac{Ee^{-k_{ep}t}}{(1-k_{ep}\tau)^{1/a-1}} \left[ 1 - \gamma\left(\frac{1}{a-1}, \left(\frac{1}{\tau} - k_{ep}\right)t\right) \right] \quad (20)$$

where  $D(u)$  is the gamma distribution of capillary transit times and  $\gamma$  is the upper incomplete gamma function.

### 6.5 Model Free Analysis

All model-free approaches to DCE-MRI data directly analyze the patterns of the dynamic curves, either considering the mean of the ROI curves or analyzing every pixel as a single entity. Widely used markers are the maximum of the SI, the time to peak, and the wash-in and wash-out rates (232, 233), while several of these parameters have been proposed as measurements that are correlated with response to treatment (234).

Another type of model-free analysis focuses on the shape of the tissue curves and classify them in predefined tissue types. The shape of the tissue curve can vary across a wide range of patterns (as shown in Figure 15), with the most common being:

- Type 1: steady enhancement of the SI
- Type 2: enhancement followed by plateau
- Type 3: enhancement followed by wash-out

The type of the curve is indicative of a specific tissue pathophysiology. For example, Type 3 curves, are usually considered as the most suspicious for underlying malignant neoplastic tissue.

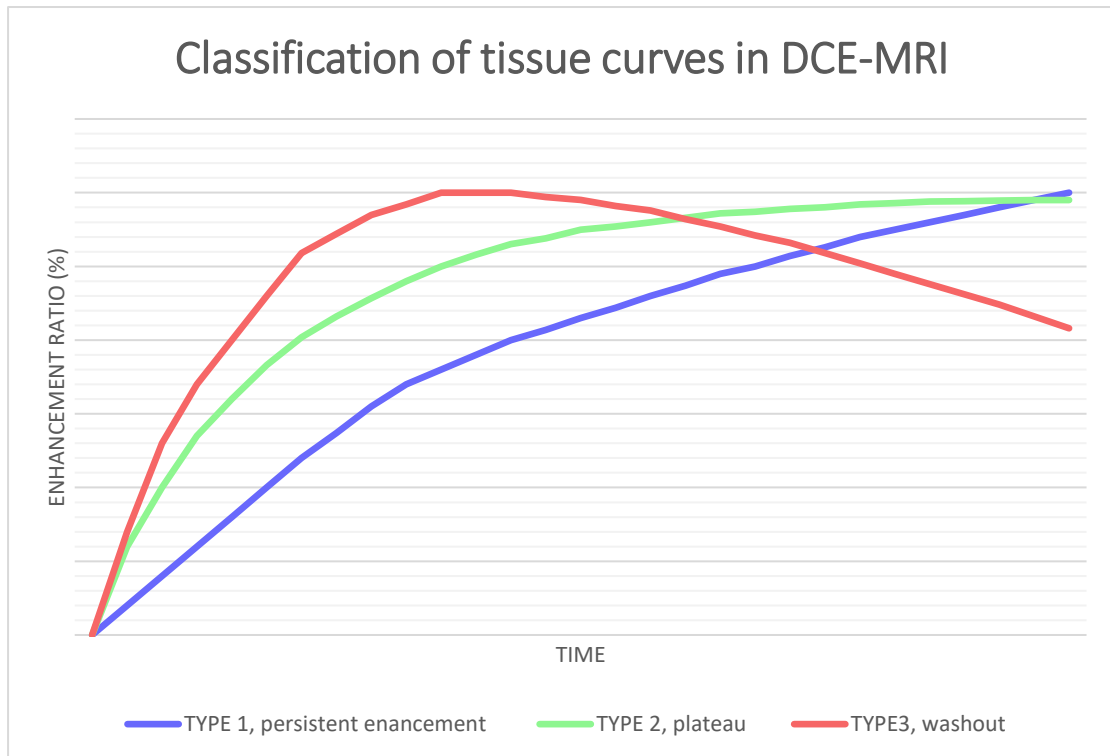


*Figure 15. Classification of tissue curves in three patterns. Type 1 is the blue curve where persistent wash-in is noticed. Type 2 is the green curve where the enhancement is followed by a plateau. Type 3 is the red curve where the initial wash-in phase is followed by a wash-out.*

In the past few years, pure tissue curve analysis has often been combined with sophisticated Pattern Recognition (PR) techniques to classify DCE-MRI data. These methods involve automatic recognition of certain enhancement patterns based on a statistical classifier, which is responsible for decision making to assign a certain pattern to a certain class (235). The most widely used unsupervised method is the principal component analysis (PCA) which finds a linear transformation that maps the time curve of the SI to a new coordinated system of uncorrelated and orthogonal axes (236). Independent component analysis (ICA) (237), which differs from PCA in the assumption that the signal is a linear combination of statistically independent non-Gaussian signals, is also commonly used. Finally, supervised methods have been widely used for this purpose, such as artificial neural networks (ANNs), and multi-layer

perceptron (MLP) (238) a sub-group of ANNs, which comprises of a set of processing nodes organized in input, hidden and output layers. Support vector machines (239) (SVM) are also popular supervised learning models, that have been used as a classification mechanism for delineating malignant and benign lesions

Concluding, model free methods for DCE-MRI for a promising analysis framework that have been gaining ground over the last years. Its main benefit is the increased robustness and the reduced sensitivity to protocol parameters and user interference.

## 6.6 Conclusion

DCE perfusion is an imaging technique that give an added value to the MRI, by adding information about the hemodynamic characteristics of the examined tissue. A lot of methods have been proposed for the analysis and interpretation of the dynamic curves, with the two major groups being the model based PK modelling and the model-free approaches using PR techniques. For the right choice and application of each method, the quality of the data and the characteristics of the examined tissue should be taken into account.

## 7 Research motivation and thesis goals

- **Optimization of DCE perfusion MRI protocol for imaging active MS and CIS lesions**

The initial goal of this dissertation, is to design a DCE perfusion protocol tailored to the needs of imaging active MS and CIS lesions, providing better spatial characterization and quantification of these lesions. Considering the limited available MR imaging time, novel solutions should be found in order to extend the acquisition time without temporal burden of the imaging time.

Furthermore, taking into account that active MS and CIS lesions are characterized by low permeabilities, the conventional imaging protocols do not provide sufficient time for the extravasation of the CA to the brain parenchyma. For this purpose, this dissertation proposes that longer scan times will imply higher tissue concentration, thus increased signal intensities and better capturing of the underlying phenomena. Thus, this dissertation proposed the extension of the DCE acquisition time, by acquiring extra-single T1 snapshots after the conventional DCE protocol that will be incorporated in the conventional protocol in a post processing step, resulting in a time extended perfusion protocol, called Snaps, by minimally extending the DCE conventional acquisition time.

- **Application of DCE perfusion MRI in lesions and NAWM areas of MS and CIS patients and correlation with neuropsychological data**

Both the conventional and the novel proposed DCE protocol will be applied in a cohort of CIS and RRMS patients and the DCE perfusion parameters of NAWM, non-

enhancing and enhancing lesions will be examined, to investigate the added value of the extended time proposed protocol in the detection and characterization of MS lesions, regarding their post-inflammatory permeability changes. Furthermore, considering the cognitive disturbances that occur in MS and CIS patients, as well as the fact that these are lacking explicit explanation by conventional MRI techniques, the investigation of the underlying microstructural damage through DCE perfusion protocol is of great interest. For this purpose, this dissertation aims to examine the role of perfusion characteristics of CIS and MS patients, derived from the application of the DCE perfusion MRI data, aiming to predict the cognitive and emotional status.

- **PK quantitative analysis for clinical research**

To our knowledge, most MR modalities do not provide embedded perfusion software, while commercial solutions result in an extra, high cost. Moreover, these solutions do not provide open source code, thus these are not subjected to modifications in the computational procedures that are required for research purposes.

For this purpose, this dissertation aims to develop an in-house software platform that will be able to analyze the below mentioned novel DCE protocol for MS and CIS patients and provide computational solutions that are tailored to the needs of analyzing MS and CIS data. This will be an integrated perfusion analysis platform, providing functionalities such as importing several medical image protocols (dicom, nifty), signal denoising techniques, PK analysis and maps visualization. Furthermore, several computational PK models are available in the literature, each of these making several different assumptions and providing accurate results under different

pathologies. This dissertation aims to examine the accuracy of the available PK models for the purpose of analyzing active MS and CIS lesions.

- **Computational analysis validation**

Considering the plethora of available PK models and the dependence of the underlying analysis under different assumptions, the validation of the computational tools is of great importance. Taking into account that there is no existing ground truth on PK analysis of MS and CIS data, the aforementioned analysis framework was tested and validated in a breast cancer patient cohort, that were classified as responders, no-responders to NAC therapy through a biopsy specimen. This part of the present dissertation achieved to accurately classify the aforementioned patients as responders or no-responders with great accuracy.

- **Correlation between DSC and DCE perfusion parameters in MS and CIS patients**

There are a few studies in the previous literature, employing DSC-MRI in MS patients, revealing diffuse hemodynamic impairment both in NAWM and in deep GM areas. Furthermore, increased perfusion had been reported in acute enhancing and in chronic reactivated non-enhancing plaques, as well as in NAWM of CIS patients, thus revealing the sensitivity of DSC technique in the detection of inflammatory activity in the acute phases of the disease. Main perfusion MRI techniques are the DCE and the DSC MRI, both able to quantify hemodynamic function of the brain but in a different context. To our knowledge, there is not any published research for correlation between the parameters from these techniques in demyelinating diseases, thus it worth to examine for undisclosed correlations.

## Part B: Disease oriented research methodology and clinical application

## 8 PK quantitative analysis for clinical research

Computer-aided diagnosis (CADx) systems are used in several medical image analysis applications for assisting clinicians in the interpretation of medical images as well as the characterization of various pathologies including MS. MRI provides tissue related measurements that combined with signal post-processing techniques are able to quantify the underlying physiological processes. To this end, a software application for the analysis of DCE-MRI data was implemented, combined with powerful visualization techniques. Model-based techniques have been implemented in order to describe the PK properties of Gd-based contrast agents and provide quantitative results to the end user under an interactive graphical user interface (GUI).

### 8.1 DCE–MRI quantification

In this first module, a DCE-MRI data analysis platform with GUI to facilitate the workflow of the method, is introduced. Moreover, the pipeline of the procedure as well as critical aspects of designing clinical studies are summarized.

For the reliable quantification of DCE data, there are several critical aspects that user must be aware. Regarding data acquisition, scanning parameters need to be carefully selected (such as repetition time (TR), echo time (TE) and flip angle (FA)) whereas the type of the tracer, the dose injected and the rate of injection are also critical. Regarding data analysis, important parameters to consider include: (a) selection of the Region of Interest (ROI) for tissue and artery by expert radiologists, (b) selection of the Arterial Input Function (AIF) region or the assumption of a theoretical one, (c) the algorithm used to estimate CA concentration from signal intensity values, (d) the PK model used for data fitting (which should optimally take into account individual differences in hematocrit levels).

### 8.1.1 Data Preparation

The data can be uploaded from a variety of medical imaging protocols (i.e. DICOM, NIFTI, ANALYZE, MAT). Once the import of the data is accomplished, a table appears in the main window with information on the imaging protocol used to acquire the data (TR, TE and FA settings; see Figure 16). In the next step, the user is able to navigate through the dynamic series either by slice or time instance. The user can also check time curves for a user-selected area, and if necessary a temporal smoothing algorithm using splines can be applied for signal denoising. If the patient moved during the acquisition of the DCE data, a registration algorithm is available which co-registers all the volumes according to the specified reference volume. Usually, the reference volume is the arterial phase, where the contrast to noise ratio is maximized. Finally, the default values for the CA  $r_1$  constant and the Hematocrit of the patient are  $4 \text{ L} \times \text{mmol}^{-1} \times \text{sec}^{-1}$  and 0.45 respectively, but these can be modified according to the user.

In order to proceed to the next step, the user is asked to manually set the onset of CA injection. This can be accomplished by considering the time course signal of an artery and complete the corresponding field as shown in Figure 16.

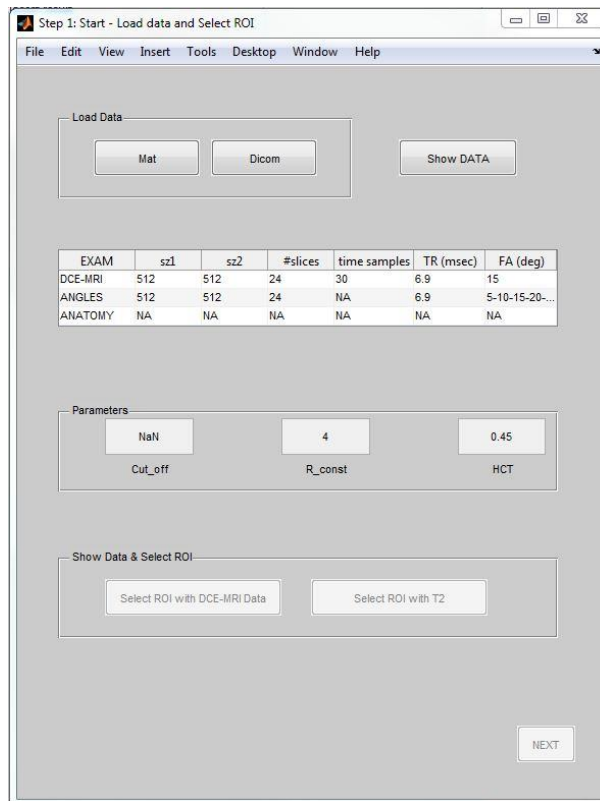


*Figure 16. Pre-processing step of the DCE tool. In this step user Load the data-set, update the CA r1 constant and Hct and select the ROIs*

In order to proceed to the analysis, user have to manually set the injection time of the CA. To this end, the “Show DATA” button from Figure 16 let the user to visually inspect the image dataset, by browsing the different slices, the different time stamps of the DCE and even check the temporal evolution of a specific voxel, as shown on Figure 17, Figure 18 Figure 19.

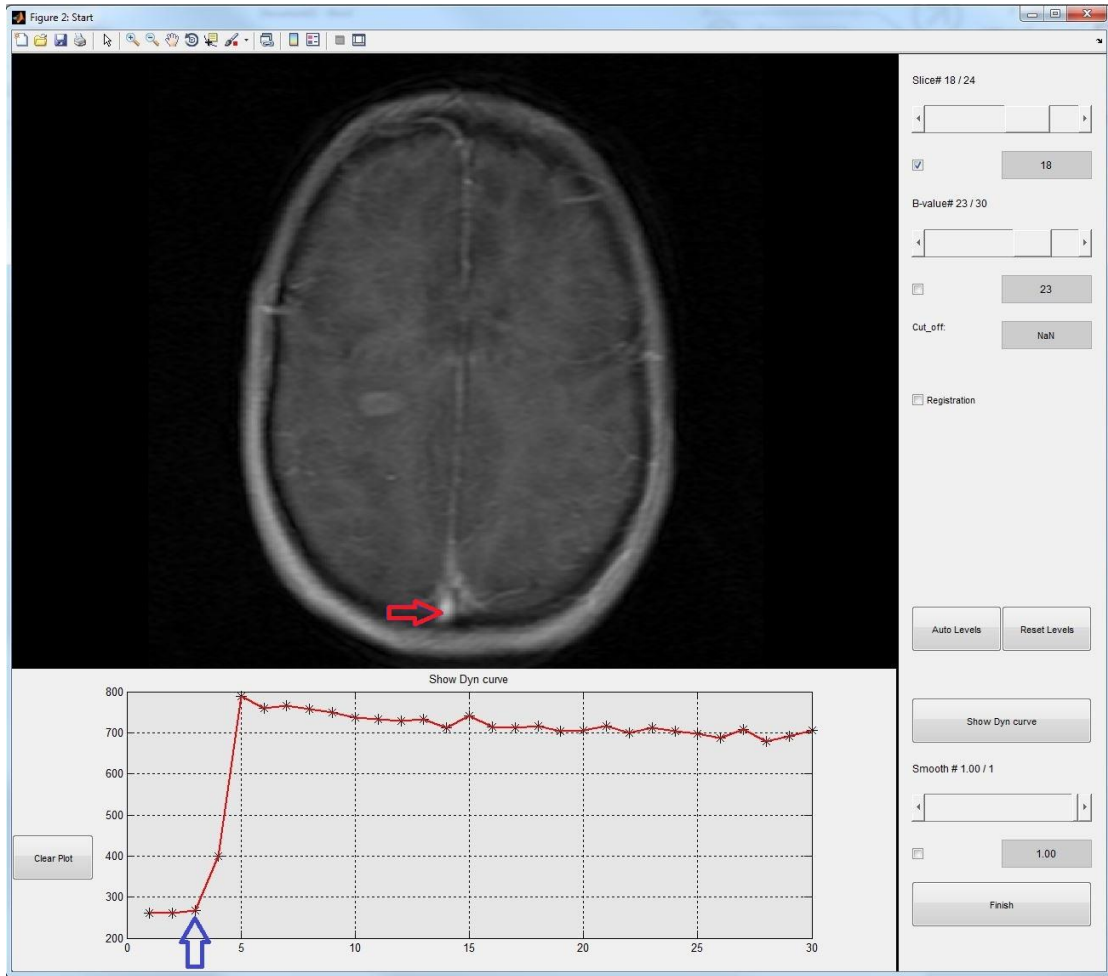


Figure 17. The upper left panel displays the image set loaded. The controls for scrolling through slices and time points and the de-noising module appear on the right-hand side (here the smoothing parameter was set at the default value of 1.00: no noise reduction was applied to the signal). The temporal evolution of the signal from a selected voxel can be depicted in the lower left-hand panel. In this example, the temporal evolution from a vein voxel (red arrow) is shown. The blue arrow indicates the onset of the CA injection. Stars indicate original measurements which in this case coincide with the denoised data (red line).

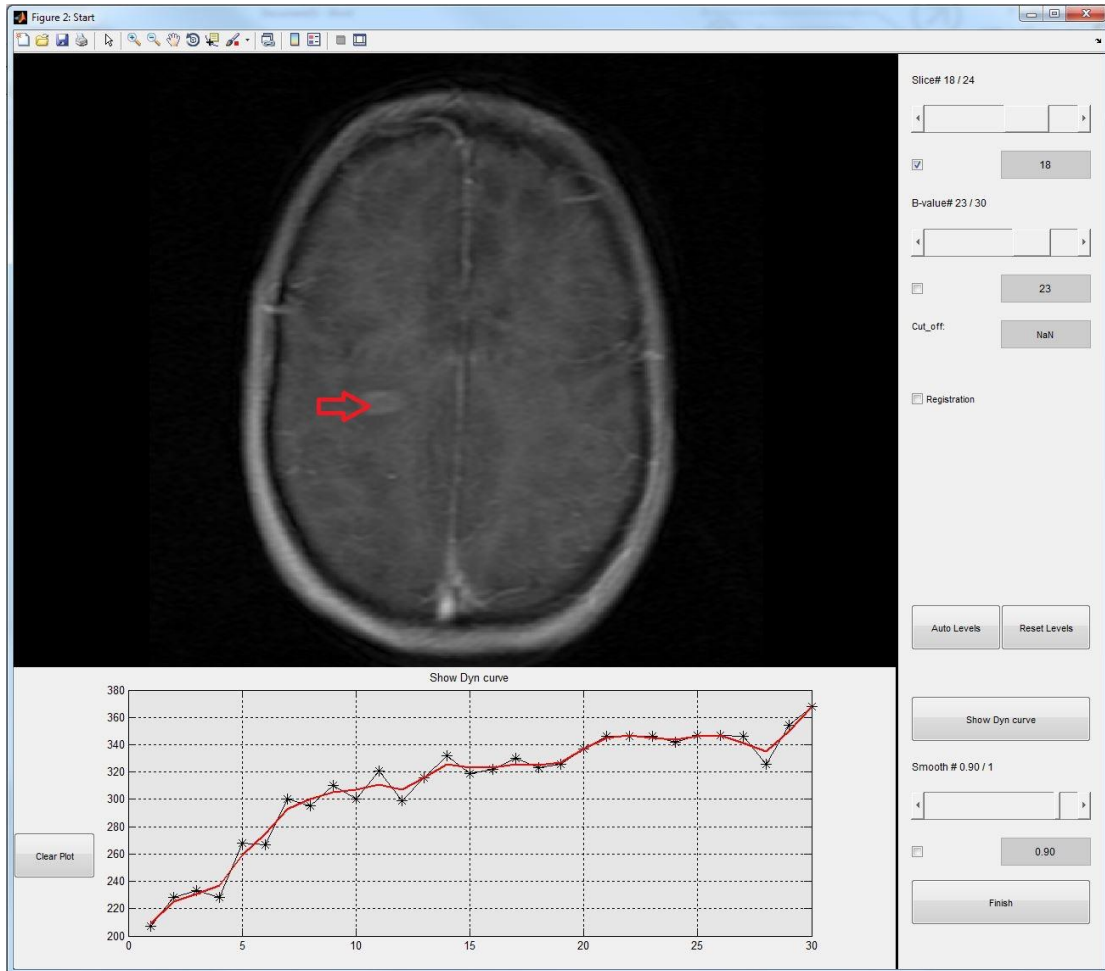
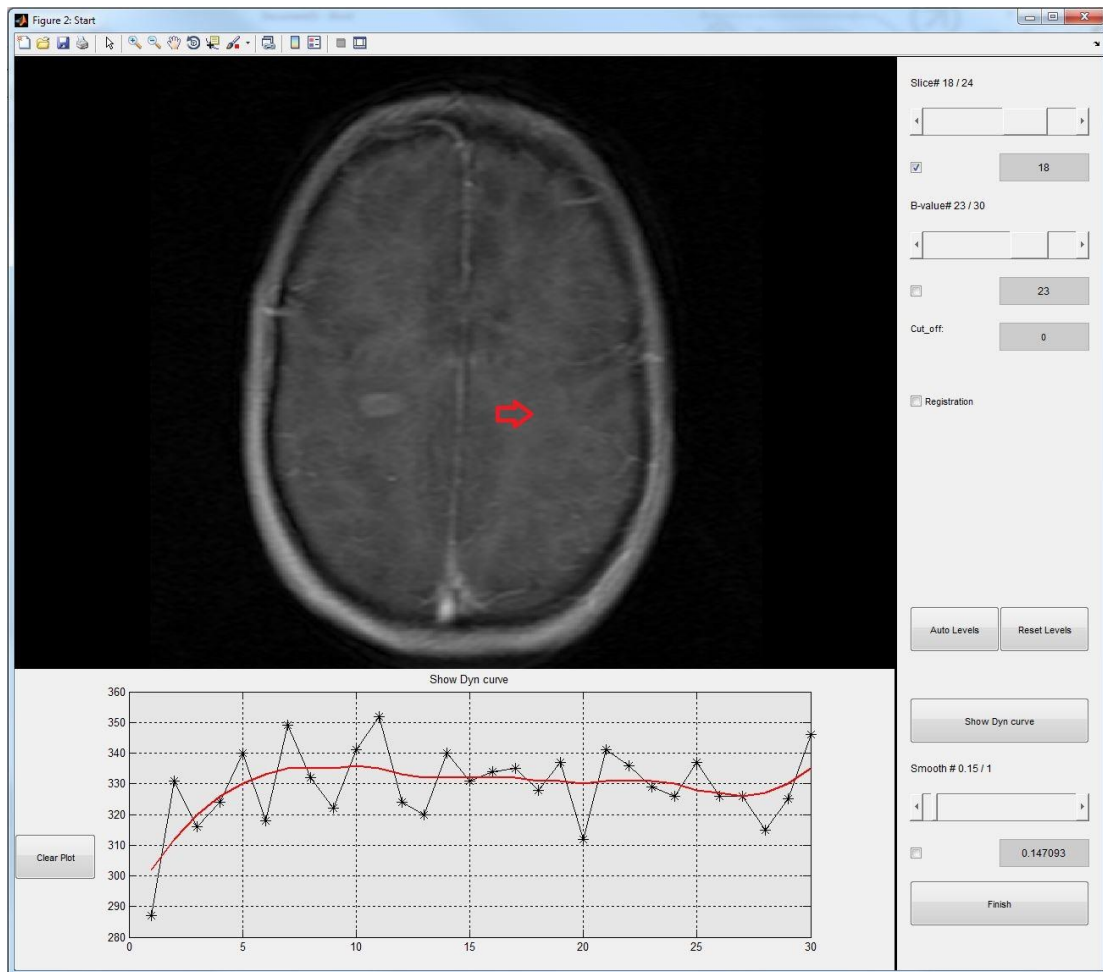
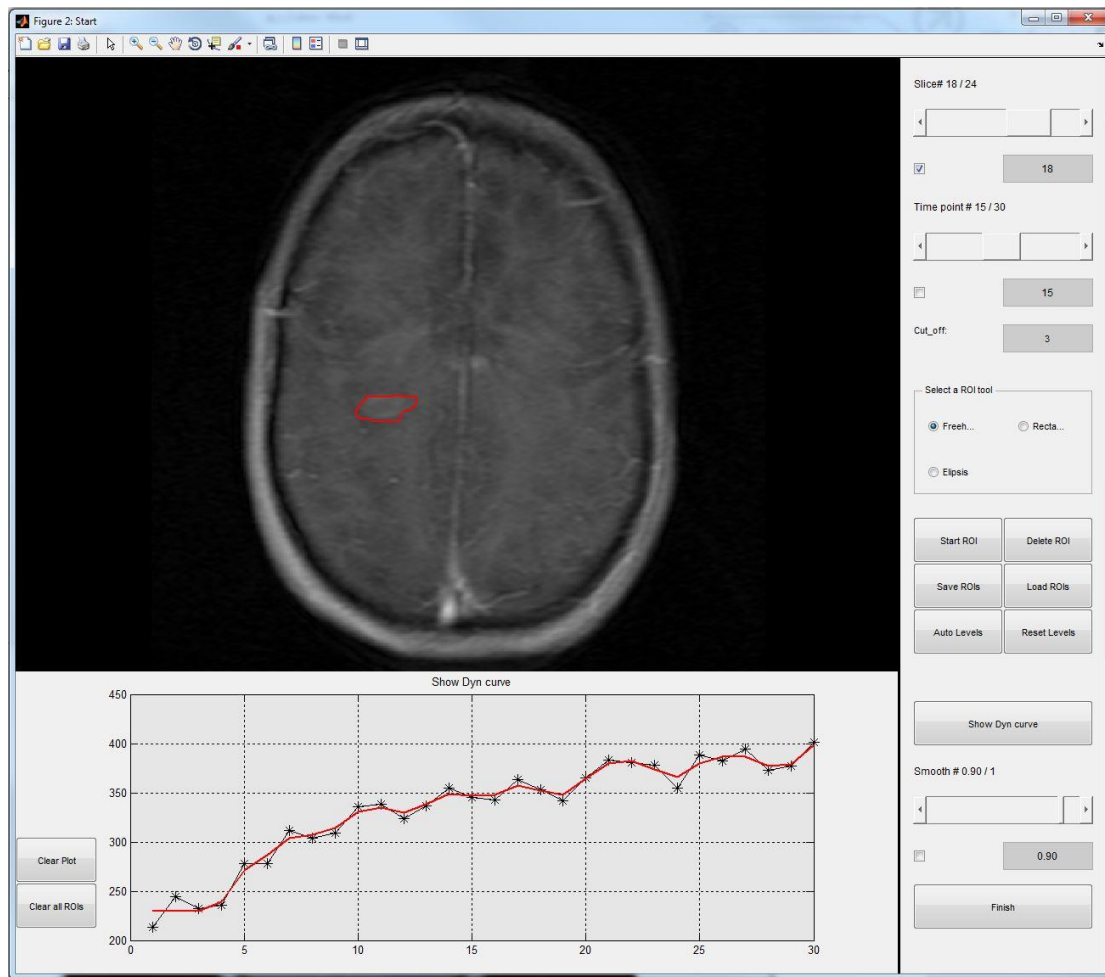


Figure 18. The signal evolution of a voxel from an active lesion (red arrow) using smoothing parameter 0.90. It is obvious that some spikes are removed from the plotted curve (stars indicate original data; denoised data are shown by a red line).



*Figure 19. The signal evolution of a voxel in normal brain parenchyma (red arrow) using smoothing parameter 0.15*

Next step is the selection of the area that should be analyzed. In this step, the user annotates from multiple slices the regions that will be fitted to the PK model using different geometric forms. Moreover, there are options to save and load ROIs, and to display the time curve of a tissue by selecting a single voxel or a 2D ROI. The User Interface (UI) of this step is shown in Figure 20. The user can scroll through the dynamic series either by slice or by time instance in order to see the temporal distribution of the CA and annotate the desirable area of interest accurately.



*Figure 20. Selection of ROI. User can also Save and Load ROIs and examine the dynamic curves of a specific tissue. In the bottom of the image it is appeared the raw SI of a pixel by black stars and the noise compensated signal by the red line.*

### 8.1.2 Signal to Contrast Conversion

An optional but crucial step of the analysis is the conversion of the SIs to CA concentration. To this end, the temporal evolution of the T1 of the tissue should be known. Alternative approaches constitute the direct fitting of the SIs to the PK model or the assumption that the ROI under examination has a constant pre-defined T1 value. However, this can lead to erroneous results due to the non-linear relationship of SI with CA concentration, especially in tissues with higher CA concentrations. These non-linearities depend on such factors as native T1 relaxation time of the examined tissue and MRI acquisition parameters. It is therefore recommended to convert both

tissue and artery SIs to CA concentration for a more robust analysis. The main techniques for measuring T1 relaxation time are the inversion recovery method (200), the Look-Locker method using an EPI protocol (201) and the multiple flip angles (mFAs) using SPGR protocols (202). In this tool, the mFAs method is used due to high Signal to Noise Ratio (SNR) and time efficiency. In this method, a T1-weighted sequence with at least two different flip angles should be acquired prior to the CA injection.

### 8.1.3 Arterial Input Function

Another critical aspect of the modeling procedure is the selection of AIF. This is a time evolving signal which describes the CA concentration in the artery that supplies the tissue of interest. The selection of AIF is critical for the PK modeling procedure and affects the reproducibility and the reliability of the results, thus in almost all PK models it has to be determined. The measurement of AIF may be impeded by a number of issues, including the partial volume effect, non-linear effects, flow artifacts, patient motion during acquisition or even the absence of an artery in the field of view of the MR image. In case that direct measurement of the AIF is not feasible, the tool provides the option to assume a theoretical one from Fritz-Hansen (240) and Weinmann (213).

The procedure for AIF selection by manually selecting a ROI is illustrated in Figure 21. Figure 22 displays the procedure to select a population average AIF.

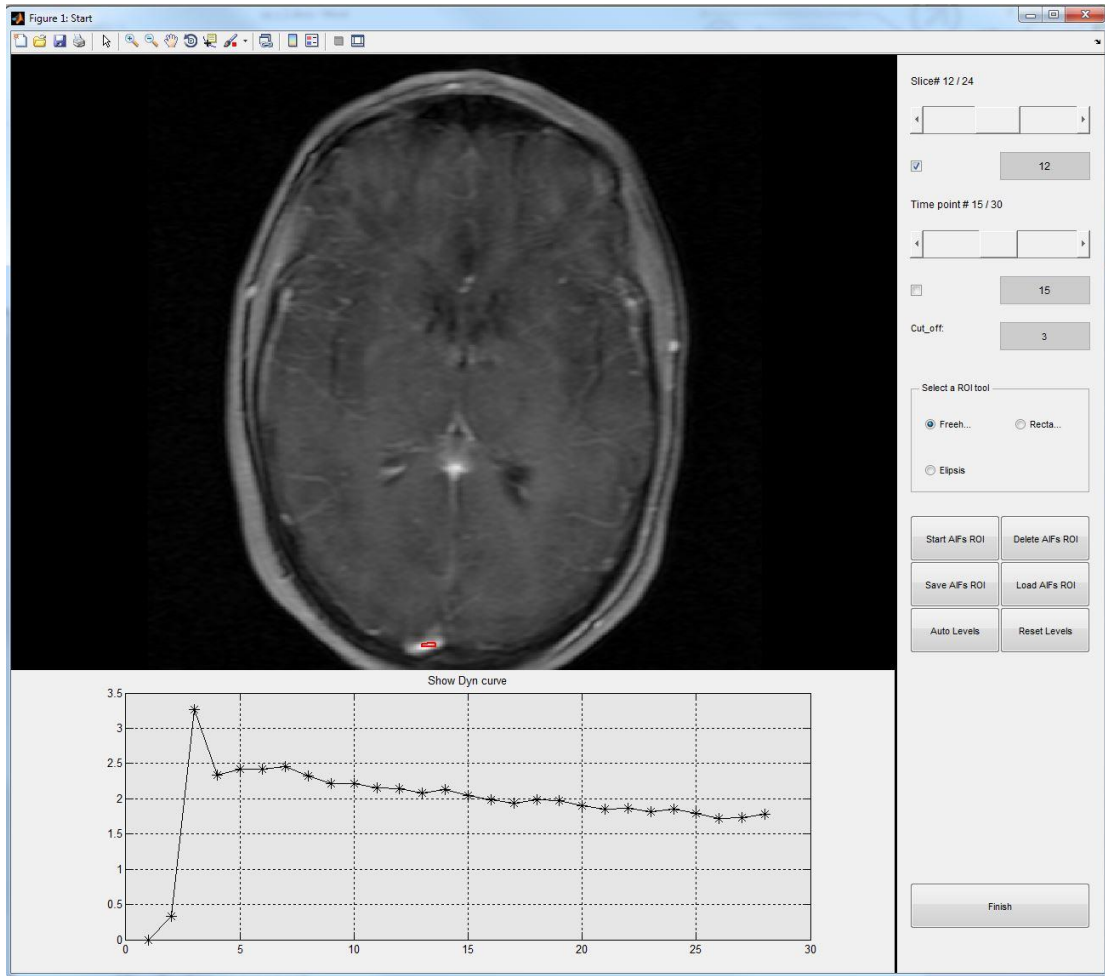


Figure 21. Selection of a vein for calculating the AIF (red selection on the MR image). In the lower left part there is depicted the resulted concentration time curve, the x axis represents the time samples while the y axis represents the CA concentration in mM.

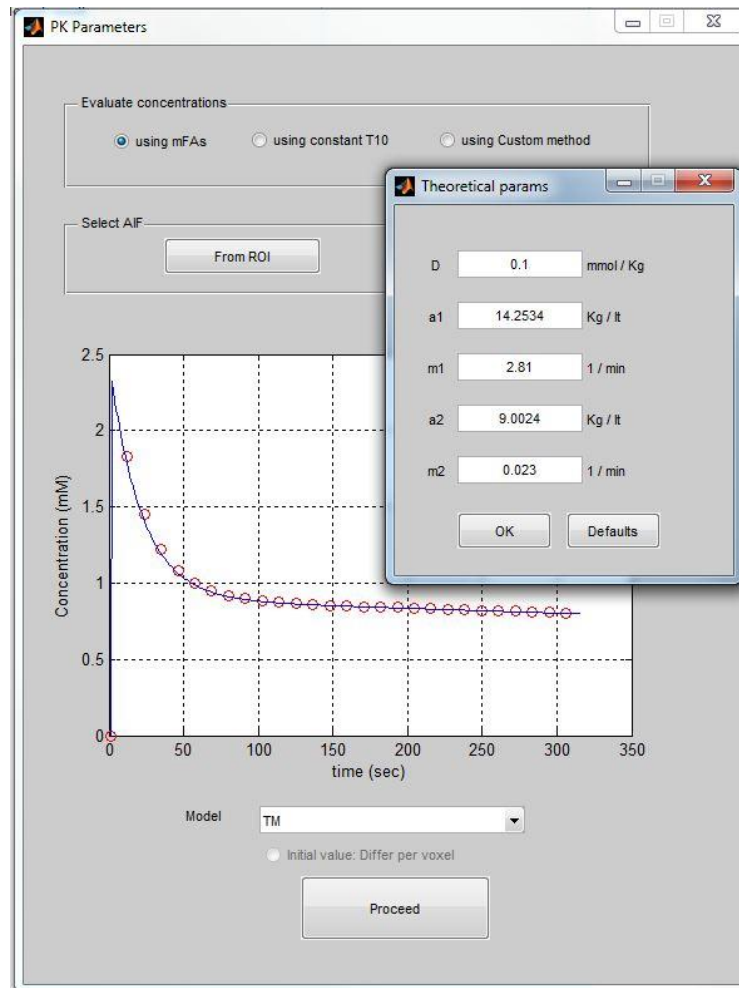


Figure 22. A population average AIF from Weinmann

#### 8.1.4 Models

Tracer kinetics can be described by two compartment models. Under this assumption, we consider two different compartments, the intravascular and the extravascular, where the tracer can be transferred among them. Parameters of interest are the transfer rates among compartments as well as the percentage space they occupy. There are a number of models that under several assumptions fit the DCE-MRI data into a set of equations, thus yielding quantitative measurements of tissue physiology. Tofts et al. published a standard set of names and symbols for these quantitative models (222) while comparative studies among these different approaches and thorough reviews can be found in the literature (9).

The models that are integrated into the tool are the well-established Tofts Model (TM) (10), the modified version that includes the vascular space Extended Tofts Model (ETM) (175), the spatially distributed Adiabatic Tissue Homogeneity Model (ATH) (225) which accounts for both spatial and temporal distribution of the CA, the Two Compartment Exchange Model (2CXM) (227) which estimates separately the permeability and blood flow and the Gamma Capillary Transit Time Model (GCTT) (230) that unifies the aforementioned models.

The UI of the DCE-MRI quantification step is shown in Figure 22 where the user is about to choose the method of signal to concentration conversion, the AIF and the model that will be used as discussed above.

## 8.2 Visualization

The visualization platform was designed to assist the visualization of the images and of the results of the processing workflow described in the previous sections. In this module the user is able to visually inspect the resulted biomarkers and assess differences between different PK models, by using a pseudo-coloring map (in the right part of each figure), as well as corresponding histograms and statistical indexes (mean, median etc.). User can also inspect the SI time curve as well as the corresponding CA concentration time curve, for a given voxel or ROI. Resulting PK biomarker values can be exported for further analyses. Moreover, in the right part of this module there are adjustments for the visualization, such as opacity, min and max of pseudo-coloring and upper and lower thresholds. Finally, the user is able to load PK analysis results from the same patient using different analysis parameters, such as different PK model, or from another patient in order to compare the results, as shown in Figure 23.

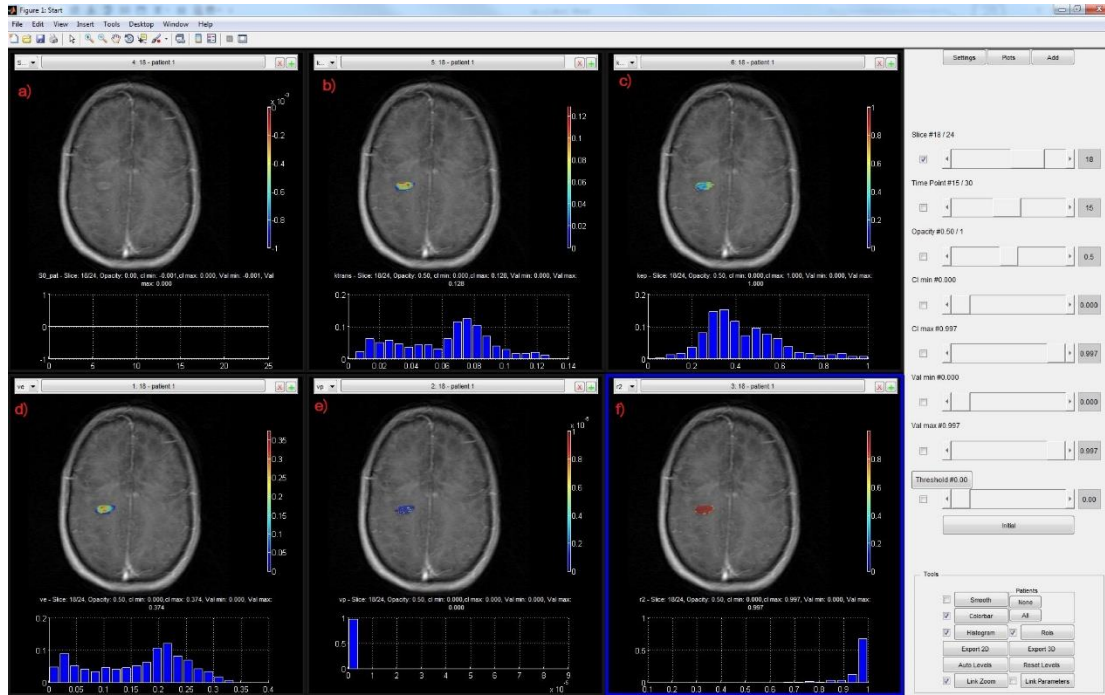


Figure 23. The visualization platform. In this module, the user can visually inspect the corresponding PK parameters, as well as the raw MRI images and the T10 map. The figure depicts a) the raw image, b) the  $k_{tr}$  map, c) the  $k_{ep}$  map, d) the  $v_e$  map, e) the  $v_p$  map and f) the  $adj-R^2$  that is a goodness of fit metric. Each image is accompanied by a pseudo-coloring scale for the corresponding parameter. The distribution of parameter values across all voxels within the prespecified ROI is shown in the histograms underneath each image.

## 9 Testing our computational tools for predicting tumor treatment response outcome

Imaging biomarkers are widely used for diagnosis, treatment response and prediction of treatment outcome in tumor tissues in a wide variety of anatomical sites, including brain and breast. Moreover, MRI is the most commonly used medical imaging technique to demonstrate tumor morphology and the relationships between malignant lesions and the neighboring structures, while it also provides relevant information for clinical management and surgical planning.

BBB is disrupted by various mechanisms in pathologies such as tumors (241) or multiple sclerosis (25), and this disruption is reflected by contrast enhancement in pathological areas. DCE-MRI is a useful imaging technique for assessing the BBB leakage, but its application in MS is rather limited in clinical practice.

Considering the wide application and the clinical confirmation of the DCE MRI biomarkers in tumor tissues, as well as the fact that in tumors there is clinical ground truth that can be confirmed, the DCE PK analysis tool presented in Chapter 7, was tested and validated on breast cancer patients that underwent neoadjuvant chemotherapy (NAC). Breast cancer is the most frequent cancer diagnosed in women worldwide (242) and is the leading cause of cancer deaths among women. Neoadjuvant chemotherapy (NAC) is considered the gold standard for locally advanced breast cancer (BRCA) treatment as it can lead to a more successful breast surgery by reducing the tumor size that needs to be excised and by possibly curing micrometastases earlier than adjuvant treatment (243).

In the present study, a public available BRCA dataset (244-246) was analyzed, comprising of DCE-MRI, DWI and PET/CT data from patients with stage II/III breast

cancer acquired before, during and at the end of NAC. Moreover, this study focus on DCE-MRI data from the above-mentioned BRCA public available dataset, aiming at a detailed investigation of several model-based IBs. To this end, in the present study the aforementioned DCE-MRI dataset was utilized in order to investigate the potential of biomarkers stemming from quantitative PK analysis techniques in predicting therapy outcome early in the NAC setting. PK analysis was conducted using extended Tofts model (ETM), an established PK model that was used for assessing perfusion characteristics of the tumor tissues. For the statistical analysis, we investigated the prognostic value of the 4 resulted model-based IBs ( $k_{trans}$ ,  $kep$ ,  $ve$ ,  $vp$ ). This work is presented in (247), examined also model-free techniques that are out of the scope of the present chapter, thus this part of the analysis will not be included in the following chapter.

## 9.1 Materials and Methods

### 9.1.1 Patient and protocol information

The complete dataset consists of 59 patients with histologically-proven breast cancer of stage II/III. DCE, DWI and PET/CT imaging data were acquired in the beginning, after the first cycle and at the completion of NAC. Furthermore, each patient was classified as pCR or non-pCR according to a biopsy specimen acquired at the end of all NAC sessions. Complete response was associated to the lack of tumor residual in both breast and lymph nodes which is in accordance with Sataloff (248).

From the complete dataset, including 59 patients, 20 patients had only PET/CT exams so these were excluded. From the remaining 39 patients, 4 patients were excluded since they had only one DCE exam, therefore the dataset that was analyzed in this study included 35 patients with two or three DCE longitudinal imaging studies.

The analyzed patient cohort included 12 pCR and 23 non-pCR patients, having a baseline and a follow-up exam whereas few of them (4 pCR and 8 non-pCR) had also a second follow-up exam.

DCE and multiple flip angles (mFAs) data were acquired on a 3.0T Philips Achieva MR scanner using a 16-channel bilateral breast coil. The acquisition of mFAs included flip angles from 2° to 20° by 2 degrees increment, whereas DCE flip angle was 20°. Imaging parameters for both DCE and mFAs protocols were TR 7.9 ms, TE 4.6 ms, 192×192×20 image resolution, 220×220 mm<sup>2</sup> field of view (FOV) and slice thickness 5mm, while in DCE temporal resolution was 16 secs and 25 dynamic acquisitions were acquired. The gadopentetate dimeglumine (Gd-DTPA) CA was administered via a power injector using 0.1 mmol/kg

#### 9.1.2 Image analysis methods

DCE-MRI data were annotated by an expert radiologist, directly on the DCE images, considering also the corresponding DWI images. This process was performed on a Graphical User Interface (GUI) platform, presented in chapter 8, written in Matlab 8.1.0.604 (R2013a) on an Intel Core 2 i7-4770 processor, 3.4 GHz with 16 GB RAM, dedicated for DCE-MRI PK modeling (249). The adopted DCE model-based analysis technique is discussed in the following sections.

Concerning the PK analysis, DCE exams were processed using our in-house platform, presented in chapter 8 (249). The mFAs data were used for SI to contrast agent (CA) concentration conversion. Considering the absence of an artery or vein in the FOV of the majority of DCE exams, a population based arterial input function (AIF) from Weinmann (213) was used for all analyses. It should be considered that assuming

the same theoretical AIF for every patient may influence the accuracy of the extracted biomarkers. That said, image-based AIF computation is also prone to errors since large vessels may be out of the FOV, may suffer from partial volume effect, or may have an inaccurate flow profile especially for image acquisition in sagittal plane.

PK analysis was based on the ETM (175), a two compartment model that estimates the interstitial to plasma rate constant  $k_{ep}$  (1/min), the volume transfer constant  $k_{trans}$  (1/min), the interstitial volume  $v_e$  ( $k_{trans}/k_{ep}$ , dimensionless) and the plasma volume  $v_p$  (dimensionless). Tofts et al. introduced the two compartment PK model that describes the CA kinetics using the following equation:

$$C_t(t) = v_p \cdot C_p(t) + k^{trans} \int [C_p(t) \cdot e^{-k_{ep}(t-\tau)}] \cdot dt \quad (21)$$

In equation (21),  $C_t$  is the CA concentration in the tissue and  $C_p$  is the CA concentration on plasma. By converting the SI in every pixel of the DCE study in CA concentration, and assuming that this is the tissue concentration, a non-linear fitting on Equation (21) estimates the vector ( $k_{trans}$ ,  $k_{ep}$ ,  $v_e$ ,  $v_p$ ). These four extracted biomarkers were then limited in ranges with biological significance i.e.  $k_{trans} < 5$  1/min,  $v_e < 1$  and  $v_p < 1$ , whereas pixels with values out of these ranges were excluded from the statistical analysis. Finally, for every resulted biomarker ( $k_{trans}$ ,  $k_{ep}$ ,  $v_e$ ,  $v_p$ ) as well as for their percentage changes, the mean, median and 5th, 15th, 80th and 90th percentiles, were computed respectively for the statistical analysis. Each variant from the model-based method, is considered as a different biomarker in our analysis (e.g.  $v_e$  80th percentile,  $v_e$  90th percentile,  $\Delta k_{ep}$  median). The mean and median values provide information about the central part of the histogram, while the 5th and

15th percentiles as well as the 80th and 90th percentiles represent the initial and final part of the histogram respectively. To this end, combining the mean and median values with the above percentiles, leads to an inclusive depiction of the histogram.

### 9.1.3 Statistical and predictive analysis

Statistical analysis was employed using R software (v.3.3) and results were displayed as mean  $\pm$  standard deviation (mean $\pm$ s.d.). A univariate analysis with the non-parametric Mann-Whitney test was applied to all calculated biomarkers to assess differences between the two subgroups (pCR vs non-pCR). For all tests, a p-value of less than 5% was considered as statistical significant.

A univariate predictive analysis framework was next conducted to further utilize all biomarkers that achieved a p-value $<$ 0.05 using 5 different classifiers. The main scope of this analysis was twofold; **a)** to estimate the discriminative power of the proposed biomarkers through a predictive analysis infrastructure using several classifiers, and **b)** assess their predictive accuracy in an unbiased way using subsets of the examined dataset that were not used for training. Initially, the examined cohort was randomly divided into stratified test and train sets comprising 20% and 80% of each examined biomarker respectively. A repeated k-fold cross validation was next performed at the training phase to prevent or reduce any over-fitting issues. K-fold cross validation was repeated 10 times with k equal to 3 due to sparsity of the training set. At the testing phase, all statistically significant biomarkers and models were validated using the “unseen” test sets. To better assess the generalization performance of the biomarkers, the aforementioned steps were repeated 50 times using exactly the same input data during each iteration and their performance was provided quantitatively using mean and standard deviation of the area under the

curve (AUC), F1 score, accuracy, sensitivity and specificity.

To examine whether a combination of the statistically significant biomarkers would potentially increase the results in terms of the predictive accuracy, a wrapper feature selection using recursive feature elimination (RFE) and the 5 suggested classifiers were applied to the examined cohort. For the convenience of the reader, ensemble adaboost with decision trees of level one, extreme gradient boosting linear, support vector machine with linear kernel, random forest, and the k-nearest neighbor were presented using acronyms clf1, clf2, clf3, clf4 and clf5, respectively. The complete workflow of the procedure is presented in Figure 24.

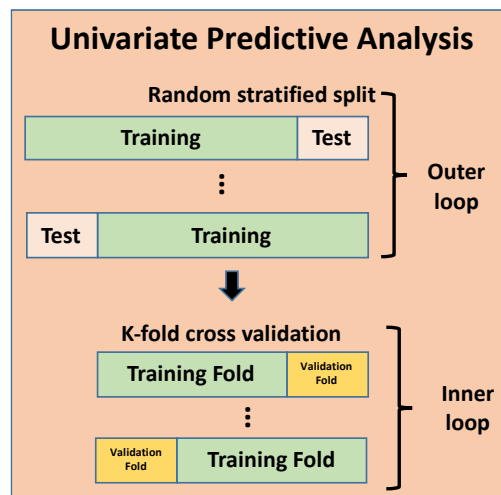
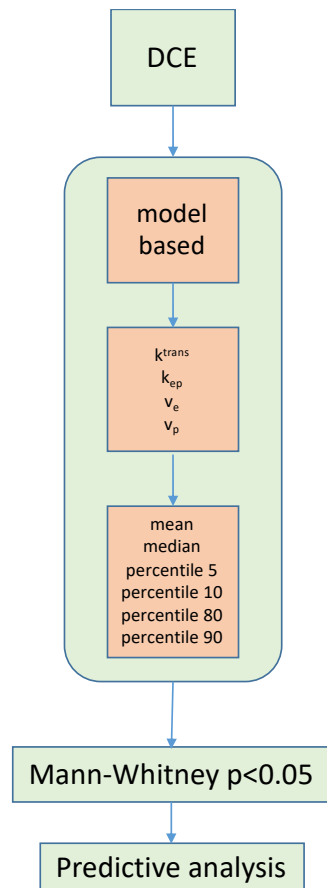


Figure 24. Analysis workflow of the proposed framework. DCE biomarkers are extracted from model-based methods and the following the statistical analysis. Afterwards, a univariate predictive analysis was applied to all the statistically significant biomarkers.

## 9.2 Results

Five biomarkers obtained at the first follow-up showed statistically significant differences between pCR and non-pCR subgroups: kep median, ve median, ve mean,

ve 80th percentile, and ve 90th percentile. The two subgroups also differed on three biomarkers measured at baseline: mean, 80th and 90th percentile of ve.

The extracted maps of the statistically significant biomarkers *kep* (first row), and *ve* (second row) are depicted in Figure 25. The first two columns are the corresponding maps of a non-pCR patient for the baseline and the first follow-up exam. The last two columns are the corresponding maps of a pCR patient for the baseline and the first follow-up exam. It can be observed from Figure 25, that the *kep* biomarker exhibits higher values on the follow-up study compared to the baseline of the non-pCR patient, whereas there is a decrease of the *kep* value for the pCR patient.

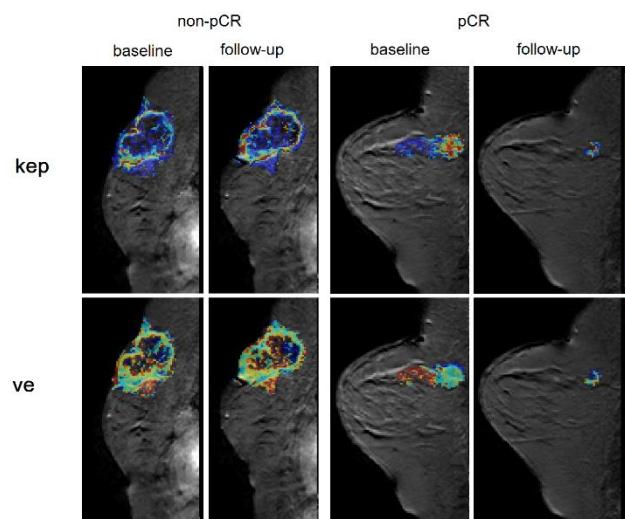


*Figure 25. The prediction significant biomarkers from a non-pCR patient and a pCR patient for the baseline (first and third columns) and follow-up studies (second and fourth columns). In the first row, the *kep* longitudinal change is shown, and in the second the *ve* longitudinal change.*

As a second step, five classifiers were utilized in order to test the predictive ability of the resulted model-based biomarkers. The best biomarkers in terms of AUC that showed non-random predictive value (sensitivity and specificity >50%) are presented in Table 7 **with bold**, together with their F1 score, sensitivity and specificity.

It is worth mentioning that no results from classifiers clf2, clf3 and clf5 for tp1 and from clf3, clf4 and clf5 for tp2 were resulted in adequate sensitivity and specificity (Table 7). For instance, for ve 80th percentile biomarker at tp1 the results (AUC, sensitivity, specificity) for clf2 were 78.5%, **37.0%**, 77.0%, for clf3 were 83.8%, **5.0%**, 96.0%, and for clf5 were 69.8%, **37.0%**, 69.0%.

It should be noted that although the best AUC for the ve 80th percentile in tp1 is achieved by clf3 (mean 83.8%), this is left out from Table 7 due to low sensitivity (5.0%). Similarly, clf2 and clf5 also result in high AUCs but low sensitivity or specificity, and are excluded Table 7. The same principle applies throughout all our statistical analysis.

*Table 7. Statistical Analysis Results*

Time Point	Classifier <sup>a</sup>	Biomarker	AUC % (mean±s.d.)	F1 % (mean±s.d.)	Sensitivity % (mean±s.d.)	Specificity % (mean±s.d.)
1	clf3	ve 80 <sup>th</sup> percentile	83.8±15.0	70.8±21.0	5.0±18.2	96.0±12.7
	clf3	ve mean	81.5±14.1	52.2±13.5	3.0±12.0	96.5±10.1
	clf3	ve 90 <sup>th</sup> percentile	81.5±15.8	61.0±13.1	9.0±24.1	94.5±14.5
	<b>clf4</b>	<b>ve 80<sup>th</sup> percentile</b>	<b>78.5±17.1</b>	<b>69.5±20.7</b>	<b>67.0±35.9</b>	<b>75.0±24.2</b>
	clf2	ve 80 <sup>th</sup> percentile	78.5±17.3	60.8±16.5	37.0±34.7	77.0±22.5
	<b>clf1</b>	<b>ve 80<sup>th</sup> percentile</b>	<b>73.4±17.4</b>	<b>62.4±17.0</b>	<b>72.0±35.2</b>	<b>59.5±29.0</b>
	clf2	ve mean	72.3±17.6	56.4±16.7	39.0±36.8	70.5±24.6
	clf4	ve mean	72.0±16.9	57.3±17.9	48.0±37.7	67.0±26.0
	<b>clf1</b>	<b>ve 90<sup>th</sup> percentile</b>	<b>70.0±14.3</b>	<b>49.6±13.1</b>	<b>52.0±39.1</b>	<b>50.0±27.7</b>
	clf5	ve 80 <sup>th</sup> percentile	69.8±14.0	55.3±12.7	37.0±36.2	69.0±26.0
	clf5	ve 90 <sup>th</sup> percentile	69.4±16.0	52.4±13.2	21.0±26.9	75.5±24.0
	<b>clf1</b>	<b>ve mean</b>	<b>68.3±16.5</b>	<b>62.0±18.9</b>	<b>76.0±35.3</b>	<b>51.5±30.1</b>
	clf5	ve mean	67.1±12.8	43.8±12.5	7.0±17.5	71.0±26.9
	clf2	ve 90 <sup>th</sup> percentile	65.5±14.0	47.9±9.1	23.0±30.7	67.5±24.9
	clf4	ve 90 <sup>th</sup> percentile	64.4±12.6	45.4±10.9	29.0±32.1	55.5±23.8
	2	clf3	ve 80 <sup>th</sup> percentile	85.0±15.6	62.3±16.6	11.0±23.2
clf3		ve mean	84.8±15.8	62.7±13.9	16.0±25.6	96.5±10.1
clf3		ve median	84.8±16.4	51.7±11.1	4.0±13.7	95.5±10.9
clf3		ve 90 <sup>th</sup> percentile	84.8±15.8	59.3±13.4	11.0±23.2	95.5±12.0
clf3		kep median	83.0±18.0	55.6±9.6	3.0±12.0	97.0±8.2
clf5		kep median	73.5±18.1	63.9±19.0	33.0±37.3	83.0±17.8
<b>clf1</b>		<b>kep median</b>	<b>73.4±18.0</b>	<b>64.5±17.1</b>	<b>68.0±36.1</b>	<b>68.5±23.6</b>
clf4		ve 80 <sup>th</sup> percentile	73.4±15.6	62.5±14.5	28.0±33.7	84.0±18.0
clf5		ve 90 <sup>th</sup> percentile	72.6±15.6	57.1±12.5	42.0±34.0	78.0±22.9
<b>clf2</b>		<b>ve median</b>	<b>72.6±20.2</b>	<b>71.0±19.4</b>	<b>67.0±31.3</b>	<b>84.0±18.7</b>
clf4		kep median	72.3±19.1	54.9±17.0	44.0±35.9	69.0±25.0
clf5		ve 80 <sup>th</sup> percentile	72.1±15.5	62.2±12.3	34.0±31.0	90.0±15.2
clf5		ve median	72.0±18.1	67.6±17.8	45.0±33.9	86.5±25.4
clf4		ve median	71.8±20.3	60.3±17.0	39.0±33.9	78.0±21.8
clf4		ve 90 <sup>th</sup> percentile	70.9±17.1	56.8±18.4	40.0±33.5	73.5±23.9
clf2		ve 90 <sup>th</sup> percentile	70.3±16.8	54.3±15.9	42.0±32.5	69.0±20.6
clf5		ve mean	70.1±17.9	65.1±20.1	33.0±34.4	88.0±17.7
clf2		ve 80 <sup>th</sup> percentile	70.0±17.7	61.0±11.6	31.0±33.3	80.5±18.4
<b>clf1</b>		<b>ve mean</b>	<b>69.9±19.6</b>	<b>62.1±16.3</b>	<b>63.0±28.2</b>	<b>73.0±25.7</b>

clf2	$v_e$ mean	69.6±20.0	65.4±17.6	61.0±27.3	83.0±19.8
clf1	$v_e$ 80 <sup>th</sup> percentile	69.4±17.8	65.0±16.5	56.0±34.5	79.5±20.0
clf1	$v_e$ median	68.4±20.3	68.5±19.5	68.0±29.9	80.0±21.4
clf1	$v_e$ 90 <sup>th</sup> percentile	67.8±16.5	57.5±19.1	58.0±32.5	66.0±24.6
clf2	$k_{ep}$ median	67.3±17.3	61.3±18.0	50.0±39.1	73.5±21.7
clf4	$v_e$ mean	66.9±19.9	56.8±14.9	39.0±30.8	77.5±18.4

<sup>a</sup>clf1 stands for ensemble adaboost with decision trees of level one, clf2 for extreme gradient boosting linear, clf3 for support vector machine with linear kernel, clf4 for random forest, and clf5 for the k-nearest neighbor classifiers.

It is worth mentioning that the  $k_{ep}$  median parameter, measured at the first follow up, was found to be the best pCR predictor, according to Table 7, in two different classifiers showing consistent accuracy results. The ensemble adaboost with decision trees of level one classifier gave the best results for  $k_{ep}$  component, with AUC 73.4%, F1 64.5%, sensitivity 68.0% and specificity 68.5%. The  $k_{ep}$  component showed also high predictive ability with extreme gradient boosting linear classifier, which further confirms the robustness of this biomarker in predicting treatment outcome. Finally, median value of  $v_e$  PK biomarker showed good predictive performance on the first follow-up using extreme gradient boosting linear and ensemble adaboost with decision trees of level one classifiers.

For baseline prediction, the mean value and 80th, 90th percentiles of  $v_e$  biomarker showed high predictive performance. Specifically, the 80th percentile of  $v_e$  biomarker showed the highest AUC of 78.5% with the random forests classifier and 73.4% AUC with the ensemble adaboost with decision trees of level one classifier. For the multivariate analysis no combination of the biomarkers resulted in better prediction outcome in baseline and follow-up study with respect to the univariate analysis. The best result from multivariate analysis, was obtained by combining recursively all statistically significant classifiers except mean and 80th percentile of  $v_e$  at first follow-up, using the extreme gradient boosting linear classifier (AUC 77.8%).

### 9.3 Discussion

In the present study, DCE-MRI data from a public available dataset, consisting of 35 BRCA patients undergoing NAC, were analyzed in order to validate the in-house T1 perfusion analysis platform presented on chapter 8. Quantitative parameters were obtained from ETM pharmacokinetic analysis, while results indicate that PK biomarkers can discriminate responders from non-responders after the first cycle of NAC. In particular, PK quantitative maps were able to discriminate responders from non-responders with good accuracy, both at baseline and first cycle after NAC therapy.

Baseline prediction of NAC treatment outcome revealed that  $v_e$  (mean, 80th and 90th percentiles) biomarker provided adequate predictive power, while at the first follow up the statistically significant biomarkers were the  $k_{ep}$  median, the  $v_e$  median, the  $v_e$  mean, the  $v_e$  80th percentile and the  $v_e$  90th percentile. Moreover, the metric with the best predictive ability, in terms of AUC and showing sensitivity and specificity more than 50%, after the first follow-up exam was  $k_{ep}$  median (AUC 73.4%), while in the baseline the strongest predictor was the 80th percentile of  $v_e$  (AUC 78.5%).

Considering that ground truth in MS and CIS patients is not straightforward, this study is a complementary task of the present dissertation that is investigating the validity of the in-house computational PK framework that will be afterwards applied in the dissertation cohort. The cohort of patients examined in the present chapter, was classified as responders and non-responders to NAC therapy by analyzing biopsy specimens, while the aforementioned PK biomarkers were able to discriminate the patient cohort with adequate accuracy, providing a strong indication about the reliability of the tool and the method that will be used afterwards.

The limitations of this study, such as limited temporal resolution, are mostly inherent to the selected dataset and have been pointed out in previous studies (245, 250). First, the cohort was of relatively small size (35) and the pCR group was smaller compared to the non-pCR group (12 pCR vs 23 non-pCR). Furthermore, results were obtained from patients with possible differences in the histological grading, while there was diversity in the specific therapeutic regimens followed for each patient. Finally, the DCE dataset used in this study was analyzed by a population AIF which may affect the PK resulted biomarkers considering that these methods don't take into account the patient-specific hemodynamic profile and tumor position.

#### 9.4 Conclusion

In this work, a publicly available DCE-MRI dataset was analyzed through model-free and model-based approaches. Overall, 35 BRCA patients with longitudinal MRI exams prior to the start and in-between NAC therapy were investigated, with an ultimate goal to predict therapy outcome as early as possible. Model-based analysis sufficiently discriminated responders from non-responders early in the therapy protocol (5 biomarkers), while in baseline prediction 3 biomarkers were found to discriminate responders from non-responders. Recently, there is a lot of research concerning the permeability of NAWM, non-enhancing lesions, and enhancing lesions in MS and CIS patients. The present tool, as presented and validated in this chapter, with appropriate analysis modifications adjusted to the specific hemodynamics of brain parenchyma, could be applied in these patients for the optimal quantification of the permeability changes in the demyelinating tissue.

## 10 Extended-time perfusion protocol (SNAPS) and assessment of permeability in MS lesions

In this chapter, a novel DCE-MRI framework is presented, comprising a newly introduced protocol, as well as a method for the selection of a suitable PK model for the accurate quantification and detection of even subtle disruption of BBB in MS lesions, with minimally extending the conventional DCE acquisition time. This study follows a preliminary study that included a small dataset of 4 RRMS patients (247). In the current study, a larger group of patients was examined, and the data analysis was more specific in terms of considering each enhancing lesion separately.

### 10.1 Materials and Methods

#### 10.1.1 Patient information and Imaging protocol

Data for this study were obtained from a subsample of 12 RR-MS patients (8 females) with active disease, as indicated by the existence of contrast-enhanced focal demyelinating lesions. The mean age at disease onset was 30.3 years, mean age at diagnosis 30.8 years old and mean disease duration was 3.7 years (Table 8). This subgroup was selected from a cohort of 56 consecutive MS and CIS patients (42 females) with mean age  $35.9 \pm 10$  years. The hospital review board approved the study and the procedure was thoroughly explained to all patients who signed the informed consent.

*Table 8. Patient and protocol information*

<i>Pt number</i>	<i>sex</i>	<i>age</i>	<i># active lesions</i>	<i># pixels/ lesion</i>	<i># Snaps acquired</i>	<i>DCE Acquisition time /window of perfusion observation (mins:secs)</i>

						NoSnaps	Snaps
1	f	33	2	173,356	8	6:00 /6:00	7:30 /26:00
2	f	24	10	164,1939,201,100,247,258,1239,365,1 46,277	6	6:00 /6:00	7:08 / 23:00
3	f	16	2	252,2651	9	6:00 /6:00	7:43 /27:00
4	f	32	1	375	6	6:00 /6:00	7:08 / 24:00
5	f	25	1	1561	7	6:00 /6:00	7:19/ 25:00
6	m	55	2	414,1072	6	6:00 /6:00	7:08 / 23:00
7	f	34	1	2991	8	6:00 /6:00	7:30/26: 00
8	f	29	1	1386	8	6:00 /6:00	7:30 /30:00
9	m	22	1	215	8	6:00 /6:00	7:30/28: 00
10	m	28	1	58	7	6:00 /6:00	7:19/ 28:00
11	m	45	1	838	7	6:00 / 6:00	7:19/26: 00
12	f	43	1	336	6	6:00 /6:00	7:08 / 23:00

All exams were performed on a 1.5T MR scanner (Hybrid Vision/Sonata, Siemens/Erlangen, Germany). For the DCE-MRI exam, a single dose (0.1 mmol/kg of body weight) of gadopentetate dimeglumine (Gd-DTPA) was administered. Prior to Gd administration, Gd-dependent sequences, such as 3D T1 - MPRAGE, were acquired. For the accurate conversion of SI to CA concentration, a fast 3D VIBE sequence implemented six times, each time utilizing sequences using a different Flip Angle (FA)

(5°, 10°, 15°, 20°, 25° and 30°) was acquired (mFAs). These six image sets of different flip angles, served as the base images for a post-processing calculation of a 3D T1 parametric image map (T10 map). Consequently, a conventional T1w DCE-MRI perfusion protocol was implemented by utilizing a fast 3D VIBE sequence, with repetition time (TR=7 msec) and echo time (TE=3.23 msec), while six baseline images acquired before the injection of CA. The FA for the perfusion protocol was 15° (T1w contrast). A reconstructed matrix size of 512 × 512 pixels was utilized, and 24 slices of 4 mm slice thickness. The DCE sequence acquired 30 dynamic time points (repetitions) with 11.3 sec temporal resolution.

After the conventional DCE perfusion protocol, hereafter referred to as NoSnaps protocol, T2-w, TSE, FLAIR, GRE, DWI and 3D T1-MPRAGE sequences were obtained. In between these post perfusion sequences, single T1-w 3D VIBE (FA=15°) delayed acquisitions were acquired, using the same parameters as the perfusion protocol and lasting 11.3 secs each. These delayed 3D T1w VIBE sequences were incorporated in the conventional DCE protocol, while the intermediate intervals were computed by splines interpolation, and the resulted image set defined the new extended DCE protocol, hereinafter named Snaps. Delayed DCE acquisitions, mFAs, and conventional DCE perfusion were all acquired with the aforementioned fast 3D VIBE sequence, using TR 7 msec and TE 3.23 msec, 512 × 512 matrix size, 4 mm slice thickness and 24 slices.

In Figure 26 a typical MRI protocol workflow for a patient is presented, including MR sequences prior and after CA administration. An exemplary SI time curve of an enhanced pixel is shown in the right part of the figure. The stars in the time curve

correspond to the time samples and the first 30 asterisks represent the NoSnaps acquisitions while the 6 last asterisks stem from the delayed T1w acquisitions. By interpolating the delayed acquisitions with a splines algorithm in order to comply with the DCE sampling time (11.3 secs), the complete Snaps protocol is obtained, depicted by the red fitted curve for an exemplary pixel inside the lesion ROI.

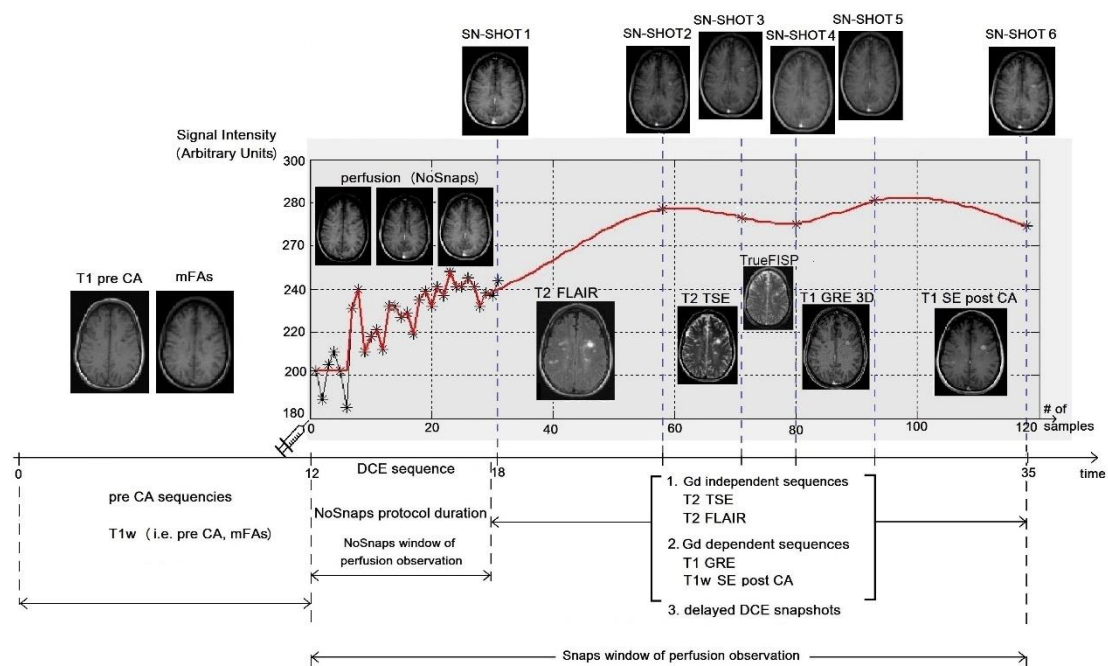


Figure 26. The time workflow of the MR protocol for patient number 2. Initially Gd dependent sequences are acquired i.e. mFAs sequence. DCE study starts at the 12th minute and lasts about 6 mins, the so called NoSnaps protocol. Afterwards, the Gd dependent sequences i.e. T1w SE post CA and Gd independent i.e. T2, FLAIR and DWI are acquired, and in between them six delayed DCE snapshots. In the right part of the figure, an exemplary SI time curve is shown in which the first 30 stars are from the NoSnaps protocol, while the next 6 stars are the delayed DCE snapshots.

The mean acquisition time for the Snaps protocol is computed by calculating the mean number of Snaps acquisitions, multiplied by their duration of 11.3secs, and the result is added to the NoSnaps acquisition time, i.e. 6mins ((mean#ofSnaps)\*11.3sec+6min). Overall, the acquisition time and the window time of perfusion observation for the NoSnaps protocol is 6 mins for all patients, whereas the mean

acquisition time for the Snaps protocol is 7 mins and 21 secs, and the mean window time of perfusion observation after the interpolation is almost 26 mins on average (Table 8). It is worth noticing the difference in time duration between the NoSnaps and Snaps protocols in the signal plot of Figure 26, where the window time of perfusion observation for the former protocol is 6 mins and for the latter protocol is 23 mins, by extending the MRI examination time in the Snaps protocol only by 1 min, approximately.

An initial 3D volume of the DCE with high contrast to noise ratio (CNR) was used as a reference for the co-registration of the DCE dynamic series and the delayed DCE snapshots using the FSL software (251, 252). Regions of interest (ROI) were annotated by a neuroradiologist (EP) with 20 years of experience directly on the DCE sequence by consulting anatomical images, such as T1 post GD and T2 FLAIR, including the part of the MS lesion with visible enhancement. Furthermore, ROIs were drawn including tissue outside the periphery of the enhancing part of the MS lesion, in order to compare the findings of the PK results in the active lesion area with the surrounding tissue.

#### 10.1.2 PK models

All the examined lesions were analyzed using three different PK models, the well-established TM (10), the extended TM (175) which considers the vascular contribution and the Patlak model (174) which, according to previous findings, provides accurate results on small BBB leakage. For all these models the mFAs data, single T1-w acquisitions with different flip angles, were used in order to accurately convert SIs into CA concentration. A population averaged arterial input function (AIF) from Weinmann et al. was used for analyzing the exams (213). Finally estimated

biomarkers were limited in physiological interpretable values  $k^{\text{trans}} < 5 \text{ 1/min}$ ,  $v_e < 1$ ,  $v_p < 1$ .

### 10.1.3 Statistical Analysis

R-square ( $R^2$ ) is a commonly used goodness-of-fit metric for a model. It has been shown that metrics which rely on the absolute distance between the fitted curve and measured data are not optimal for these problems (253). This issue is more serious when comparing models that vary on sample size and parameter number, favoring the more complex ones. Thus, in the present study, the bias corrected adjusted R-square ( $\text{adj-}R^2$ ) (254) was used instead of  $R^2$ , which takes into account differences in the number of time points between the NoSnaps and Snaps protocols, as well as differences in the number of estimated biomarkers across the three different PK models. The regression model was penalized for extra parameters that do not significantly contribute toward explaining variance in the dependent variable according to the following equation:

$$\text{adj-}R^2 = 1 - (1 - R^2) \cdot (n - 1) / (n - k - 1) \quad (22)$$

where  $n$  is sample size and  $k$  is number of predictors.

A statistical analysis was conducted in order to compare each combination of PK model and acquisition protocol (i.e. ETM-Snaps, TM-NoSnaps, etc.) using an iterative process featuring the following steps: a) all PK models were first grouped into group A (Snaps) and B (NoSnaps) according to the protocol that was used for data acquisition, b) an  $\text{adj-}R^2$  threshold was applied varying from 0.1 to 0.5 regardless of model in each set of superthreshold pixels, in order to identify regions with subtle uptake that satisfied the following thresholding equation:

(adj-R<sup>2</sup>\_ETM-protocol) OR (adj-R<sup>2</sup>\_TM-protocol) OR (adj-R<sup>2</sup>\_PATLAK-protocol) > threshold (23)

c) subthreshold pixels in each of the 3 PK models were excluded from the analysis, d) descriptive statistics for the distribution of superthreshold pixels were computed (mean, median and percentile values) for every biomarker and e) the goodness-of-fit was examined from the computed adj-R<sup>2</sup> values by comparing both PK models and protocols.

The computed parameters at each adj-R<sup>2</sup> threshold did not follow normal distributions ( $p < 5\%$ ). Accordingly, the Wilcoxon-Mann-Whitney test was used in order to evaluate differences between the two different perfusion protocols for each model on each estimated parameter (e.g.,  $k^{\text{trans}}_{\text{TM\_Snaps}}$  vs.  $k^{\text{trans}}_{\text{TM\_NoSnaps}}$ ). It should be reported, that this analysis considered only  $k^{\text{trans}}$  values, considering that this is the only common biomarker of the three examined models.

Finally, in order to examine the specific properties of each protocol separately and investigate their physiological interpretation we evaluated parameter values extracted from pixels identified exclusively by each of the two protocols (NoSnaps, Snaps).

## 10.2 Results

The range of  $k^{\text{trans}}$  values for TM and ET models were largely overlapping between Snaps and Nosnaps protocols. Conversely, the Patlak model produced overall lower  $k^{\text{trans}}$  values in the Snaps as compared to the NoSnaps protocols (Figure 27). Furthermore, when stricter thresholding was applied higher  $k^{\text{trans}}$  value ranges were achieved. This can be attributed to the fact that low enhancement pixels are

associated with low fitting accuracy, due to the low signal to noise ratio (SNR), so these are excluded at higher thresholds. Moreover, a systematic decrease of the  $k^{\text{trans}}$  values from the NoSnaps protocol to the Snaps protocol can be observed for every threshold, and the distribution of  $k^{\text{trans}}$  boxplots on the Snaps protocol are skewed towards the higher  $k^{\text{trans}}$  values compared with the NoSnaps protocol (Figure 27).

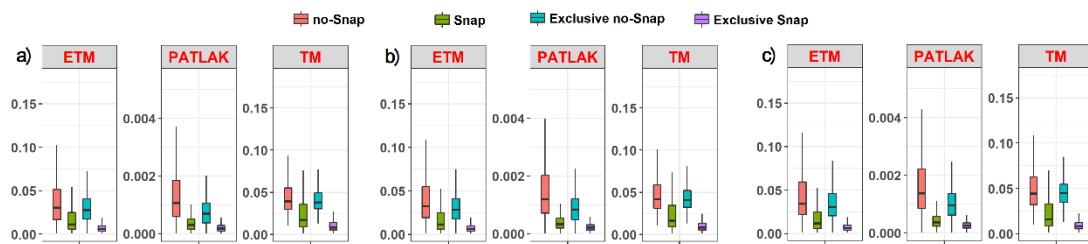


Figure 27.  $k^{\text{trans}}$  (1/min) boxplots for different adj-R2 thresholds: a) 0.2, b) 0.3 and c) 0.4, for the NoSnap (red) and Snap (green) protocols across the three model fitting methods. Values for pixels exclusively identified in the NoSnaps and values for pixels exclusively identified by Snaps are shown in blue and purple, respectively.

Subsequently, the number of remaining pixels after each consecutive thresholding, that satisfied equation (23), were calculated for each protocol. At every threshold the Snaps protocol resulted in a significantly higher number of pixels that satisfy the thresholding condition as well as in the number of exclusively identified pixels (Table 9) as compared to the NoSnaps protocol.

Table 9. Pixel contribution for every protocol after thresholding

adj-R <sup>2</sup> threshold	Total number of Pixels "NoSnaps"	Pixels identified exclusively from "NoSnaps"	Total number of Pixels "Snaps"	Pixels identified exclusively from "Snaps"	Percentage difference on Total pixels of Snaps compared to NoSnaps (%)
0.1	11544	644	15610	4710	35
0.2	9611	822	14221	5432	48
0.3	8150	962	12547	5359	54
0.4	6912	978	11062	5128	60

Concerning the goodness of fit values associated with each protocol, the Snaps protocol was associated with higher fitting accuracies across models and thresholds (Figure 28). Moreover, it is apparent that the ETM model performs better in terms of fitting accuracy compared with the Tofts and Patlak PK models (Figure 28).

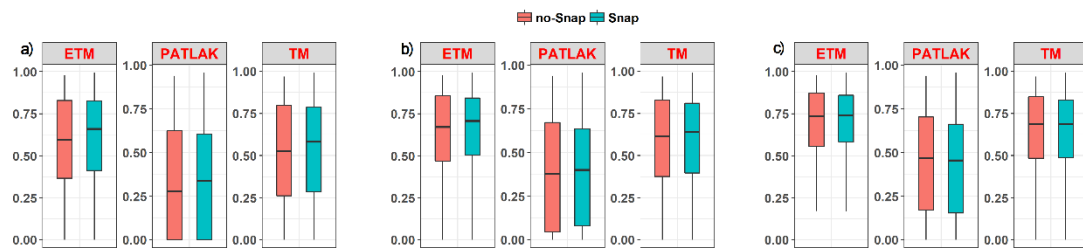


Figure 28. *adj-R2* boxplots for different *adj-R2* thresholds: a) 0.2, b) 0.3 and c) 0.4 for the NoSnap (red), Snap (green) protocols across the three model fitting methods.

Finally, it can be noticed in the SI time curve in the right part of Figure 26, that the signal from the conventional NoSnaps protocol starts from baseline intensity 200 and at the end of the protocol (30 time samples) the enhanced SI is almost 240, an increment of 20%. Examining the SI of the time extended Snaps protocol, this also starts at baseline value of 200 and after 120 samples ends up to almost 280, which is an increment of 40%. It is obvious that for signals stemming from tissue with subtle BBB disruptions, thus low CA uptake, the time extended SI of the Snaps protocol results in a better SNR thus a better fitting accuracy by a PK model.

A similar procedure was applied to pixels identified exclusively by the NoSnaps and Snaps protocols. Visual inspection the  $k^{\text{trans}}$  boxplots reveals that pixels identified solely by the Snaps protocol are represented in the lowest range of  $k^{\text{trans}}$  values. On the contrary, pixels exclusively identified by the NoSnaps protocol display a wide range of  $k^{\text{trans}}$  values Figure 27.

An additional analysis in order to validate the ROI areas was performed, by assessing the ETM goodness of fit ( $\text{adj-R}^2$ ) in the lesions ROIs (foreground) as well as in ROIs annotated in the peripheral tissue (background). To this end, the initial lesions ROIs were dilated using an octagon kernel of size 15. Afterwards, the lesion ROIs were removed from the dilated ROIs resulting in the peripheral ROIs, which were used in order to run a supplementary analysis, an exemplary result presented in Figure 29.

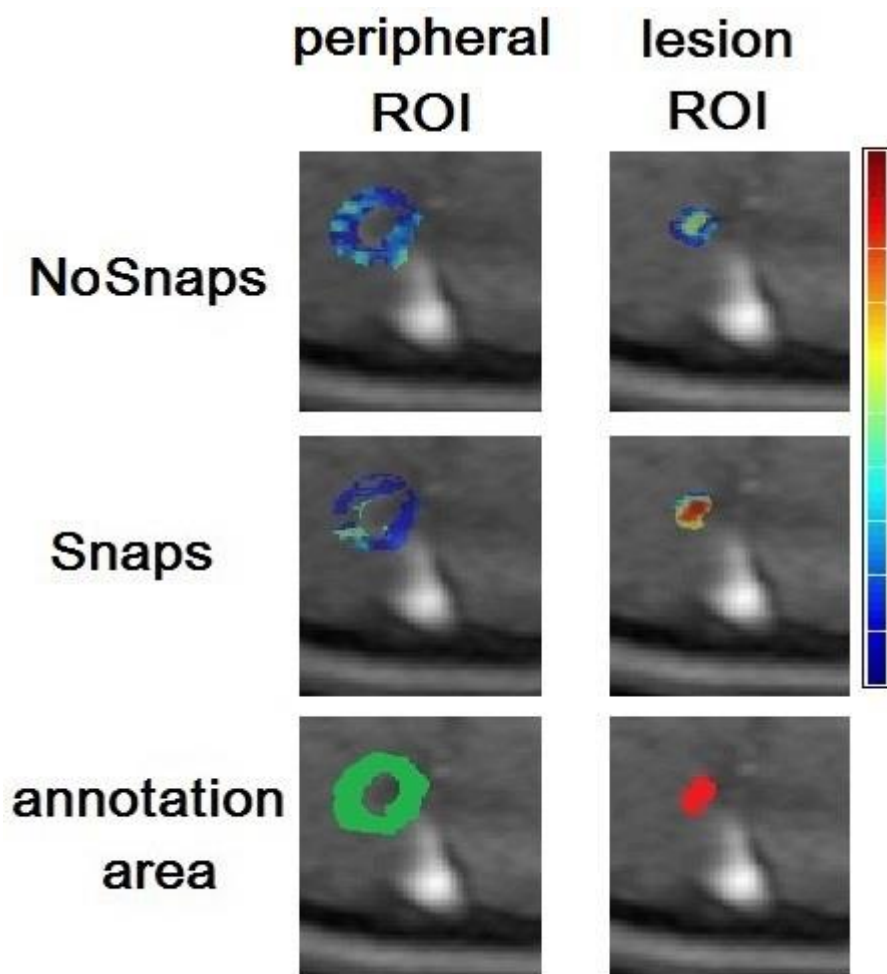


Figure 29. A sample figure displaying  $\text{adj-R}^2$  values (pseudo-color scale) computed for the periphery of the lesion (left-hand column) and the active lesion ROI (right-hand column) using the NoSnaps (upper row) and Snaps (middle row) protocols. Expert-drawn ROIs for the periphery of the lesion (green) and the active lesion (red) are shown in the lower set of images.

In more detail, median values  $\text{adj-R}^2$  were calculated for the active lesion and the peripheral tissue ROI, without applying an  $\text{adj-R}^2$  threshold. Overall, the Snaps

protocol not only achieved better goodness of fit in the ROIs of the active lesions compared to the NoSnaps (NoSnaps: median adj-R<sup>2</sup> = 0.324 (SD=0.204), Snaps: median adj-R<sup>2</sup> = 0.506 (SD=0.192), but also exhibited larger absolute percentage difference between lesion and peripheral tissue. Finally, for all the 24 examined lesions the absolute median percentage change of goodness of fit from the lesions ROIs to the peripheral tissue was 61% for the Snaps protocol compared to 49% for the NoSnaps one.

### 10.3 Discussion

The BBB is a complex structure comprising endothelial cells with tight junctions, perivascular astrocytes and pericyte vessels that separates the brain tissue from the circulating blood and prevents the entry of cells and toxic metabolites into the CNS (255). Post-inflammatory BBB disruption, at the early stages of MS, might be caused by immune-active cells that penetrate the endothelial tight junctions and enter the cerebral tissue (6, 7). This transient breakdown of the BBB allows large, hydrophilic substances, such as Gd-DTPA, to pass through abnormal tight junctions or via pinocytosis (256) and accumulate locally in the affected brain parenchyma. These contrast agents have a shortening effect on the longitudinal relaxation time (T<sub>1</sub>), causing increased signal intensities in areas with BBB disruption. In the clinical setting, contrast-enhanced T<sub>1</sub> weighted MRI is useful to detect focal BBB disruption in active MS lesions (116) and prove dissemination of the disease in space and time, which is essential for making an early diagnosis of MS (12). Although BBB leakage is more prominent in active, focal lesions, increased BBB permeability has also been proved in diffuse NAWM areas (25, 257), while there is also evidence of persistent BBB abnormalities in chronic inactive lesions (24). Since the impairment of BBB function is

of vital importance for the pathogenesis of MS, many treatment strategies target to the resolution of inflammation and protection of BBB function (1, 2). Consequently, the detection and accurate quantification of the BBB permeability is very important for the diagnosis, determination of disease activity and estimation of treatment efficacy in MS.

To this end, a novel time-extended DCE-MRI protocol called Snaps, tailored for quantifying subtle BBB disruption is proposed, providing extended temporal perfusion information, at the expense of minimally extending the conventional DCE acquisition time. Furthermore, this novel Snaps protocol combined with the extended Tofts PK model, resulted in better spatial characterization of the MS enhancing lesions, in terms of quantifying a significantly greater number of pixels with adequate fitting accuracy. Most importantly, these pixels were found to lie in the low  $k^{\text{trans}}$  range, indicating improved detection and quantification of even subtle BBB disruption in patients with RRMS.

In previous studies, that also examined the dynamics of late enhancement on MS lesions (188-190) time extended DCE protocols were utilized in MS patients, with acquisition time extending up to 155 mins (190). These time-consuming protocols could not easily be applied in clinical practice. On the contrary, the proposed time-extended DCE-MRI protocol achieved to extend the window of perfusion observation by 17 mins in average, by minimal prolonging the examination time, 1 min on average. Moreover, other studies have been concentrated on finding subtle BBB disruption in NAWM (4, 5, 25, 76, 185, 186) and GM (5) of MS patients or on visibly non-enhancing MS lesions (4, 76, 181, 182, 189), pointing out the importance of quantifying these

non-visible BBB disruptions by PK modeling. In the current study, a similar approach is being followed by trying to quantify more accurately even non-visible parts of the enhancing MS lesions.

Other studies investigated the optimal protocol and acquisition parameters in combination with model selection for the accurate quantification of low BBB permeabilities. Both Cramer et al. (3) and Barnes et al. (173) found that Patlak model is the most accurate for low BBB leakage quantification under certain circumstances. More specific, Patlak model is able to measure accurately low BBB disruptions when back-diffusion is ignored, thus the total measurement duration considering the permeability of the lesion that is measured, plays a key role in the accuracy and precision of the results. Moreover Barnes et al. (173) concluded that baseline acquisition should be long enough, one to four minutes, in order to provide accurate permeability estimation on Patlak model. Both studies also reported that when using Patlak to quantify low permeabilities ( $k^{\text{trans}} < 2 \cdot 10^{-3}$  1/min), increased acquisition times (>15 min) will significantly improve the measurement accuracy.

Sampling rate is another parameter that may influence the accuracy of the measurement, so there should be taken into account the lesion that will be quantified, the PK model that will be used and the fact that an enhanced lesion usually presents high variation in the very first samples, after the CA injection, and afterwards there is a medium to low variation on the SI. Jelescu et al. (177) proposed a dual temporal resolution protocol that is described by high temporal resolution and low spatial resolution in the first minute of perfusion in order to efficiently capture the first-pass bolus. For the following 20 minutes, protocol resolution changes to low temporal and

high spatial in order to ensure accurate detection and segmentation of even small MS lesions. This protocol was also used by Haar et al. (187) to study subtle BBB leakages appearing in Alzheimer neurodegenerative disorder, while in the same study it was reported that shorter scan times can lead to significantly overestimated permeabilities in lesions that are described by low BBB leakage.

Comparing the methodology presented herein to previous studies (188-190), it is reported that in this study a quantitative perfusion protocol is utilized that is able to quantify even subtle BBB leakage, and is not based on a visual inspection of the SI changes that provide a binary result (i.e. enhancing or not), or T1 relaxation times that still are prone to inaccuracies biased from inherent protocol parameters. Moreover, compared with the previously reported dual temporal resolution protocol (177), the proposed method in this study achieved to sufficiently capture the first-pass bolus considering a sufficient temporal resolution of 11.3 sec without compromising the spatial resolution in the first minute of the perfusion, and preserving high spatial resolution,  $512 \times 512$  pixels, for the entire duration of the perfusion. The methodology presented herein, provided permeabilities that are in the same range of values with results from previous studies (3, 177) and the previously reported overestimation of permeabilities when using short scan times as well as the fact that at long scan times  $k^{\text{trans}}$  boxplots tend to skew towards higher  $k^{\text{trans}}$  values Figure 27 from Haar et al. (187) and Bae et al. (258) are confirmed. Moreover, permeabilities resulted from Patlak model are significantly decreased compared to those resulted from Tofts and extended Tofts models, that is in-line with previous findings (3, 177). Finally, previously reported model and acquisition parameters for measuring subtle BBB disruptions are maintained, considering that in this study the time of perfusion

observation was kept long enough (average 26 mins), the baseline acquisition was about 1 min, and the temporal resolution was 11.3 sec, an adequate interval in order to efficiently capture the first pass bolus dynamics.

Regarding to the model selection part of this work, taking into account that active lesions are being studied and the fact that these lesions might have different degree of BBB disruptions, it cannot be reported that only subtle BBB disruptions are being measured. In contrast, using this methodology and considering the novel time extended perfusion protocol, it is reported that the low BBB permeabilities can be also accurately quantified, providing a more precise identification of the aforementioned lesions.

The principal limitation of the current work is the limited patient sample size that may be inadequate in order to draw definite conclusions concerning the added-value of the proposed method. Future work in this direction needs to further investigate the accuracy of the current methodology using larger and more diverse patient cohorts. Moreover, in future work, visibly non-enhancing lesions and NAWM regions can be examined with the aforementioned methodology, in order to examine for subtle BBB disruptions in these areas. Considering the methodology of this work, the interpolation method for embedding the Snaps protocol into the conventional perfusion protocol, could be replaced with a more robust method in order to exclude inaccuracies in the intermediate time samples. Finally, the methodology presented herein could be applied to other pathologies in order to extract information from additional perfusion biomarkers and investigate the reproducibility of the current

method, in cases that late enhancement can reveal critical pathophysiological processes, such as on brain tumors.

#### 10.4 Conclusion

DCE-MRI is the major imaging technique for BBB leakage quantification in MS lesions. Considering reports from previous studies, most MS lesions are described by low BBB permeabilities compared with tumors, induce to the requirement of increased acquisition time on the perfusion studies. Longer scan time implies increased number of measurements (samples) thus more time for the CA to extravasate to the measured tissue. This indicates higher tissue concentrations that is of major importance when trying to measure subtle BBB disruptions. Furthermore, considering the necessity of minimizing the patient examination time in the MR system, it is of great importance to provide new methods that extend the time of perfusion observation without charging the examination time. In this study we compared three different PK models and two DCE-MRI protocols and by measuring even subtle BBB disruptions we achieved a better spatial characterization and quantification of the enhancing MS lesions with minimal extension of the MRI acquisition time. To this end, the quantification of the DCE perfusion parameters in NAWM and MS and CIS lesions of variable SI and enhancement on T1 sequences, could be facilitated, also, by the Snaps method. To further investigate this hypothesis we applied both the two DCE-MRI protocols in a cohort of MS and CIS patients, as will be analytically presented in the next chapter.

## 11 Application of DCE perfusion MRI in CIS and MS patients and correlation of PK parameters with neuropsychiatric measures.

### 11.1 Introduction

Cognitive disturbances are known to occur in MS and CIS patients, even at the earliest stages of the disease (259, 260), inadequately explained by the brain morphological changes, as detected on conventional MRI techniques (261-264). Few studies on CIS patients have explored the nature of their neuropsychological impairment. This has included verbal short-term and working memory, speed of information processing, and, secondarily, executive function and attention (265, 266). Some researchers have suggested that the most frequently affected domain is attention and concentration along with verbal fluency (267, 268). It is presently unclear whether the detected variability in performance relates to clinical features, such as clinical presentation, disease progression and physical disability or to imaging findings (266, 269). To date, associations have been established between the location of visible lesions and cerebral atrophy with cognitive and emotional symptoms in MS (261, 262).

Non-conventional MRI techniques revealed widespread hemodynamic and microstructural brain damage in MS and CIS patients, invisible by conventional MRI, that may be related to specific domains of cognitive dysfunction (262, 264). In a previous study investigated the relation between hemodynamic measurements and memory function in patients with CIS, using DSC-perfusion MRI and estimating CBV, CBF and MTT values in NAWM and normal appearing deep gray matter structures, CIS patients showed significantly impaired scores on working memory and secondary verbal memory that correlated inversely with elevated CBV values in the left frontal and periventricular NAWM, thalamus, right caudate and corpus callosum, brain

regions thought to be involved in memory function. These observations suggested that inflammation-related processes, which represent the initial neuropathological change of MS, may be of sufficient magnitude to disrupt crucial interhemispheric connections and connections with left frontal lobe cortical regions, ultimately affecting working memory (263).

While contrast enhancing lesions on T1w protocols is a strong indication of inflammation in MS, the BBB disruption and the changes in perfusion parameters indicate an early step in the development of a new lesion. Many studies have examined the PK parameters in active, inactive as well as in other brain regions (3, 24, 173, 177-180), highlighting the importance of the BBB function. The related literature review concerning DCE MRI quantification in MS lesions is reported thoroughly in chapter 5.2, while in CIS there is no extensive application. In summary, previous studies report a trend of increasing permeability from healthy controls brain tissues, followed by NAWM areas of MS patients, and non-enhancing lesions, while the contrast enhancing lesions represented the leakiest tissues (24, 178-180). Furthermore, the high influence of the quantification procedure by the noise of the measurement procedure (173), as well as ,the importance of increasing the acquisition time when trying to quantify subtle BBB leakages has been highlighted (173, 177, 188, 189).

To our knowledge, there are not studies in the literature investigating the role of perfusion characteristics of CIS and MS patients, derived from the application of the DCE-perfusion MRI, in the prediction of their cognitive and emotional status. In the current study we applied an optimized DCE-MRI protocol, using the Patlak method, in

patients with CIS and MS and measure hemodynamic indices, such as K-trans in NAWM (as opposed to active lesions), in relation to neuropsychological data.

## 11.2 Methods

### 11.2.1 Participants

The present study utilized DCE-MRI data from 69 patients diagnosed with CIS or RRMS who had available neuropsychiatric data. CIS and RR patients were recruited through the MS epidemiology program project of Crete and fulfilled the clinical and MRI criteria of the international panel on MS. Patients were recruited during July of 2015 and December of 2018. The hospital review board approved the study and informed written consent was obtained from all subjects prior to participating in the study.

Clinicians obtained a detailed health history from all participants. Exclusion criteria included the pre-existing neurological or psychiatric disorder. Patients or healthy subjects with MRI markers of small vessel disease associated with cognitive impairment, such as lacunes, periventricular or deep white matter confluent hyperintensities, enlarged perivascular spaces, cerebral microbleeds or cortical superficial siderosis, were, also, excluded from the study.

Specifically, the CIS group consisted of 37 consecutive patients who had experienced a single neurological episode (initial clinical attack) without having experienced a recurrence up to the time of the baseline MRI assessment. The majority of CIS patients did not have clinical or paraclinical evidence for dissemination in space (monofocal presentation), whereas others presented such evidence (multifocal presentation). None of the CIS patients included in the study had received steroids for

at least 3 months prior to study inclusion and none of them was on any immunomodulatory treatment.

Diagnosis of 32 RRMS was based on the criteria for clinically definite MS, with a relapsing-remitting course and mild physical disability. The diagnosis of each MS case included in this study was confirmed by a specialist neurologist, using the clinical and MRI criteria of the International Panel on MS. Onset of disease was defined as the year the patient first experienced clear symptoms of MS. A relapse was defined as the appearance of new neurological symptoms or a worsening of pre-existing symptoms lasting for at least 24 h and preceded by a period of clinical stability or improvement of at least 30 days. Other exclusion criteria included (a) history of alcohol or drug abuse, head injury with loss of consciousness, schizophrenia or bipolar disorder, learning disability, or any other neurological disorder, (b) autoimmune and/or immune-mediated diseases and infectious diseases, and (c) significant visual or motor impairment that would interfere with executive function. The two groups were comparable on age ( $p=.3$ ), education level ( $p=.3$ ), and gender ratio ( $p=.6$ , see Table 10) although, as expected, RR-MS patients scored higher on EDSS ( $p < 0.001$ ), had longer illness duration ( $p < 0.05$ ), and larger total volume of MS lesions ( $p < 0.001$ ).

*Table 10. Demographic and clinical information by group.*

	CIS (n=37)	RR-MS (n=32)
Age in years, Mean (SD)	36.3 (8.6)	34.1 (9.2)
Range	21-60	16-58
Education in years, Mean (SD)	12.7 (3.3)	14.0 (3.1)

Women	24 (64.9%)	23 (71.9%)
EDSS**	1.2 (0.8)	2.2 (1.0)
Range	0-3.5	1-4.5
Illness Duration (years)*	3.3 (2.9)	5.6 (5.7)
Range	0-10	0-20
MS lesion volume (mm3) **	3.0 (4.7)	8.5 (8.2)
Range	0-19.0	0.2-36.4

---

EDSS: Expanded Disability Scale \*p<0.05, \*\*p < 0.001.

### 11.2.2 Neuropsychological assessment

The battery of neuropsychological tests included verbal short-term and working memory, passage and list learning and delayed recall tasks, vocabulary and verbal fluency tasks, visual motor processing speed and sustained attention, and set-shifting ability.

Verbal episodic memory was assessed using the Greek adaptation of the Rey Auditory Verbal Learning Test (270). Visuomotor processing speed was assessed through the Trail Making Test (TMT) Part A (271) and manipulative motor dexterity and efficiency using the Grooved Pegboard Test (Lafayette Instrument, Lafayette, IN, USA). Executive tests included TMT Part B, and the Semantic and Phonemic Verbal Fluency tasks (272).

Normative data from the Greek population were available on each measure from a sample of 550 native Greek individuals aged 16-65 years stratified by educational level and geographic origin (cities with population over 10,000: 54%, towns with population ranging between 2,000-5,000: 29%, and towns with population

under 2,000: 17% (273)). This approach permitted computation of age- and education-adjusted standard scores, separately for six subgroups defined by age (16-38 and 39-60 years) and education level (0-9, 10-12, and 13+ years of formal education).

Self-reported symptoms of anxiety and depression were recorded using the Greek version of the Hospital Anxiety and Depression Scale (HADS) (274), with a widely employed cutoff for clinically significant anxiety or depressive symptomatology of 7/8 points. Cronbach's  $\alpha$  scores were .83 and .84 for the Anxiety and Depression scales, respectively (270-275).

### 11.2.3 Scanning and data processing

All exams were performed on a 1.5T MR scanner (Hybrid Vision/Sonata, Siemens/Erlangen, Germany). Given that quality assurance protocols are embedded in a routine QA program for the specific head coil, it can be stated that SNR is greater than 100, when using phantom measurements (ACR100), with tolerance levels at <5% on a year basis. Under this rationale, this can provide that measurements stemming from the proposed protocol does not suffer from signal fluctuation or temporal signal drift. Extensive protocol description is provided in section 10.1.1.

All the examined lesions were analyzed using the Patlak model (174) which according to previous findings gives accurate results on small BBB leakage. Prior to PK analysis, mFAs data (single T1-w acquisitions with different flip angles) were used in order to accurately convert SIs into CA concentration. A population averaged arterial input function (AIF) from Weinmann et al. was used for analyzing the exams (213). Finally estimated biomarkers were limited in physiological interpretable values  $k_{trans} < 5$  1/min,  $v_p < 1$ .

Measurements of  $k_{trans}$  and  $v_p$  values were obtained within focal white matter and in 12 NAWM areas in patients, involving periventricular and deep frontal, parietal, temporal and occipital WM, separately in each hemisphere. The focal white matter lesions were identified on T2-weighted images, and classified as isointense, mildly hypointense, or severely hypointense, according to their signal intensity on pre-contrast T1-weighted images. The isointense and mildly hypointense lesions were defined as having equal or lower signal intensity, respectively, compared to that of white matter, whereas severely hypointense lesions were seen as having very low signal intensity (between that of gray matter and cerebrospinal fluid). Regions of interest (ROIs) were manually drawn by a neuroradiologist, with 20 years of neuroradiological experience, on the DCE source images and automatically transferred to the  $k_{trans}$  and  $v_p$  maps (

Figure 30).

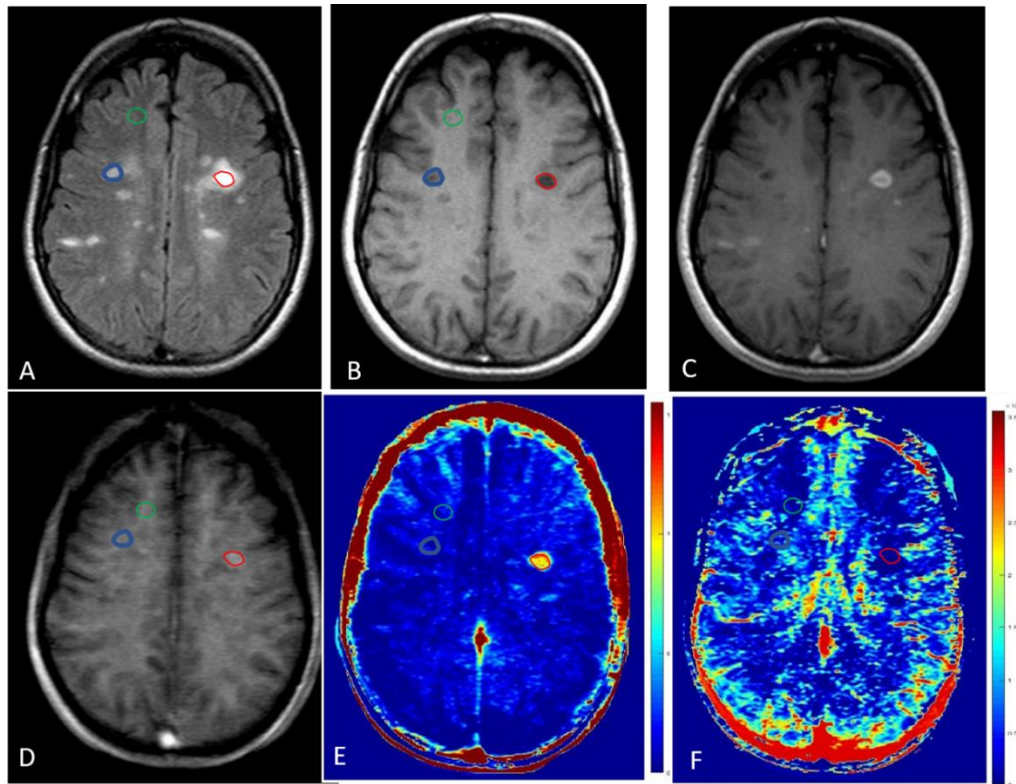


*Figure 30 FLAIR (A), T1SE before (A) and after (C) Gd administration, 3D-T1 VIBE (D), Ktrans map (E) and vp map (F) in a patient with RRMS. ROIs are manually drawn in NAWM (green), mild hypointense on T1 (blue) and severe hypointense peripherally enhancing lesion (red).*

Demographic and clinical characteristics as well as neuropsychological test scores were compared between groups using independent samples t-tests. Systematic variability in k-trans values, measured with each method, between NAWM and each of three lesion types (isointense, mild, severe) were assessed via paired-samples t-tests. These group-based tests were conducted on k-trans and vp values obtained by averaging across all lesions measured in each patient which were compared to the global average k-trans and vp values across all NAWM ROIs for each participant. Bonferroni-adjusted p-value was set at  $0.05/3 = 0.017$  for three pairwise comparisons

(isointense vs NAWM, mild vs NAWM, severe vs NAWM). This approach, although suitable for comparisons of lesion measurements against NAWM, was not deemed suitable for comparisons between lesion types, given the very small n for certain comparisons (<20 participants who had isointense and severe lesions). Therefore, lesion-based analyses were conducted in order to compare lesion types. These were in the form of two-way mixed ANOVAs with two levels for the lesion type variable (isointense vs. mild, isointense vs. severe, or mild vs. severe), and group as the between-subject variable. The p value was set to  $0.05/3 = .016$ .

Finally, associations between k-trans and vp values and clinical characteristics (illness duration, EDSS) or neuropsychological test performance (both raw and age- and education-adjusted z scores, based on Greek population norms) were assessed through Pearson correlation coefficients stratified by group.

## 11.3 Results

### 11.3.1 Neuropsychiatric status of patients with CIS and RR-MS

Neuropsychiatric assessment data were available on 26 patients with CIS and 15 patients with RR-MS. The two subgroups were comparable on age ( $p=.9$ ), education level ( $p=.2$ ), and gender ratio ( $p=.3$ ). As shown in Table 11**Error! Reference source not found.** the two clinical groups performed at comparable levels on all tests administered with the exception of the tasks assessing visuomotor coordination and fine motor skills (Trail Making Test and Pegboard task), where patients with RR-MS significantly underperformed patients with CIS. Inspection of standard scores indicates that both patient groups performed, on average, very close to the expected values according to their age and education levels with certain exceptions. Specifically,

RR-MS patients' average scores were approximately 2 SDs below the expected mean on the Pegboard task.

*Table 11. Cognitive and emotional status of CIS and RR-MS patients.*

	CIS (n=26)	RR-MS (n=15)	P value
AVLT Total Score (z)	-0.39 (1.0)	-0.01 (1.1)	0.2
AVLT Trial 7 (z)	-0.40 (1.3)	-0.14 (1.0)	0.2
AVLT Retention (z)	-0.21 (1.4)	0.1 (0.9)	0.7
Semantic Verbal Fluency (z)	-0.11 (1.0)	-0.14 (1.1)	0.5
Phonemic Verbal Fluency (z)	0.01 (1.1)	-0.21 (0.9)	0.6
TMT-A (z)	0.50 (0.7)	-0.10 (0.9)	0.02
TMT-B (z)	0.90 (1.3)	-0.16 (1.9)	0.04
Pegboard (Dominant hand [z])	-0.20 (1.2)	-2.19 (3.2)	0.02
Pegboard (Non- dominant [z])	-0.04 (1.5)	-2.05 (2.3)	0.006
HADS Anxiety	7.55 (5.0)	8.9 (4.7)	0.4
% >8 points	27.3%	46.2%	0.3
HADS Depression	3.6 (3.8)	4.9 (2.3)	0.3
% >8 points	11.5%	13.3%	0.9

Notes. Unless otherwise indicated values correspond to mean (SD)

### 11.3.2 k-Trans and vp in lesions vs NAWM using the Snap as compared to the NoSnap method

There were no significant differences between average k-trans or vp values of NAWM and three types of lesions (isointense, mild, severe) obtained using the NoSnaps method (Figure 31), although k-trans values in enhancing lesions were significantly higher than k-trans in NAWM.

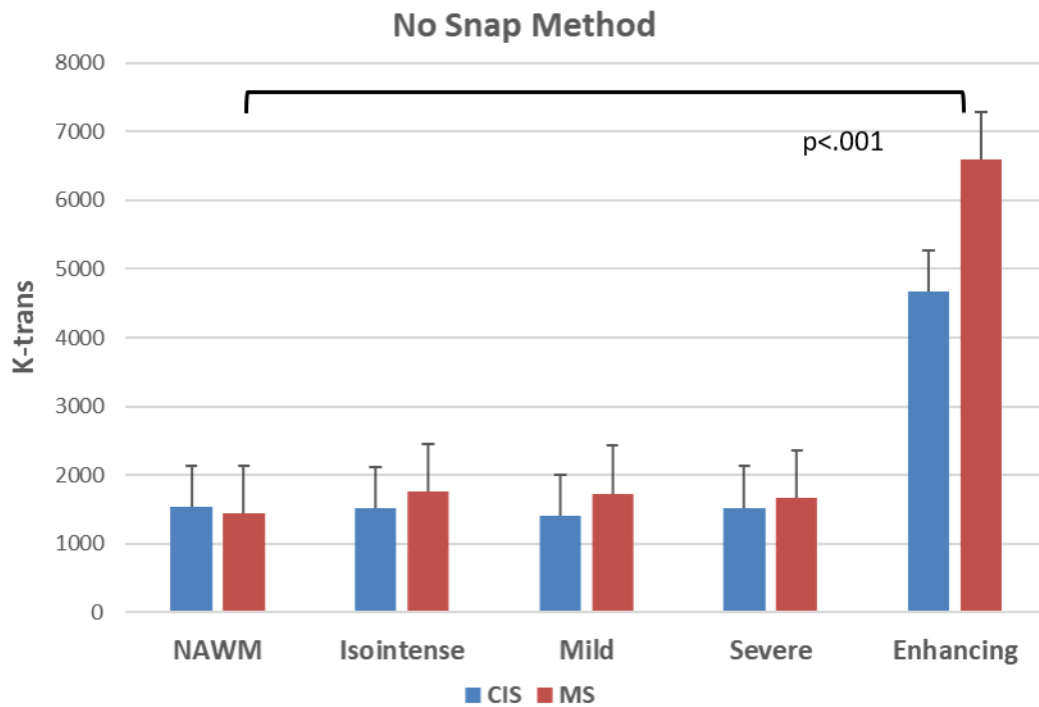


Figure 31. Average k-Trans values obtained using the NoSnap method for the average NAWM and four types of lesions. Vertical lines represent standard error.

On the contrary, by using the Snaps method, k-trans values of average NAWM were found to be significantly lower compared to the respective values of mild hypointense lesions ( $p=0.02$ ), severe hypointense lesions ( $p=0.0007$ ) and enhancing lesions ( $p=0.002$ ) in both CIS and RRMS patients (Figure 32).

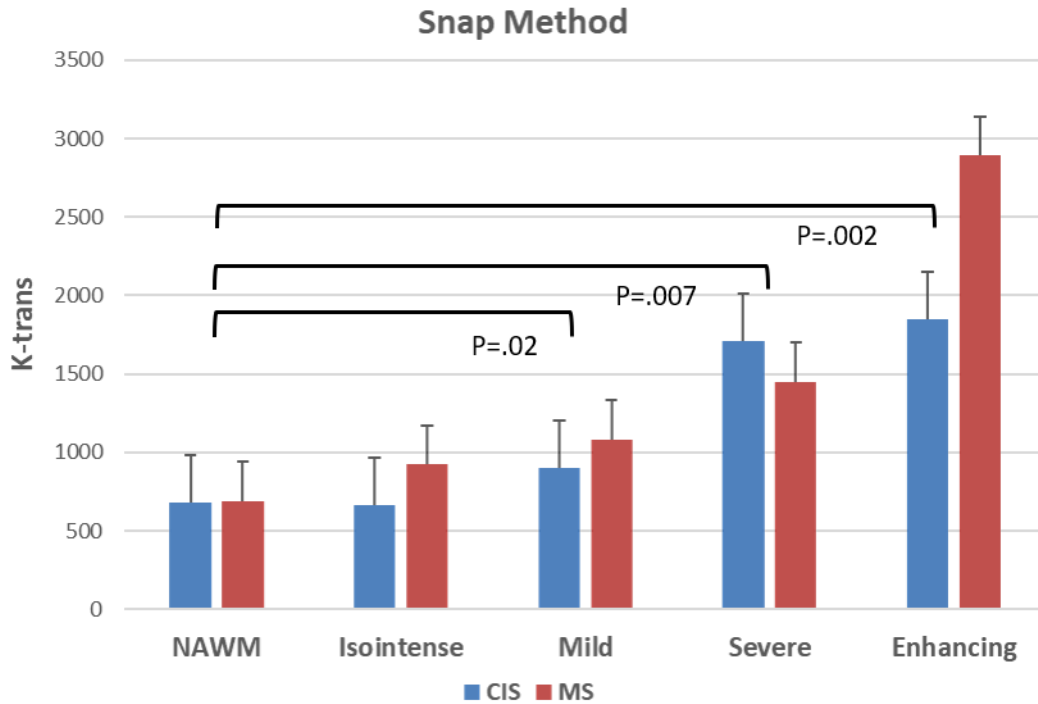


Figure 32. Average k-Trans values obtained using the Snap method for the average NAWM and four types of lesions. Vertical lines represent standard error. Brackets indicate significant differences between values in NAWM and three lesion types across clinical groups.

### 11.3.3 Comparison of clinical groups on k-trans and vp

Higher k-trans values (Nosnaps) were found among patients with CIS as compared to the RR-MS group in two NAWM ROIs: right occipital,  $F(1,67) = 5.94$ ,  $p=0.017$ , and left prefrontal,  $F(1,67) = 3.85$ ,  $p=0.05$  (Figure 33). The two groups did not differ significantly on k-trans or vp in any NAWM ROI using the Snap method. In addition, higher vp values were found in the MS group in the right temporal NAWM ( $F[1,67]=4.32$ ,  $p=0.042$ ), using the Nosnaps method.

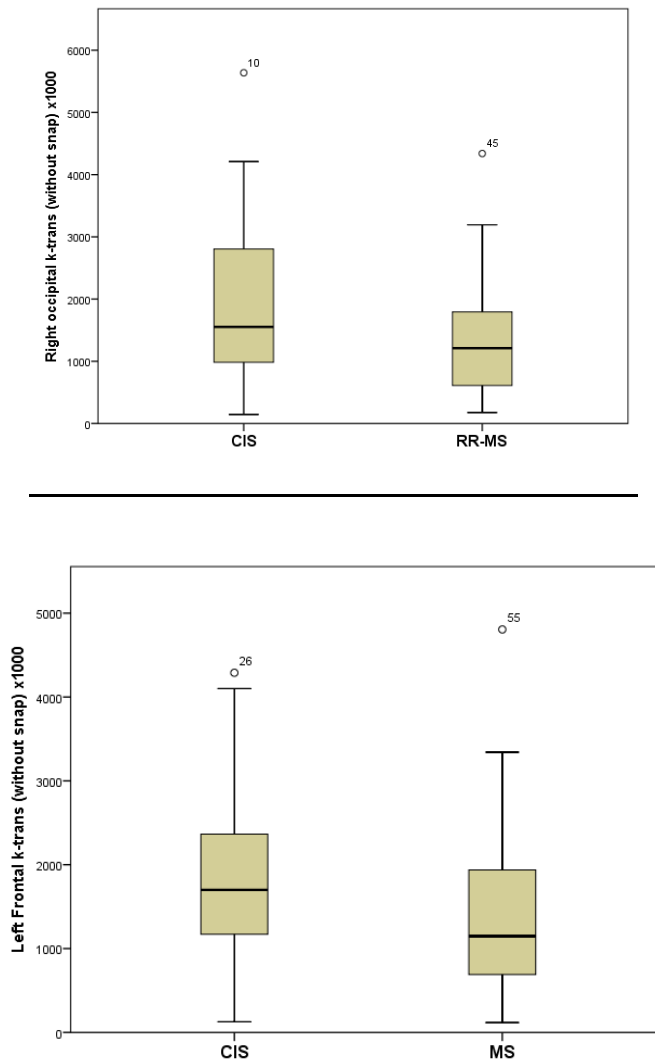
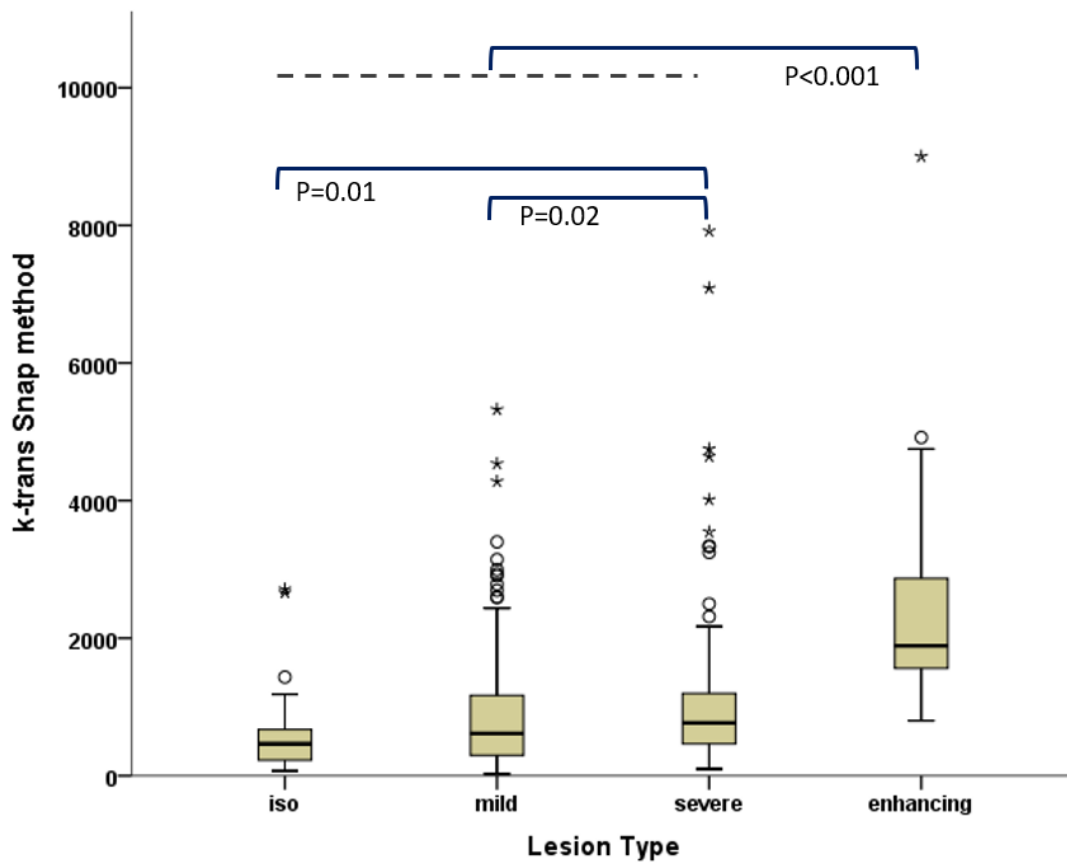


Figure 33. *k-trans* in frontal NAWM measured without snap as a function of clinical group.

#### 11.3.4 *K-trans* and *vp* as a function of lesion type

In per-lesion analyses, we compared *ktrans* values obtained with the snap or no-snap method as a function of lesion type and group via two-way mixed ANOVAs. A total of 611 lesions were measured (66 isointense, 357 mild hypointense, 165 severe hypointense and 26 enhancing). Significant main effect of lesion type was found for both snap ( $F[3,603] = 12.801, p < 0.001$ ) and no-snap methods ( $F[3,603] = 48.253, p < 0.001$ ) in the absence of a group main effect ( $p > .1$ ) or a group by lesion type interaction ( $p > .1$ ). For snap-derived data, pairwise tests indicated that *ktrans* values

were significantly higher in severe as compared to either isointense ( $p=0.01$ ) or mild hypointense lesions ( $p=0.02$ ), which did not differ from each other ( $p=.2$ ). For no-snap-derived data, ktrans values were comparable across isointense, mild hypointense and severe hypointense lesions ( $p>0.3$ ). K-trans values in enhancing lesions were significantly higher than k-trans in all other lesion types using either method ( $p<0.001$ ). There were no significant difference among the vp values of the different lesions types for either the no-snap or snap method.



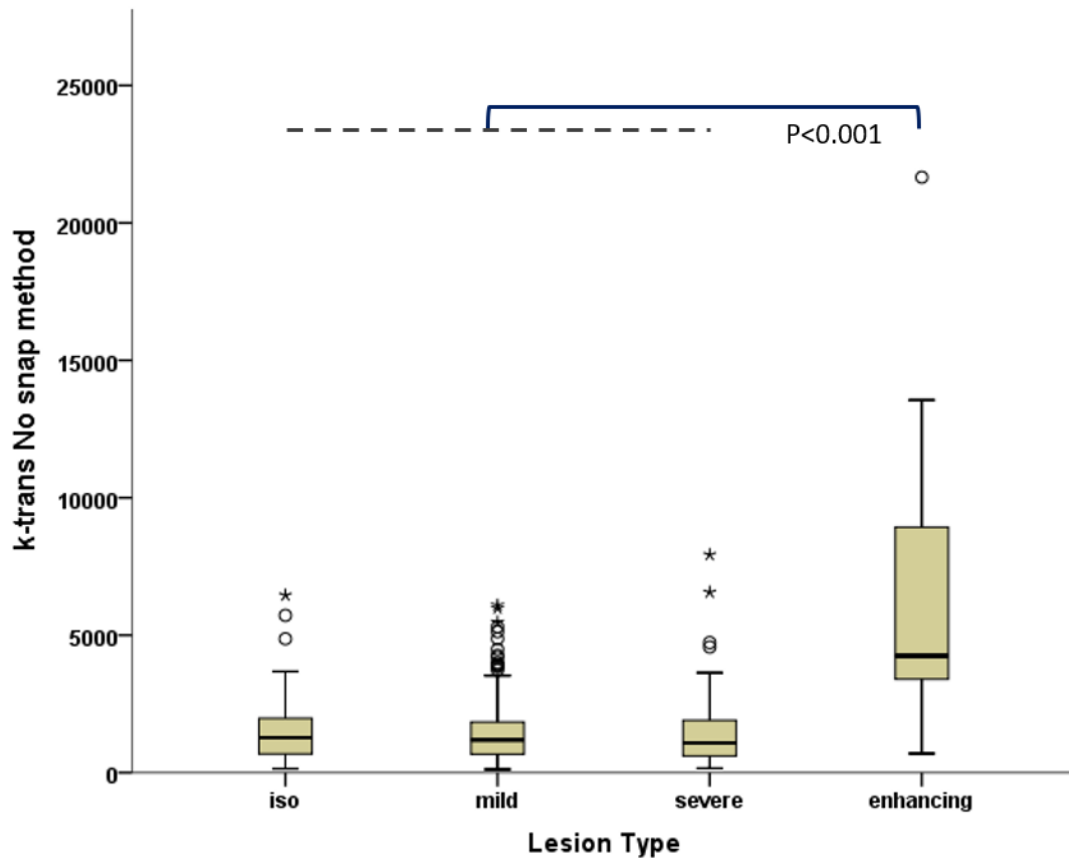


Figure 34. K-trans as a function of lesion type using the snap (upper panel) and no-snap method (lower panel).

### 11.3.5 Clinical correlates of k-trans and vp values in NAWM

In view of the moderate correlations between EDSS/illness duration and total MS lesion volume, all subsequent analyses included the latter variable as a covariate. Moderate-size partial correlations between k-trans values with clinical variables were restricted to EDSS with the no-snap method. Among patients with CIS EDSS physical burden of the disease positively correlated with k-trans in right occipital ( $r=0.47$ ,  $p=0.007$ ) and left thalamus ( $r=0.43$ ,  $p=0.01$ ). In the RR-MS group positive correlations with EDSS were found in left frontal ( $r=0.43$ ,  $p=0.022$ ) and parietal ROIs ( $r=0.56$ ,

$p=0.003$ ). All other correlations with illness duration and EDSS were  $|r| < 0.1$ , as well as all correlations with Vep values.

#### 11.3.6 Neuropsychiatric status as a function of k-trans values in NAWM

Several significant associations between k-trans values with age- and education-adjusted neuropsychiatric test scores, controlling for total lesion volume, were found in both patient groups (see Table 12, Table 13). As shown in Figure 35, these were more extensive in the RR-MS group. Specifically, higher k-trans values in the left frontal NAWM were significantly associated ( $p < .01$ ) with lower scores on both verbal learning and delayed retention indices (AVLT total words recalled over 5 learning trials and AVLT delayed recall of the list of 15 words), and with lower scores on the semantic verbal fluency test (number of animal, fruit, and object names retrieved from semantic memory in 60''). Somewhat weaker associations in the same direction were noted with k-trans values in bilateral periventricular and left semioval NAWM. Finally, fine motor efficiency (time to complete the Grooved Pegboard test) was positively related to k-trans values in the basal ganglia (lenticular nucleus) and frontal NAWM. Notably, the latter associations were properly lateralized, so that unimanual performance depended upon k-trans values in the contralateral lentiform nucleus and frontal NAWM.

Associations of neuropsychological test scores with k-trans measured using the snap method (and with vp measures obtained with either method) did not approach significance ( $P > .1$ ).

Table 12. Pearson correlation coefficients between *k*-trans (no-snap method) and test scores (age- and education level-adjusted) in the RR-MS group.

	AVLT Immediate recall	AVLT Delayed Recall	AVLT Retention	Semantic fluency	GP (R hand)	GP (L hand)	HADS Depression
L Thalamus							0.71***
R Thalamus						0.53*	0.43*
L Lenticular					0.76***	0.60*	
R Lenticular						0.73**	
L Caudate					0.50*		
L Frontal	-0.78**	-0.77**	-0.76**	-0.62**	0.63**	0.49	
R Frontal					0.44	0.72**	
L PVL	-0.58*	-0.58*	-0.59*		0.55*		
R PVL	-0.62*	-0.62*	-0.75**				
L Semioval	-0.61*	-0.55*	-0.52*				

\*\*\*p<0.001, \*\* p<0.01, \* p<0.05. Note all other |r|<0.3. GP: Grooved pegboard test

Table 13. Pearson correlation coefficients between *k*-trans (no-snap method) and test scores (age- and education level-adjusted) in the CIS group.

	AVLT Immediate recall	AVLT Delayed Recall	AVLT Retention	Semantic Fluency
L Thalamus	-0.58**	-0.42*	-0.32	
L Lenticular				
L Frontal	-0.40*	-0.44*		
L PVL				-0.42*
R PVL				-0.44*
L Parietal				-0.44*
L Occipital	-0.55**			
R Occipital				
L Semioval				-0.49*
R Semioval	-0.55***	-0.55***	-0.56***	-0.59***

\*\*\*p<0.001, \*\* p<0.01, \* p<0.05. Note all other |r|<0.3; Snap method in bold, no-snap method in italics. GP: Grooved pegboard test

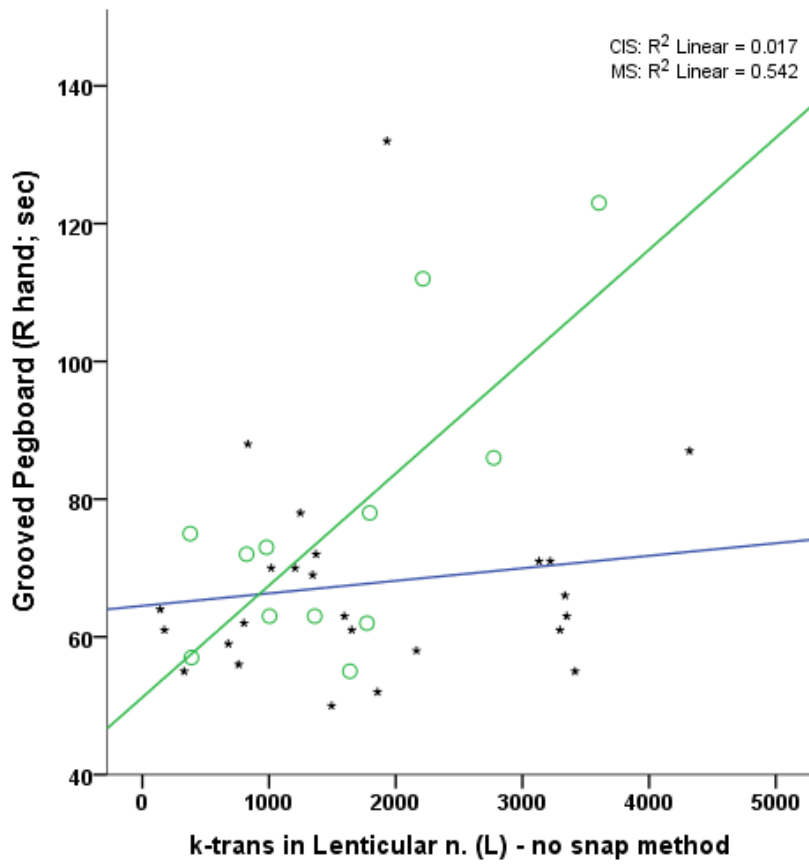
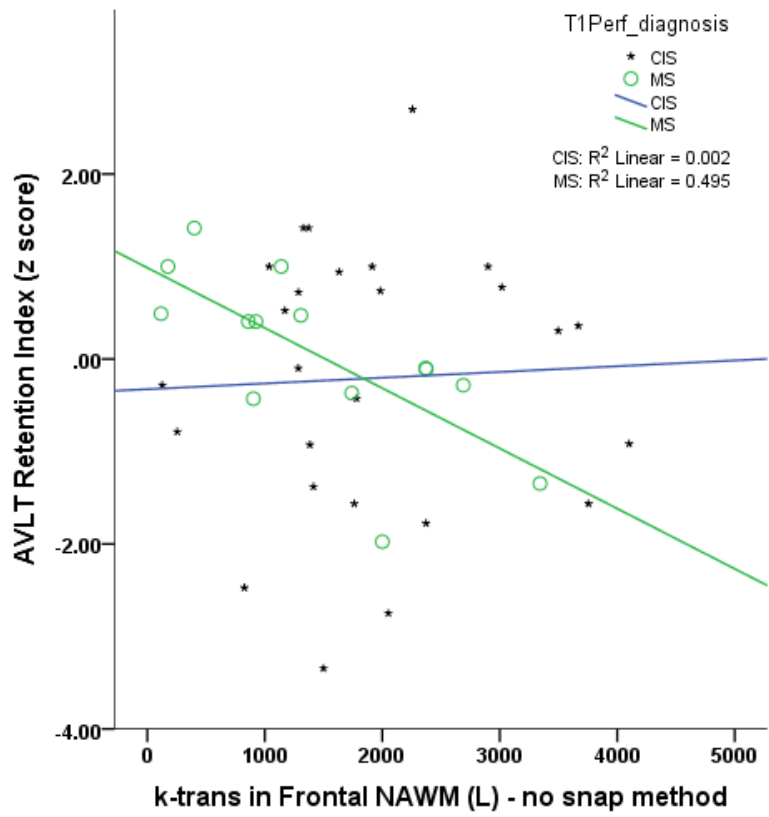


Figure 35 Associations between *k-trans* values in the frontal NAWM (left hemisphere) with the capacity to form long term episodic memories (upper panel) and between *k-*

*trans in the lentiform nucleus and fine motor efficiency (lower panel; note that higher scores indicate worse performance). Best-fitting regression curves are shown separately for each group (linear fit).*

## 11.4 Discussion

### **Neuropsychiatric status of patients with CIS and RR-MS**

On average the two clinical groups performed at comparable levels on the majority of cognitive tests administered, with the exception of the test assessing visuomotor coordination and fine motor efficiency. Taken together these results suggest that patients in the present cohort experienced little or no impact of the disease on brain circuits responsible for language, memory, and executive functions. Moreover, the two groups were comparable on levels of self-reported anxiety and depression measures, which may have affected cognitive performance. With respect to depression symptoms, in particular, the frequency of patients reporting clinically significant symptomatology (as indicated by HADS scores >8) was only 11.5% and 13.3% in the CIS and MS groups, respectively,

### **Permeability as a function of lesion type**

Concerning the differentiation accuracy of the two examined DCE protocols,  $k_{trans}$  values from the novel proposed Snaps protocol achieved to better discriminate the NAWM from the iso, mild and severe lesions, while NoSnaps protocol didn't found significant differences between NAWM and the three types of lesions (isointense, mild, severe). The better discrimination accuracy is speculated to be due to the extending acquisition time that is able to quantify more accurately the permeability of the underlying areas. Furthermore, the lower permeabilities of the time extended protocol in comparison with the conventional protocol, agree with reports from

previous research (187, 258). Finally, higher ktrans values were found in the right occipital and left prefrontal NAWM areas of CIS patients compared to the MS patients, that could be attributed to higher degree of diffuse low grade inflammation in the NAWM of CIS patients compared to the respective WM areas of MS, where an ischemic substrate predominates (76).

Snaps protocol achieved better discrimination of the three types of plaques, compared to the NoSnaps method, a further indication of the added value that extension of the imaging time provided. This research part reported that severe lesions are described by higher permeabilities compared to the mild hypointense or isointense lesions. The higher permeability observed in severe hypointense lesions could be attributed to the peripherally enhancing reactivated chronic lesions included in this category. Nosnaps protocol didn't identified significant differences among different lesions types. According to a previous report, no significant differences were found between the PK parameters of hypointense and isointense lesions (25). Finally, enhanced lesions showed increased permeability compared to non-enhancing lesions, a finding that agrees with previous reports (76), and reflect the increased inflammatory activity of the active plaques.

### **Neuropsychiatric status as a function of k-trans values in NAWM**

Concerning the correlation between the permeability values and the clinical and neuropsychological variables, only the NoSnaps method resulted in moderate correlations, in right occipital and left thalamus for the CIS patients, while for the MS cohort there were found positive correlations in left frontal and parietal. These results are expected in view of the crucial role of frontoparietal circuits in motor control and

conduction of somatosensory input which are, in turn, reflected in overall physical capacity as measured by EDSS. Snaps protocol didn't reveal notable correlations.

Considering more sensitive indices of motor function, obtained using the Grooved Pegboard test, there were strong indications that increased ktrans values in NAWM and basal ganglia involved in the frontostriatal motor control circuit were related to less efficient fine motor control. These associations were restricted to patients suffering from the most severe impairment in motor efficiency (MS group). In addition, increased ktrans values in left frontal NAWM correlated significantly with both episodic and semantic memory retrieval as measured by retention capacity of a newly-learned supraspan word list and efficient retrieval of animal, fruit, or object names from semantic memory. These results are consistent with the role of the left prefrontal cortex in verbal retrieval. Importantly the aforementioned associations were regionally specific and independent of total lesion burden.

Reports from previous studies are conflicted, since some studies have found correlations of structural changes with clinical disability (276-278), while other report that they didn't found any correlation (181, 182). Considering that quantification of DCE MRI data is a procedure prone to errors and influenced by several protocol related and PK analysis parameters, as well as the conflicted results from the previous studies, the correlation of clinical measures with imaging results is an open research field that needs further standardization.

### 11.5 Conclusion

In this part of the dissertation, we examined the correlations of the conventional and the novel proposed time extended perfusion MRI protocols with the

neuropsychologic data. Research findings concerning a sub-cohort of the overall study population, showed positive correlations, while the novel proposed perfusion protocol seems to provide better correlations in some test cases. Future work includes the extension of the results of the present study in the overall patient cohort.

## 12 Correlation of T1 (DCE) with T2\* (DSC) perfusion parameters

### 12.1 Introduction

There are few studies employing DSC-MRI in patients with clinically definite MS, revealing diffuse hemodynamic impairment both in NAWM and in deep gray matter (DGM) areas (149, 156, 158, 163, 279). The findings were thought to reflect primary vascular pathology rather than decreased metabolic demand. On the other hand, increased perfusion has been found in acute enhancing and in some chronic reactivated non-enhancing MS plaques, indicating that DSC-MRI is sensitive in detecting inflammatory activity in acute phases of the disease (154). Furthermore, results from the present research team revealed increased CBV values in all regions of the NAWM and of the DGM evaluated in patients with CIS, as compared to patients with RRMS and to controls. In contrast, the CBF values of the caudate and thalami were significantly lower in patients with CIS than in controls (166). These could have resulted from diffuse inflammation-mediated vasodilatation or even angiogenesis at the earliest stage of MS, leading to focal ischemia in some DGM regions in patients with CIS and global ischemia in patients with RRMS.

Finally, it should be mentioned that there is no research in the literature that correlates DSC and DCE MRI data. DSC MRI provides quantification of hemodynamic measurements, such as the CBF, which is the volume of blood passing through a given amount of brain tissue per unit of time, CBV, that indicates the volume of blood in a given amount of brain tissue and MTT which is the average time that blood cells spend within a determinative volume of capillary circulation. On the other side, the most relevant biomarkers that DCE MRI quantification provides, are the measurement of BBB permeability ( $k_{trans}$ ) and the volume extravascular extracellular space (EES). To

this purpose, the main motivation of the following research, is to examine the underlying relationships among these two different perfusion techniques, and the provided biomarkers, in MS and CIS patients.

## 12.2 Methods

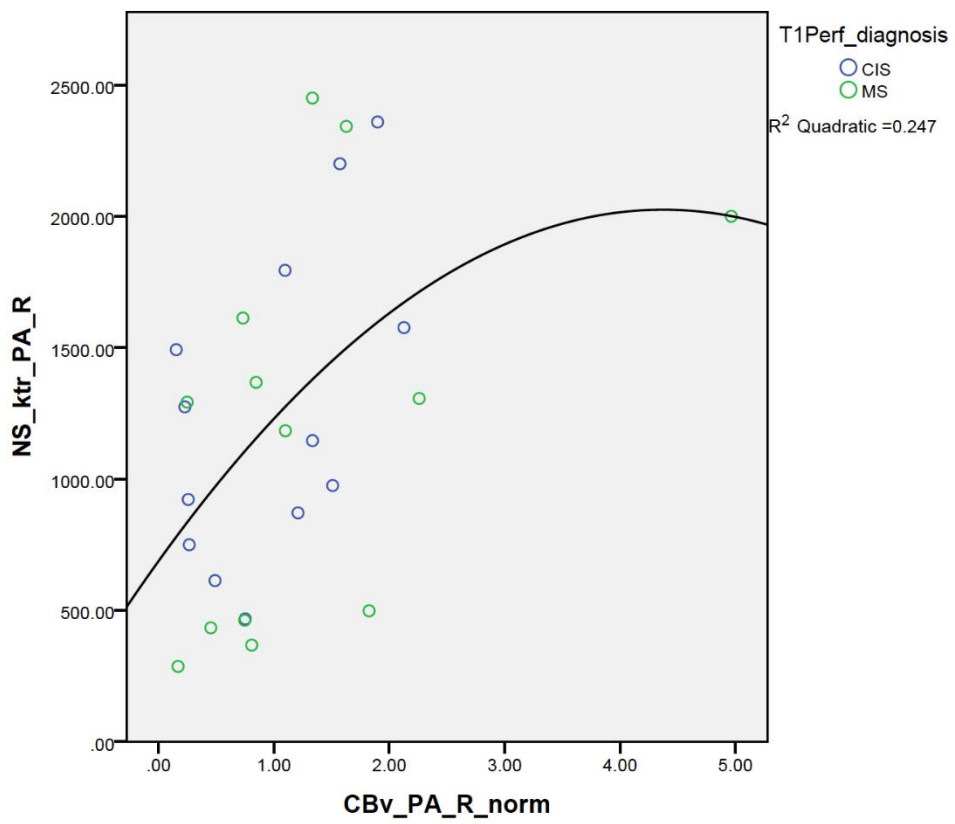
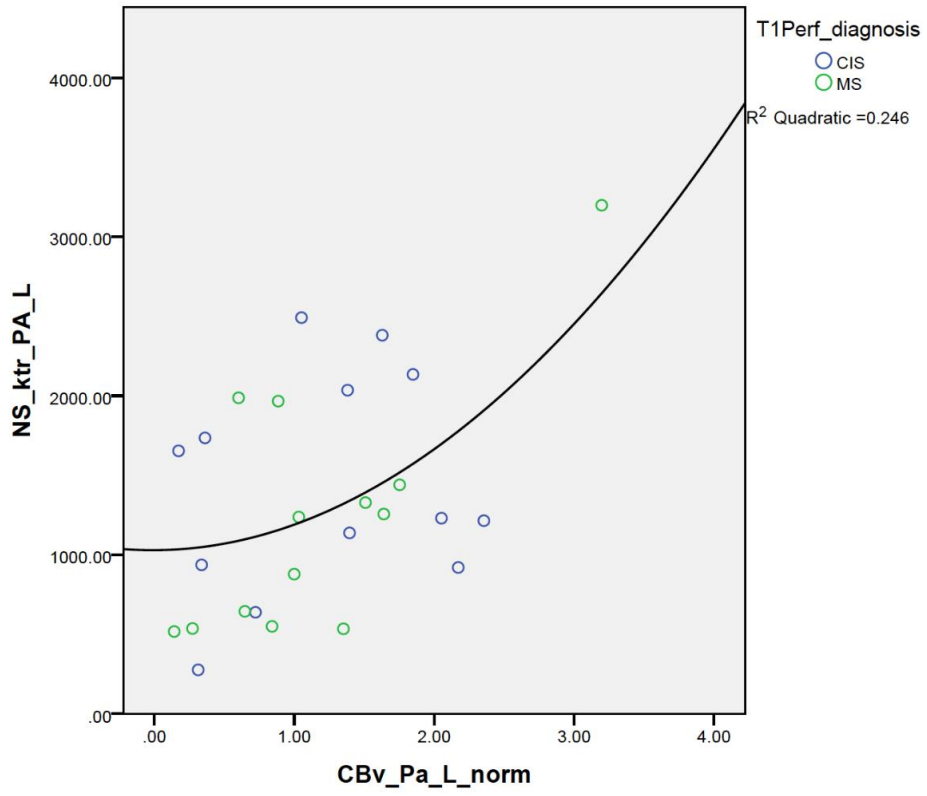
The DSC-MRI technique was performed utilizing a dynamic two-dimensional single-shot multislice GRE EPI sequence (TR/TE, flip angle 1500 ms/40 ms/30°, bandwidth 2442 Hz/pixel, echo spacing 0.47 ms and EPI factor 64), after intravenous administration of a single dose (0.1 mmol/kg) of gadobutrol. Twenty axial consecutive slices of 4 mm slice thickness and 1.5 mm inter-slice gap were obtained covering the entire brain. The sequence was repeated every 1.5 s for a total time of 1 min and 20 s, thus obtaining 50 dynamic acquisitions with 1.5 s temporal resolution for each of the 20 anatomical slices. The arterial input function was calculated and parametric maps of relative CBV, cerebral blood flow (CBF) and mean transit time (MTT) values were created automatically, using standard software provided by the manufacturer. In order to compare between subjects, the calculated relative CBV, CBF and MTT values were normalized for each patient with respect to the average values of CBF and MTT of the dentate gyrus and the Cornu ammonis 2 and 3 fields (DG/CA23) of the hippocampi (set at 45 ml/100/ml/min and 4 s respectively), a region assumed not to be affected in early MS (166). Normalized CBV, CBF and MTT values were calculated for the same regions of interest located at the NAWM areas and focal WM lesions as described in chapter 10.

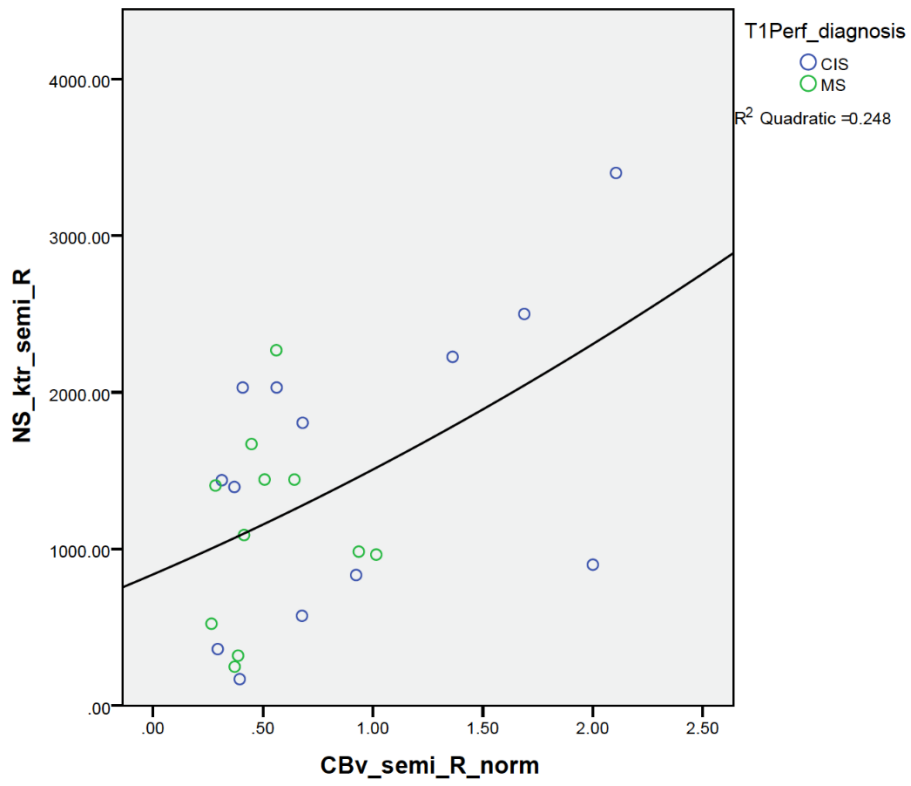
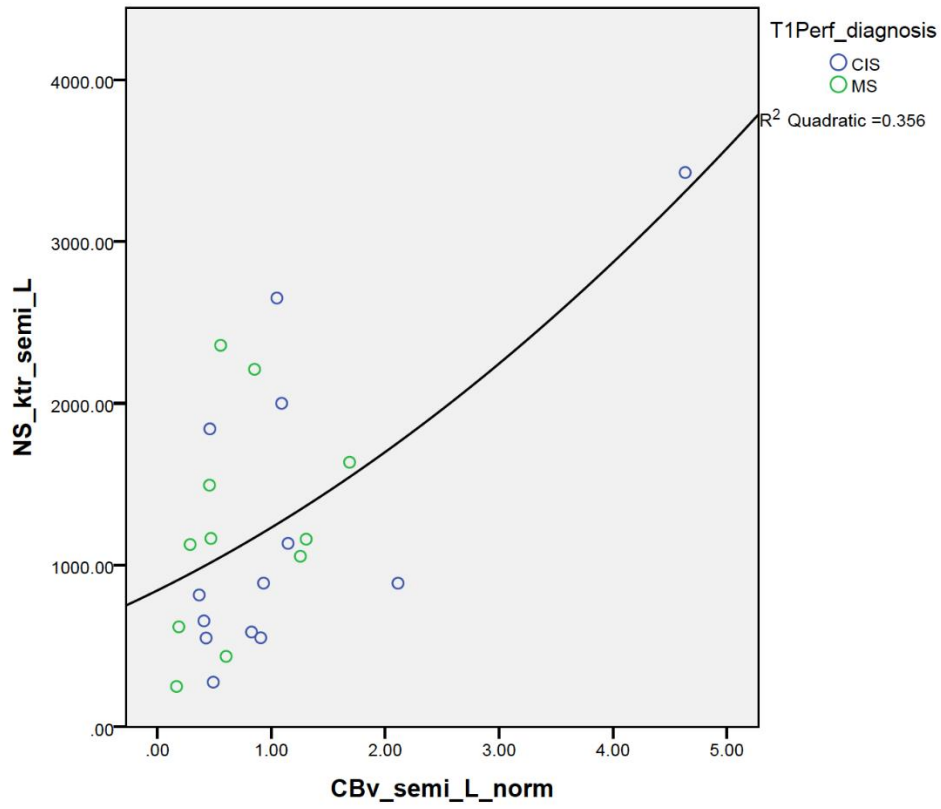
DCE and DSC data were available on 16 patients with CIS (11 women) and 14 patients with RR-MS (11 women) with mean age of 34.6 (SD=7.2) and 35.6 (SD=9.5) years, respectively, and average EDSS of 1.3 (SD=0.9) and 2.4 SD=1.3), respectively.

Associations between normalized CBV and CBF and k-trans values were examined through linear and quadratic bivariate regression models.

### 12.3 Results

Due to the small group size associations between k-trans and normalized CBV (or CBF) were assessed in the total sample. Significant positive correlations were found in five ROIs between normalized CBV and k-trans values obtained using the no-snap method, including bilateral parietal, semioval and splenium NAWM. Inspection of the regression plots in Figure 36 suggests that the association between the two sets of measures was best described by curvilinear fit and was not driven by values in a single group of patients. Similar results were noted for normalized CBF values in three NAWM ROIs (left parietal and semioval center bilaterally, see Figure 37).  $R^2$  indices for best-fitting regression models between CBF/CBV and either ktrans values obtained with the snap method or vp values obtained with either methods were  $<0.07$  in all regions measured (Figure 37).





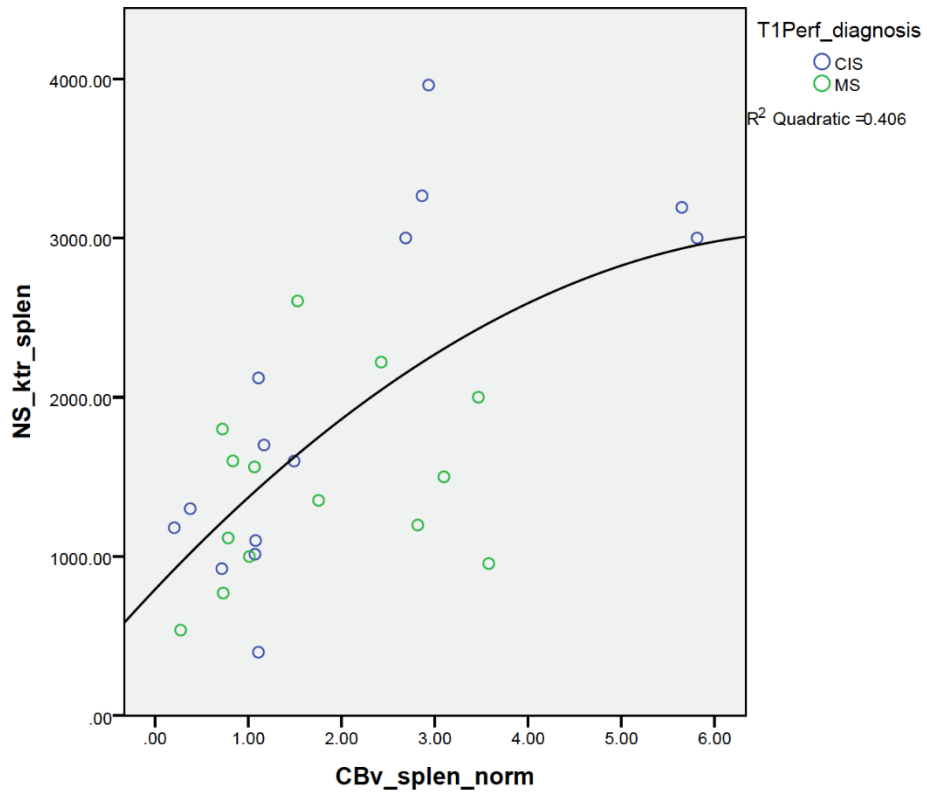
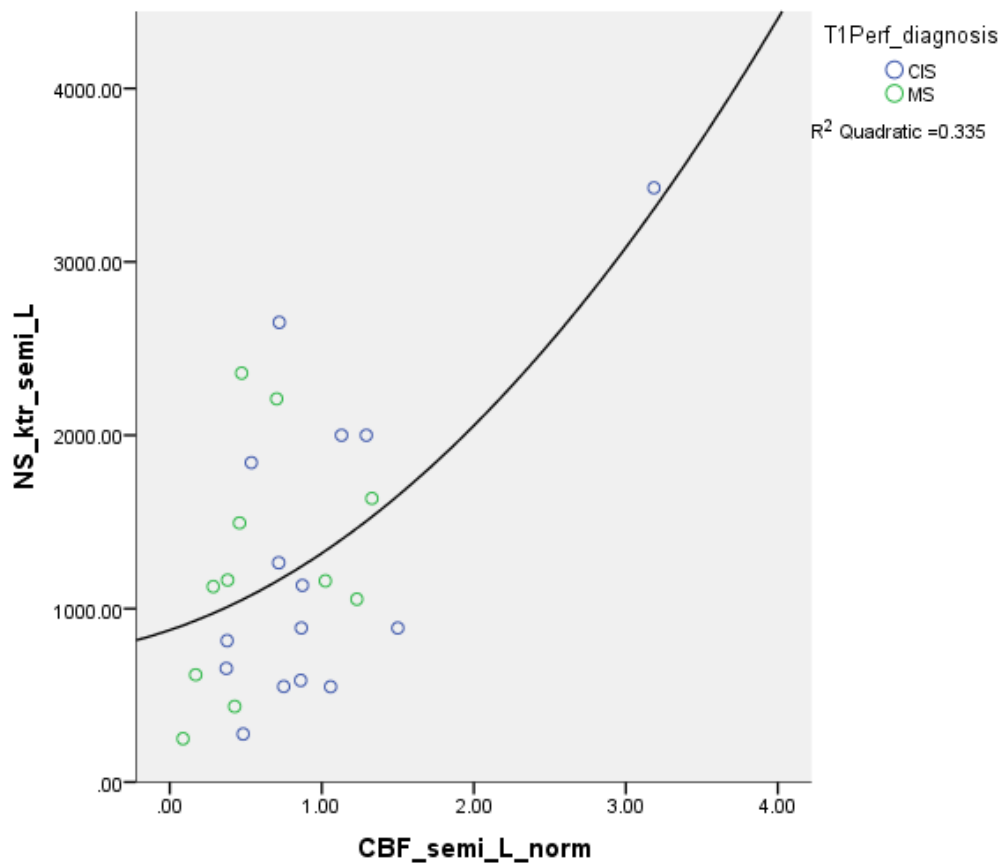
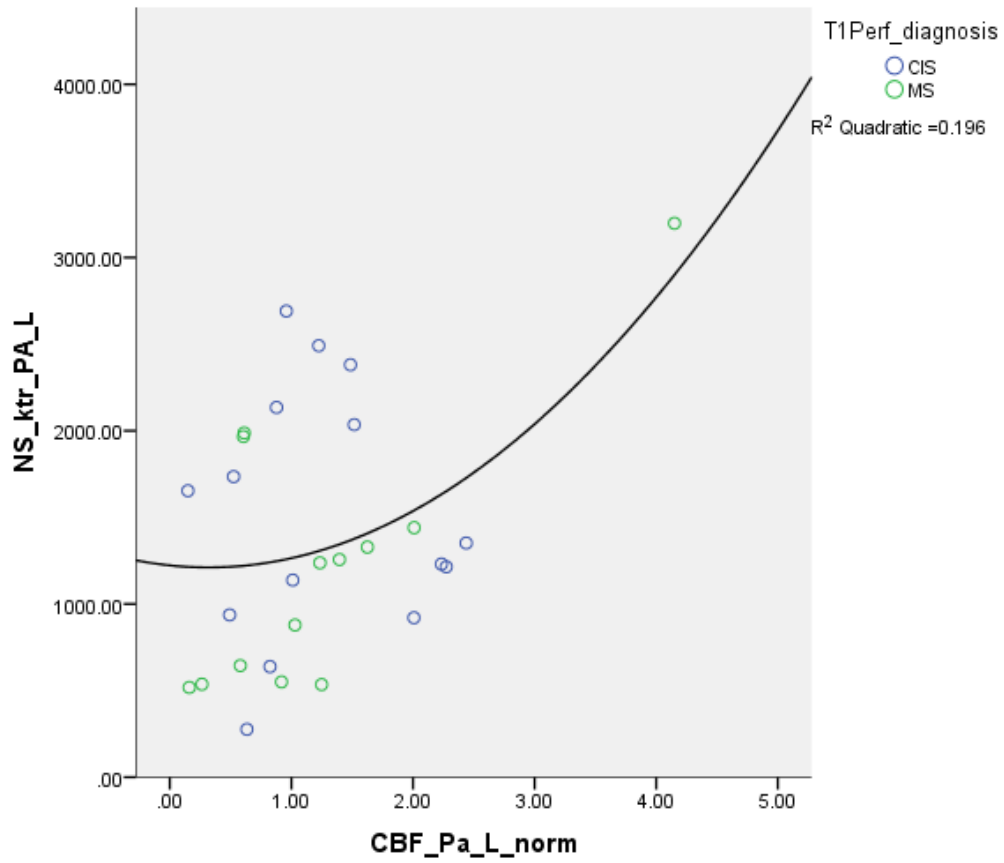


Figure 36. Best-fitting regression curves describing the association between normalized CBV and corresponding k-trans values obtained with the no-snap method in five NAWM ROIs (left & right parietal, left and right semioval center, and splenium of the corpus callosum).



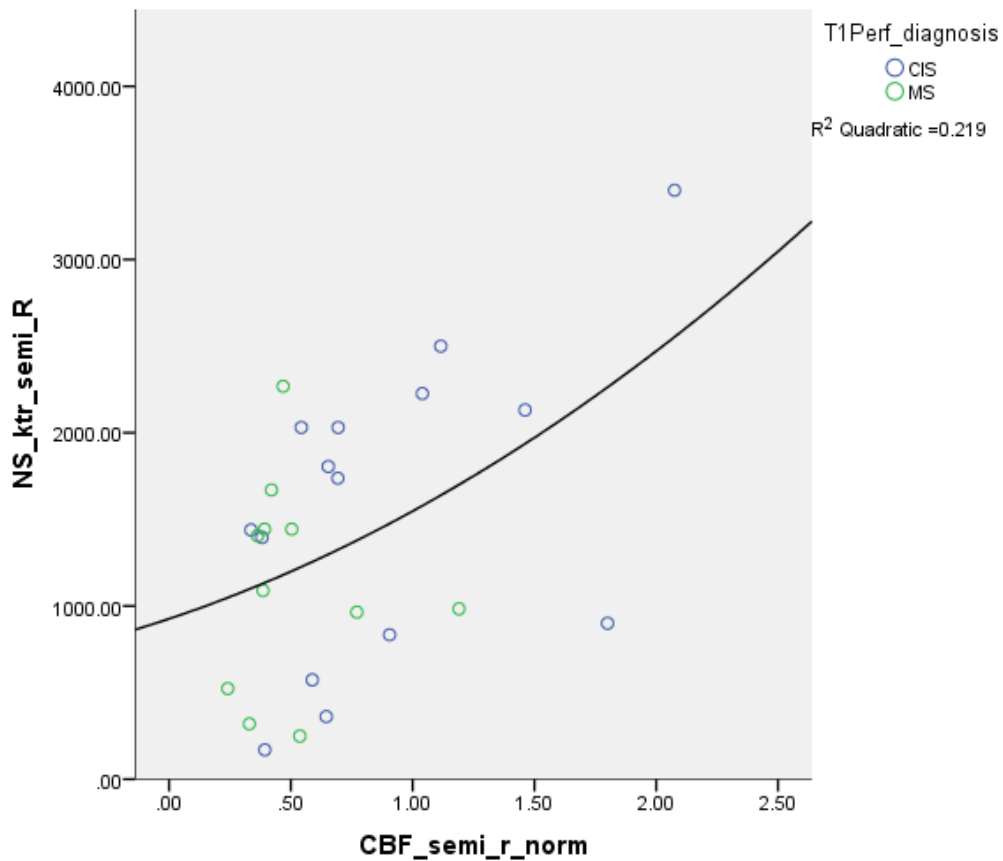


Figure 37 Best-fitting regression curves describing the association between normalized CBF and corresponding k-trans values obtained with the no-snap method in three NAWM ROIs (left parietal, left and right semioval center).

#### 12.4 Discussion

This part of the dissertation examined the relationship among indices derived from two perfusion imaging techniques, DCE (Ktrans) and DSC (CBF, CBV), motivated by the scarcity of similar attempts in the literature. We found modest correlations between CBF and CBV with ktrans in several NAWM regions. In these analyses, which were conducted across clinical groups due to the relatively small sample size, there was some evidence that the degree of association between perfusion indices increased at progressively higher levels of CBF/CBV.

Taking into account that even if DCE and DSC MRI are both MRI perfusion protocols that reveal hemodynamic processes, these are relying on different assumptions, and considering that DSC highlights the susceptibility effects of the paramagnetic CA using T2\* protocols while DCE exploits the relaxivity of the CA on the signal echo by acquiring T1w images before, during and after the intravenous administration. In more detail, DCE investigates the microvascular structure and function from the PK of the CA as this is transported from the brain vasculature. On the other side, DSC MRI is sensitive in detecting inflammatory activity in acute phases of the disease.

The correlation analysis that was conducted in this part of the dissertation, didn't provide strong correlations among the aforementioned parameters. This can be attributed to the fact that even two perfusion techniques are considered, these are based on different assumptions and they model different functionalities of the CA in the brain perfusion MRI.

### 12.5 Conclusion

The results on this chapter of the present dissertation, examined but didn't find any underlying correlations among the DCE and DSC perfusion MRI techniques in MS and CIS patients. This study took place in a sub cohort of the overall patient population, while future work will publish the aforementioned results in the complete cohort of patients. Finally, considering the above mentioned findings, we are concluding that these perfusion techniques are complementary, thus they should be both taken into account in order to obtain a complete imaging framework.

## 13 Added value and future work

The added value of the present study can be split to three sections.

### **1. DCE protocol - tool (disease oriented)**

Initially, a disease oriented framework was implemented, able to quantify accurately the active MS lesions and better characterize spatially of the active lesion part. This framework consisted of the designation of a novel T1 perfusion protocol that achieved to triple the window time of perfusion observation by minimally extending the magnetic resonance acquisition time for all patients. Furthermore, an integrated in-house T1 perfusion platform was implemented for analyzing the aforementioned data. This platform consisted of functionalities from importing medical imaging protocol data, performing data pre-processing computations (such as de-noising), selection from a different PK models, PK maps visualization and exporting. Finally, an extensive analysis was performed for validating the high accuracy of the novel proposed perfusion protocol compared to the conventional in quantifying active MS and CIS lesions, as well as the selection of the proper PK model for accurate quantification and spatial characterization of the active lesion part. Future work in this direction needs to further investigate the accuracy of the current methodology using a larger cohort of patients, while visibly non-enhancing lesions as well as normal appearing white matter can be examined for subtle blood brain barrier disruptions using the proposed framework.

### **2. Application of DCE protocol in CIS and MS patients and correlation with neuropsychological findings**

A second objective of this dissertation was to examine the quantification accuracy in NAWM and demyelinating lesions of CIS and MS patients. Analysis results indicate that time extended DCE protocol achieved better lesion and NAWM areas quantification in comparison with the conventional DCE protocol, while the SNAPS protocol better discriminated the three lesion types as well as the lesions from NAWM.

Moreover, we examined the relationship between regional perfusion changes and neuropsychological dysfunctions in MS and CIS patients. For this purpose, thorough statistical analysis, T1 perfusion maps were correlated with a neuropsychological test battery, with strong correlations found between the perfusion parameters and the clinical and the neuropsychiatric status of the patients. This analysis took place in a sub-cohort of the overall patients, while results concerning the whole cohort will be reported in the near future. Finally, these preliminary results suggest the efficiency of T1 perfusion to constitute a complementary technique to conventional imaging, for non-invasive evaluation of the aforementioned symptoms.

### **3. Correlation of T1 (DCE) with T2\* (DSC) perfusion parameters.**

Finally, in this dissertation we examined the relationship among the DCE and DSC perfusion protocols parameters. Positive correlations were found among CBV, CBF and  $k_{trans}$  in NAWM, but these were described by curvilinear fit and data was not driven by values in a single group of patients. Regarding future work, we will examine the aforementioned results in a study including the complete cohort of patients.

## REFERENCES

1. Ortiz GG, Pacheco-Moisés FP, Macías-Islas M, Flores-Alvarado LJ, Mireles-Ramírez MA, González-Renovato ED, et al. Role of the blood-brain barrier in multiple sclerosis. *Arch Med Res*. 2014;45(8):687-97.
2. Lopes Pinheiro MA, Kooij G, Mizee MR, Kamermans A, Enzmann G, Lyck R, et al. Immune cell trafficking across the barriers of the central nervous system in multiple sclerosis and stroke. *Biochim Biophys Acta*. 2016;1862(3):461-71.
3. Cramer SP, Larsson HB. Accurate determination of blood-brain barrier permeability using dynamic contrast-enhanced T1-weighted MRI: a simulation and in vivo study on healthy subjects and multiple sclerosis patients. *J Cereb Blood Flow Metab*. 2014;34(10):1655-65.
4. Soon D, Altmann DR, Fernando KT, Giovannoni G, Barkhof F, Polman CH, et al. A study of subtle blood brain barrier disruption in a placebo-controlled trial of natalizumab in relapsing remitting multiple sclerosis. *J Neurol*. 2007;254(3):306-14.
5. Ingrisich M, Sourbron S, Herberich S, Schneider MJ, Kümpfel T, Hohlfeld R, et al. Dynamic Contrast-Enhanced Magnetic Resonance Imaging Suggests Normal Perfusion in Normal-Appearing White Matter in Multiple Sclerosis. *Invest Radiol*. 2017;52(3):135-41.
6. Misra A, Ganesh S, Shahiwala A, Shah SP. Drug delivery to the central nervous system: a review. *J Pharm Pharm Sci*. 2003;6(2):252-73.
7. Upadhyay RK. Drug delivery systems, CNS protection, and the blood brain barrier. *Biomed Res Int*. 2014;2014:869269.
8. Heye AK, Culling RD, Valdés Hernández MeC, Thrippleton MJ, Wardlaw JM. Assessment of blood-brain barrier disruption using dynamic contrast-enhanced MRI. A systematic review. *Neuroimage Clin*. 2014;6:262-74.
9. Sourbron SP, Buckley DL. Classic models for dynamic contrast-enhanced MRI. *NMR Biomed*. 2013;26(8):1004-27.
10. Tofts PS, Kermode AG. Measurement of the blood-brain barrier permeability and leakage space using dynamic MR imaging. 1. Fundamental concepts. *Magn Reson Med*. 1991;17(2):357-67.
11. Liu C, Li Wan Po A, Blumhardt LD. "Summary measure" statistic for assessing the outcome of treatment trials in relapsing-remitting multiple sclerosis. *J Neurol Neurosurg Psychiatry*. 1998;64(6):726-9.
12. Polman CH, Reingold SC, Banwell B, Clanet M, Cohen JA, Filippi M, et al. Diagnostic criteria for multiple sclerosis: 2010 revisions to the McDonald criteria. *Ann Neurol*. 2011;69(2):292-302.
13. Brownlee WJ, Miszkiel KA, Altmann DR, Ciccarelli O, Miller DH. Periventricular lesions and MS diagnostic criteria in young adults with typical clinically isolated syndromes. *Mult Scler*. 2017;23(7):1031-4.
14. Leray E, Moreau T, Fromont A, Edan G. Epidemiology of multiple sclerosis. *Rev Neurol (Paris)*. 2016;172(1):3-13.
15. Koch-Henriksen N, Sørensen PS. The changing demographic pattern of multiple sclerosis epidemiology. *Lancet Neurol*. 2010;9(5):520-32.
16. Parnell GP, Booth DR. The Multiple Sclerosis (MS) Genetic Risk Factors Indicate both Acquired and Innate Immune Cell Subsets Contribute to MS Pathogenesis and Identify Novel Therapeutic Opportunities. *Front Immunol*. 2017;8:425.
17. Debouverie M, Pittion-Vouyovitch S, Louis S, Roederer T, Guillemin F. Increasing incidence of multiple sclerosis among women in Lorraine, Eastern France. *Mult Scler*. 2007;13(8):962-7.
18. Midgard R, Riise T, Svanes C, Kvåle G, Nyland H. Incidence of multiple sclerosis in Møre and Romsdal, Norway from 1950 to 1991. An age-period-cohort analysis. *Brain*. 1996;119 ( Pt 1):203-11.

19. Barnett MH, Williams DB, Day S, Macaskill P, McLeod JG. Progressive increase in incidence and prevalence of multiple sclerosis in Newcastle, Australia: a 35-year study. *J Neurol Sci.* 2003;213(1-2):1-6.
20. Ramagopalan SV, Maugeri NJ, Handunnetthi L, Lincoln MR, Orton SM, Dymont DA, et al. Expression of the multiple sclerosis-associated MHC class II Allele HLA-DRB1\*1501 is regulated by vitamin D. *PLoS Genet.* 2009;5(2):e1000369.
21. Hollenbach JA, Oksenberg JR. The immunogenetics of multiple sclerosis: A comprehensive review. *J Autoimmun.* 2015;64:13-25.
22. Confavreux C, Suissa S, Sadiere P, Bourdès V, Vukusic S, Group ViMSS. Vaccinations and the risk of relapse in multiple sclerosis. *Vaccines in Multiple Sclerosis Study Group. N Engl J Med.* 2001;344(5):319-26.
23. Leitner H. Influence of neurosteroids on the pathogenesis of multiple sclerosis. *Med Hypotheses.* 2010;75(2):229-34.
24. Claudio L, Raine CS, Brosnan CF. Evidence of persistent blood-brain barrier abnormalities in chronic-progressive multiple sclerosis. *Acta Neuropathol.* 1995;90(3):228-38.
25. Cramer SP, Simonsen H, Frederiksen JL, Rostrup E, Larsson HB. Abnormal blood-brain barrier permeability in normal appearing white matter in multiple sclerosis investigated by MRI. *Neuroimage Clin.* 2014;4:182-9.
26. Ghasemi N, Razavi S, Nikzad E. Multiple Sclerosis: Pathogenesis, Symptoms, Diagnoses and Cell-Based Therapy. *Cell J.* 2017;19(1):1-10.
27. Gandhi R, Laroni A, Weiner HL. Role of the innate immune system in the pathogenesis of multiple sclerosis. *J Neuroimmunol.* 2010;221(1-2):7-14.
28. Palace J. Making the diagnosis of multiple sclerosis. *J Neurol Neurosurg Psychiatry.* 2001;71 Suppl 2:ii3-8.
29. Bejar JM, Ziegler DK. Onset of multiple sclerosis in a 24-month-old child. *Arch Neurol.* 1984;41(8):881-2.
30. Marrie RA, Yu N, Blanchard J, Leung S, Elliott L. The rising prevalence and changing age distribution of multiple sclerosis in Manitoba. *Neurology.* 2010;74(6):465-71.
31. Weiner HL. A shift from adaptive to innate immunity: a potential mechanism of disease progression in multiple sclerosis. *J Neurol.* 2008;255 Suppl 1:3-11.
32. Miller DH, Chard DT, Ciccarelli O. Clinically isolated syndromes. *Lancet Neurol.* 2012;11(2):157-69.
33. Jacobi C, Hähnel S, Martinez-Torres F, Rieger S, Jüttler E, Heiland S, et al. Prospective combined brain and spinal cord MRI in clinically isolated syndromes and possible early multiple sclerosis: impact on dissemination in space and time. *Eur J Neurol.* 2008;15(12):1359-64.
34. Noseworthy JH, Lucchinetti C, Rodriguez M, Weinshenker BG. Multiple sclerosis. *N Engl J Med.* 2000;343(13):938-52.
35. Kappos L, Polman CH, Freedman MS, Edan G, Hartung HP, Miller DH, et al. Treatment with interferon beta-1b delays conversion to clinically definite and McDonald MS in patients with clinically isolated syndromes. *Neurology.* 2006;67(7):1242-9.
36. Kapoor R, Miller DH, Jones SJ, Plant GT, Brusa A, Gass A, et al. Effects of intravenous methylprednisolone on outcome in MRI-based prognostic subgroups in acute optic neuritis. *Neurology.* 1998;50(1):230-7.
37. Gebhardt M, Kropp P, Jürgens TP, Hoffmann F, Zettl UK. Headache in the first manifestation of Multiple Sclerosis - Prospective, multicenter study. *Brain Behav.* 2017;7(12):e00852.
38. Gelfand JM. Multiple sclerosis: diagnosis, differential diagnosis, and clinical presentation. *Handb Clin Neurol.* 2014;122:269-90.

39. Gronseth GS, Ashman EJ. Practice parameter: the usefulness of evoked potentials in identifying clinically silent lesions in patients with suspected multiple sclerosis (an evidence-based review): Report of the Quality Standards Subcommittee of the American Academy of Neurology. *Neurology*. 2000;54(9):1720-5.
40. Kurtzke JF. Rating neurologic impairment in multiple sclerosis: an expanded disability status scale (EDSS). *Neurology*. 1983;33(11):1444-52.
41. Vellinga MM, Geurts JJ, Rostrup E, Uitdehaag BM, Polman CH, Barkhof F, et al. Clinical correlations of brain lesion distribution in multiple sclerosis. *J Magn Reson Imaging*. 2009;29(4):768-73.
42. Beck J, Rondot P, Catinot L, Falcoff E, Kirchner H, Wietzerbin J. Increased production of interferon gamma and tumor necrosis factor precedes clinical manifestation in multiple sclerosis: do cytokines trigger off exacerbations? *Acta Neurol Scand*. 1988;78(4):318-23.
43. Dettke M, Scheidt P, Prange H, Kirchner H. Correlation between interferon production and clinical disease activity in patients with multiple sclerosis. *J Clin Immunol*. 1997;17(4):293-300.
44. Lucchinetti C, Brück W, Parisi J, Scheithauer B, Rodriguez M, Lassmann H. A quantitative analysis of oligodendrocytes in multiple sclerosis lesions. A study of 113 cases. *Brain*. 1999;122 ( Pt 12):2279-95.
45. Trapp BD, Peterson J, Ransohoff RM, Rudick R, Mörk S, Bö L. Axonal transection in the lesions of multiple sclerosis. *N Engl J Med*. 1998;338(5):278-85.
46. Bjartmar C, Trapp BD. Axonal and neuronal degeneration in multiple sclerosis: mechanisms and functional consequences. *Curr Opin Neurol*. 2001;14(3):271-8.
47. Bitsch A, Schuchardt J, Bunkowski S, Kuhlmann T, Brück W. Acute axonal injury in multiple sclerosis. Correlation with demyelination and inflammation. *Brain*. 2000;123 ( Pt 6):1174-83.
48. Ferguson B, Matyszak MK, Esiri MM, Perry VH. Axonal damage in acute multiple sclerosis lesions. *Brain*. 1997;120 ( Pt 3):393-9.
49. Kuhlmann T, Lingfeld G, Bitsch A, Schuchardt J, Brück W. Acute axonal damage in multiple sclerosis is most extensive in early disease stages and decreases over time. *Brain*. 2002;125(Pt 10):2202-12.
50. Wujek JR, Bjartmar C, Richer E, Ransohoff RM, Yu M, Tuohy VK, et al. Axon loss in the spinal cord determines permanent neurological disability in an animal model of multiple sclerosis. *J Neuropathol Exp Neurol*. 2002;61(1):23-32.
51. Davie CA, Barker GJ, Webb S, Tofts PS, Thompson AJ, Harding AE, et al. Persistent functional deficit in multiple sclerosis and autosomal dominant cerebellar ataxia is associated with axon loss. *Brain*. 1995;118 ( Pt 6):1583-92.
52. De Stefano N, Matthews PM, Fu L, Narayanan S, Stanley J, Francis GS, et al. Axonal damage correlates with disability in patients with relapsing-remitting multiple sclerosis. Results of a longitudinal magnetic resonance spectroscopy study. *Brain*. 1998;121 ( Pt 8):1469-77.
53. Metz I, Weigand SD, Popescu BF, Frischer JM, Parisi JE, Guo Y, et al. Pathologic heterogeneity persists in early active multiple sclerosis lesions. *Ann Neurol*. 2014;75(5):728-38.
54. Lucchinetti C, Brück W, Parisi J, Scheithauer B, Rodriguez M, Lassmann H. Heterogeneity of multiple sclerosis lesions: implications for the pathogenesis of demyelination. *Ann Neurol*. 2000;47(6):707-17.
55. Barkhof F, Bruck W, De Groot CJ, Bergers E, Hulshof S, Geurts J, et al. Remyelinated lesions in multiple sclerosis: magnetic resonance image appearance. *Arch Neurol*. 2003;60(8):1073-81.
56. Brück W, Kuhlmann T, Stadelmann C. Remyelination in multiple sclerosis. *J Neurol Sci*. 2003;206(2):181-5.

57. Prineas JW, Barnard RO, Kwon EE, Sharer LR, Cho ES. Multiple sclerosis: remyelination of nascent lesions. *Ann Neurol.* 1993;33(2):137-51.
58. Kornek B, Storch MK, Weissert R, Wallstroem E, Stefferl A, Olsson T, et al. Multiple sclerosis and chronic autoimmune encephalomyelitis: a comparative quantitative study of axonal injury in active, inactive, and remyelinated lesions. *Am J Pathol.* 2000;157(1):267-76.
59. Duncan GJ, Plemel JR, Assinck P, Manesh SB, Muir FGW, Hirata R, et al. Myelin regulatory factor drives remyelination in multiple sclerosis. *Acta Neuropathol.* 2017;134(3):403-22.
60. Kidd D, Barkhof F, McConnell R, Algra PR, Allen IV, Revesz T. Cortical lesions in multiple sclerosis. *Brain.* 1999;122 ( Pt 1):17-26.
61. Peterson JW, Bö L, Mörk S, Chang A, Trapp BD. Transected neurites, apoptotic neurons, and reduced inflammation in cortical multiple sclerosis lesions. *Ann Neurol.* 2001;50(3):389-400.
62. Dyrna F, Hanske S, Krueger M, Bechmann I. The blood-brain barrier. *J Neuroimmune Pharmacol.* 2013;8(4):763-73.
63. M L. Zur Lehre von der Cerebrospinalflüssigkeit. *ZKlin Med*1900. p. 480–94.
64. Reese TS, Karnovsky MJ. Fine structural localization of a blood-brain barrier to exogenous peroxidase. *J Cell Biol.* 1967;34(1):207-17.
65. Crone C, Olesen SP. Electrical resistance of brain microvascular endothelium. *Brain Res.* 1982;241(1):49-55.
66. Butt AM, Jones HC, Abbott NJ. Electrical resistance across the blood-brain barrier in anaesthetized rats: a developmental study. *J Physiol.* 1990;429:47-62.
67. de Vries HE, Kuiper J, de Boer AG, Van Berkel TJ, Breimer DD. The blood-brain barrier in neuroinflammatory diseases. *Pharmacol Rev.* 1997;49(2):143-55.
68. Shepro D, Morel NM. Pericyte physiology. *FASEB J.* 1993;7(11):1031-8.
69. Hamilton NB, Attwell D, Hall CN. Pericyte-mediated regulation of capillary diameter: a component of neurovascular coupling in health and disease. *Front Neuroenergetics.* 2010;2.
70. Serlin Y, Shelef I, Knyazer B, Friedman A. Anatomy and physiology of the blood-brain barrier. *Semin Cell Dev Biol.* 2015;38:2-6.
71. Davies DC. Blood-brain barrier breakdown in septic encephalopathy and brain tumours. *J Anat.* 2002;200(6):639-46.
72. Powlislock JT, Becker DP, Sullivan HG, Miller JD. Vascular permeability alterations to horseradish peroxidase in experimental brain injury. *Brain Res.* 1978;153(2):223-39.
73. Olmez I, Ozyurt H. Reactive oxygen species and ischemic cerebrovascular disease. *Neurochem Int.* 2012;60(2):208-12.
74. Robberecht W. Oxidative stress in amyotrophic lateral sclerosis. *J Neurol.* 2000;247 Suppl 1:11-6.
75. van Horssen J, Witte ME, Schreiberl G, de Vries HE. Radical changes in multiple sclerosis pathogenesis. *Biochim Biophys Acta.* 2011;1812(2):141-50.
76. Ingrisch M, Sourbron S, Morhard D, Ertl-Wagner B, Kümpfel T, Hohlfeld R, et al. Quantification of perfusion and permeability in multiple sclerosis: dynamic contrast-enhanced MRI in 3D at 3T. *Invest Radiol.* 2012;47(4):252-8.
77. Adams CW, Poston RN, Buk SJ, Sidhu YS, Vipond H. Inflammatory vasculitis in multiple sclerosis. *J Neurol Sci.* 1985;69(3):269-83.
78. Brück W, Bitsch A, Kolenda H, Brück Y, Stiefel M, Lassmann H. Inflammatory central nervous system demyelination: correlation of magnetic resonance imaging findings with lesion pathology. *Ann Neurol.* 1997;42(5):783-93.
79. Miller DH, Rudge P, Johnson G, Kendall BE, Macmanus DG, Moseley IF, et al. Serial gadolinium enhanced magnetic resonance imaging in multiple sclerosis. *Brain.* 1988;111 ( Pt 4):927-39.

80. Minagar A, Alexander JS. Blood-brain barrier disruption in multiple sclerosis. *Mult Scler*. 2003;9(6):540-9.
81. Leech S, Kirk J, Plumb J, McQuaid S. Persistent endothelial abnormalities and blood-brain barrier leak in primary and secondary progressive multiple sclerosis. *Neuropathol Appl Neurobiol*. 2007;33(1):86-98.
82. Traboulsee A, Simon JH, Stone L, Fisher E, Jones DE, Malhotra A, et al. Revised Recommendations of the Consortium of MS Centers Task Force for a Standardized MRI Protocol and Clinical Guidelines for the Diagnosis and Follow-Up of Multiple Sclerosis. *AJNR Am J Neuroradiol*. 2016;37(3):394-401.
83. Filippi M, Rocca MA, Ciccarelli O, De Stefano N, Evangelou N, Kappos L, et al. MRI criteria for the diagnosis of multiple sclerosis: MAGNIMS consensus guidelines. *Lancet Neurol*. 2016;15(3):292-303.
84. Wattjes MP, Rovira À, Miller D, Yousry TA, Sormani MP, de Stefano MP, et al. Evidence-based guidelines: MAGNIMS consensus guidelines on the use of MRI in multiple sclerosis--establishing disease prognosis and monitoring patients. *Nat Rev Neurol*. 2015;11(10):597-606.
85. Bakshi R, Thompson AJ, Rocca MA, Pelletier D, Dousset V, Barkhof F, et al. MRI in multiple sclerosis: current status and future prospects. *Lancet Neurol*. 2008;7(7):615-25.
86. Ormerod IE, Miller DH, McDonald WI, du Boulay EP, Rudge P, Kendall BE, et al. The role of NMR imaging in the assessment of multiple sclerosis and isolated neurological lesions. A quantitative study. *Brain*. 1987;110 ( Pt 6):1579-616.
87. Sheldon JJ, Siddharthan R, Tobias J, Sheremata WA, Soila K, Viamonte M. MR imaging of multiple sclerosis: comparison with clinical and CT examinations in 74 patients. *AJR Am J Roentgenol*. 1985;145(5):957-64.
88. McFarland HF. The lesion in multiple sclerosis: clinical, pathological, and magnetic resonance imaging considerations. *J Neurol Neurosurg Psychiatry*. 1998;64 Suppl 1:S26-30.
89. Achten E, Deblaere K. Health technology assessment on the use of magnetic resonance imaging (MRI) and computed tomography (CT) in the diagnosis of multiple sclerosis (MS) and clinically isolated syndromes (CIS). *Eur J Radiol*. 2008;65(2):211-3.
90. Absinta M, Rocca MA, Colombo B, Copetti M, De Feo D, Falini A, et al. Patients with migraine do not have MRI-visible cortical lesions. *J Neurol*. 2012;259(12):2695-8.
91. Wardlaw JM, Smith EE, Biessels GJ, Cordonnier C, Fazekas F, Frayne R, et al. Neuroimaging standards for research into small vessel disease and its contribution to ageing and neurodegeneration. *Lancet Neurol*. 2013;12(8):822-38.
92. Jurynczyk M, Gheraldes R, Probert F, Woodhall MR, Waters P, Tackley G, et al. Distinct brain imaging characteristics of autoantibody-mediated CNS conditions and multiple sclerosis. *Brain*. 2017;140(3):617-27.
93. Gean-Marton AD, Vezina LG, Marton KI, Stimac GK, Peyster RG, Taveras JM, et al. Abnormal corpus callosum: a sensitive and specific indicator of multiple sclerosis. *Radiology*. 1991;180(1):215-21.
94. Palmer S, Bradley WG, Chen DY, Patel S. Subcallosal striations: early findings of multiple sclerosis on sagittal, thin-section, fast FLAIR MR images. *Radiology*. 1999;210(1):149-53.
95. Zhou F, Shiroishi M, Gong H, Zee CS. Multiple sclerosis: hyperintense lesions in the brain on T1-weighted MR images assessed by diffusion tensor imaging. *J Magn Reson Imaging*. 2010;31(4):789-95.
96. Brex PA, Parker GJ, Leary SM, Molyneux PD, Barker GJ, Davie CA, et al. Lesion heterogeneity in multiple sclerosis: a study of the relations between appearances on T1 weighted images, T1 relaxation times, and metabolite concentrations. *J Neurol Neurosurg Psychiatry*. 2000;68(5):627-32.

97. van Waesberghe JH, Kamphorst W, De Groot CJ, van Walderveen MA, Castelijns JA, Ravid R, et al. Axonal loss in multiple sclerosis lesions: magnetic resonance imaging insights into substrates of disability. *Ann Neurol.* 1999;46(5):747-54.
98. van Walderveen MA, Kamphorst W, Scheltens P, van Waesberghe JH, Ravid R, Valk J, et al. Histopathologic correlate of hypointense lesions on T1-weighted spin-echo MRI in multiple sclerosis. *Neurology.* 1998;50(5):1282-8.
99. van Walderveen MA, Barkhof F, Pouwels PJ, van Schijndel RA, Polman CH, Castelijns JA. Neuronal damage in T1-hypointense multiple sclerosis lesions demonstrated in vivo using proton magnetic resonance spectroscopy. *Ann Neurol.* 1999;46(1):79-87.
100. Wallace CJ, Seland TP, Fong TC. Multiple sclerosis: the impact of MR imaging. *AJR Am J Roentgenol.* 1992;158(4):849-57.
101. Bastianello S, Bozzao A, Paolillo A, Giugni E, Gasperini C, Koudriavtseva T, et al. Fast spin-echo and fast fluid-attenuated inversion-recovery versus conventional spin-echo sequences for MR quantification of multiple sclerosis lesions. *AJNR Am J Neuroradiol.* 1997;18(4):699-704.
102. Jackson A, Sheppard S, Laitt RD, Kassner A, Moriarty D. Optic neuritis: MR imaging with combined fat- and water-suppression techniques. *Radiology.* 1998;206(1):57-63.
103. Filippi M, Horsfield MA, Hajnal JV, Narayana PA, Udupa JK, Yousry TA, et al. Quantitative assessment of magnetic resonance imaging lesion load in multiple sclerosis. *J Neurol Neurosurg Psychiatry.* 1998;64 Suppl 1:S88-93.
104. Koopmans RA, Li DK, Grochowski E, Cutler PJ, Paty DW. Benign versus chronic progressive multiple sclerosis: magnetic resonance imaging features. *Ann Neurol.* 1989;25(1):74-81.
105. Thompson AJ, Kermode AG, Wicks D, MacManus DG, Kendall BE, Kingsley DP, et al. Major differences in the dynamics of primary and secondary progressive multiple sclerosis. *Ann Neurol.* 1991;29(1):53-62.
106. Fazekas F, Barkhof F, Filippi M. Unenhanced and enhanced magnetic resonance imaging in the diagnosis of multiple sclerosis. *J Neurol Neurosurg Psychiatry.* 1998;64 Suppl 1:S2-5.
107. Morrissey SP, Stodal H, Zettl U, Simonis C, Jung S, Kiefer R, et al. In vivo MRI and its histological correlates in acute adoptive transfer experimental allergic encephalomyelitis. Quantification of inflammation and oedema. *Brain.* 1996;119 ( Pt 1):239-48.
108. Namer IJ, Steibel J, Piddlesden SJ, Mohr M, Poulet P, Chambron J. Magnetic resonance imaging of antibody-mediated demyelinating experimental allergic encephalomyelitis. *J Neuroimmunol.* 1994;54(1-2):41-50.
109. Capra R, Marciànò N, Vignolo LA, Chiesa A, Gasparotti R. Gadolinium-pentetic acid magnetic resonance imaging in patients with relapsing remitting multiple sclerosis. *Arch Neurol.* 1992;49(7):687-9.
110. McFarland HF, Frank JA, Albert PS, Smith ME, Martin R, Harris JO, et al. Using gadolinium-enhanced magnetic resonance imaging lesions to monitor disease activity in multiple sclerosis. *Ann Neurol.* 1992;32(6):758-66.
111. Thompson AJ, Miller D, Youl B, MacManus D, Moore S, Kingsley D, et al. Serial gadolinium-enhanced MRI in relapsing/remitting multiple sclerosis of varying disease duration. *Neurology.* 1992;42(1):60-3.
112. Barkhof F, Scheltens P, Frequin ST, Nauta JJ, Tas MW, Valk J, et al. Relapsing-remitting multiple sclerosis: sequential enhanced MR imaging vs clinical findings in determining disease activity. *AJR Am J Roentgenol.* 1992;159(5):1041-7.
113. Guttmann CR, Ahn SS, Hsu L, Kikinis R, Jolesz FA. The evolution of multiple sclerosis lesions on serial MR. *AJNR Am J Neuroradiol.* 1995;16(7):1481-91.
114. Harris JO, Frank JA, Patronas N, McFarlin DE, McFarland HF. Serial gadolinium-enhanced magnetic resonance imaging scans in patients with early, relapsing-remitting

- multiple sclerosis: implications for clinical trials and natural history. *Ann Neurol.* 1991;29(5):548-55.
115. Kermodé AG, Tofts PS, Thompson AJ, MacManus DG, Rudge P, Kendall BE, et al. Heterogeneity of blood-brain barrier changes in multiple sclerosis: an MRI study with gadolinium-DTPA enhancement. *Neurology.* 1990;40(2):229-35.
  116. Grossman RI, Gonzalez-Scarano F, Atlas SW, Galetta S, Silberberg DH. Multiple sclerosis: gadolinium enhancement in MR imaging. *Radiology.* 1986;161(3):721-5.
  117. Campi A, Filippi M, Comi G, Scotti G, Gerevini S, Dousset V. Magnetisation transfer ratios of contrast-enhancing and nonenhancing lesions in multiple sclerosis. *Neuroradiology.* 1996;38(2):115-9.
  118. He J, Grossman RI, Ge Y, Mannon LJ. Enhancing patterns in multiple sclerosis: evolution and persistence. *AJNR Am J Neuroradiol.* 2001;22(4):664-9.
  119. Bakshi R, Minagar A, Jaisani Z, Wolinsky JS. Imaging of multiple sclerosis: role in neurotherapeutics. *NeuroRx.* 2005;2(2):277-303.
  120. Thompson AJ, Kermodé AG, MacManus DG, Kendall BE, Kingsley DP, Moseley IF, et al. Patterns of disease activity in multiple sclerosis: clinical and magnetic resonance imaging study. *BMJ.* 1990;300(6725):631-4.
  121. Revesz T, Kidd D, Thompson AJ, Barnard RO, McDonald WI. A comparison of the pathology of primary and secondary progressive multiple sclerosis. *Brain.* 1994;117 ( Pt 4):759-65.
  122. Koudriavtseva T, Thompson AJ, Fiorelli M, Gasperini C, Bastianello S, Bozzao A, et al. Gadolinium enhanced MRI predicts clinical and MRI disease activity in relapsing-remitting multiple sclerosis. *J Neurol Neurosurg Psychiatry.* 1997;62(3):285-7.
  123. Smith ME, Stone LA, Albert PS, Frank JA, Martin R, Armstrong M, et al. Clinical worsening in multiple sclerosis is associated with increased frequency and area of gadopentetate dimeglumine-enhancing magnetic resonance imaging lesions. *Ann Neurol.* 1993;33(5):480-9.
  124. Silver NC, Good CD, Barker GJ, MacManus DG, Thompson AJ, Moseley IF, et al. Sensitivity of contrast enhanced MRI in multiple sclerosis. Effects of gadolinium dose, magnetization transfer contrast and delayed imaging. *Brain.* 1997;120 ( Pt 7):1149-61.
  125. Filippi M, Yousry T, Rocca MA, Fesl G, Voltz R, Comi G. Sensitivity of delayed gadolinium-enhanced MRI in multiple sclerosis. *Acta Neurol Scand.* 1997;95(6):331-4.
  126. Filippi M, Yousry T, Campi A, Kandziora C, Colombo B, Voltz R, et al. Comparison of triple dose versus standard dose gadolinium-DTPA for detection of MRI enhancing lesions in patients with MS. *Neurology.* 1996;46(2):379-84.
  127. Filippi M, Capra R, Campi A, Colombo B, Prandini F, Marciandò N, et al. Triple dose of gadolinium-DTPA and delayed MRI in patients with benign multiple sclerosis. *J Neurol Neurosurg Psychiatry.* 1996;60(5):526-30.
  128. Filippi M, Rovaris M, Capra R, Gasperini C, Yousry TA, Sormani MP, et al. A multi-centre longitudinal study comparing the sensitivity of monthly MRI after standard and triple dose gadolinium-DTPA for monitoring disease activity in multiple sclerosis. Implications for phase II clinical trials. *Brain.* 1998;121 ( Pt 10):2011-20.
  129. Bastianello S, Gasperini C, Paolillo A, Giugni E, Ciccarelli O, Sormani MP, et al. Sensitivity of enhanced MR in multiple sclerosis: effects of contrast dose and magnetization transfer contrast. *AJNR Am J Neuroradiol.* 1998;19(10):1863-7.
  130. Petrella JR, Grossman RI, McGowan JC, Campbell G, Cohen JA. Multiple sclerosis lesions: relationship between MR enhancement pattern and magnetization transfer effect. *AJNR Am J Neuroradiol.* 1996;17(6):1041-9.
  131. van Waesberghe JH, Castelijns JA, Roser W, Silver N, Yousry T, Lycklama à Nijeholt GJ, et al. Single-dose gadolinium with magnetization transfer versus triple-dose gadolinium

- in the MR detection of multiple sclerosis lesions. *AJNR Am J Neuroradiol.* 1997;18(7):1279-85.
132. Young IR, Hall AS, Pallis CA, Legg NJ, Bydder GM, Steiner RE. Nuclear magnetic resonance imaging of the brain in multiple sclerosis. *Lancet.* 1981;2(8255):1063-6.
  133. Runge VM, Price AC, Kirshner HS, Allen JH, Partain CL, James AE. The evaluation of multiple sclerosis by magnetic resonance imaging. *Radiographics.* 1986;6(2):203-12.
  134. Barkhof F, Filippi M, Miller DH, Scheltens P, Campi A, Polman CH, et al. Comparison of MRI criteria at first presentation to predict conversion to clinically definite multiple sclerosis. *Brain.* 1997;120 ( Pt 11):2059-69.
  135. Fazekas F, Offenbacher H, Fuchs S, Schmidt R, Niederkorn K, Horner S, et al. Criteria for an increased specificity of MRI interpretation in elderly subjects with suspected multiple sclerosis. *Neurology.* 1988;38(12):1822-5.
  136. Paty DW, Oger JJ, Kastrukoff LF, Hashimoto SA, Hooge JP, Eisen AA, et al. MRI in the diagnosis of MS: a prospective study with comparison of clinical evaluation, evoked potentials, oligoclonal banding, and CT. *Neurology.* 1988;38(2):180-5.
  137. McDonald WI, Compston A, Edan G, Goodkin D, Hartung HP, Lublin FD, et al. Recommended diagnostic criteria for multiple sclerosis: guidelines from the International Panel on the diagnosis of multiple sclerosis. *Ann Neurol.* 2001;50(1):121-7.
  138. Polman CH, Reingold SC, Edan G, Filippi M, Hartung HP, Kappos L, et al. Diagnostic criteria for multiple sclerosis: 2005 revisions to the "McDonald Criteria". *Ann Neurol.* 2005;58(6):840-6.
  139. Thompson AJ, Banwell BL, Barkhof F, Carroll WM, Coetzee T, Comi G, et al. Diagnosis of multiple sclerosis: 2017 revisions of the McDonald criteria. *Lancet Neurol.* 2018;17(2):162-73.
  140. van der Vurst de Vries RM, Mescheriakova JY, Wong YYM, Runia TF, Jafari N, Samijn JP, et al. Application of the 2017 Revised McDonald Criteria for Multiple Sclerosis to Patients With a Typical Clinically Isolated Syndrome. *JAMA Neurol.* 2018;75(11):1392-8.
  141. Bloomgren G, Richman S, Hotermans C, Subramanyam M, Goelz S, Natarajan A, et al. Risk of natalizumab-associated progressive multifocal leukoencephalopathy. *N Engl J Med.* 2012;366(20):1870-80.
  142. Essig M, Shiroishi MS, Nguyen TB, Saake M, Provenzale JM, Enterline D, et al. Perfusion MRI: the five most frequently asked technical questions. *AJR Am J Roentgenol.* 2013;200(1):24-34.
  143. Østergaard L. Principles of cerebral perfusion imaging by bolus tracking. *J Magn Reson Imaging.* 2005;22(6):710-7.
  144. Petersen ET, Zimine I, Ho YC, Golay X. Non-invasive measurement of perfusion: a critical review of arterial spin labelling techniques. *Br J Radiol.* 2006;79(944):688-701.
  145. MacDonald ME, Frayne R. Cerebrovascular MRI: a review of state-of-the-art approaches, methods and techniques. *NMR Biomed.* 2015;28(7):767-91.
  146. Lapointe E, Li DKB, Traboulsee AL, Rauscher A. What Have We Learned from Perfusion MRI in Multiple Sclerosis? *AJNR Am J Neuroradiol.* 2018;39(6):994-1000.
  147. Boxerman JL, Hamberg LM, Rosen BR, Weisskoff RM. MR contrast due to intravascular magnetic susceptibility perturbations. *Magn Reson Med.* 1995;34(4):555-66.
  148. Weisskoff RM, Zuo CS, Boxerman JL, Rosen BR. Microscopic susceptibility variation and transverse relaxation: theory and experiment. *Magn Reson Med.* 1994;31(6):601-10.
  149. Ge Y, Law M, Johnson G, Herbert J, Babb JS, Mannon LJ, et al. Dynamic susceptibility contrast perfusion MR imaging of multiple sclerosis lesions: characterizing hemodynamic impairment and inflammatory activity. *AJNR Am J Neuroradiol.* 2005;26(6):1539-47.
  150. Inglese M, Adhya S, Johnson G, Babb JS, Miles L, Jaggi H, et al. Perfusion magnetic resonance imaging correlates of neuropsychological impairment in multiple sclerosis. *J Cereb Blood Flow Metab.* 2008;28(1):164-71.

151. Peruzzo D, Castellaro M, Calabrese M, Veronese E, Rinaldi F, Bernardi V, et al. Heterogeneity of cortical lesions in multiple sclerosis: an MRI perfusion study. *J Cereb Blood Flow Metab.* 2013;33(3):457-63.
152. Wuerfel J, Bellmann-Strobl J, Brunecker P, Aktas O, McFarland H, Villringer A, et al. Changes in cerebral perfusion precede plaque formation in multiple sclerosis: a longitudinal perfusion MRI study. *Brain.* 2004;127(Pt 1):111-9.
153. Lassmann H. The pathologic substrate of magnetic resonance alterations in multiple sclerosis. *Neuroimaging Clin N Am.* 2008;18(4):563-76, ix.
154. Haselhorst R, Kappos L, Bilecen D, Scheffler K, Möri D, Radü EW, et al. Dynamic susceptibility contrast MR imaging of plaque development in multiple sclerosis: application of an extended blood-brain barrier leakage correction. *J Magn Reson Imaging.* 2000;11(5):495-505.
155. Li L, Chopp M, Nejad-Davarani SP, Jafari-Khouzani K, Patel SC, Budaj J, et al. Perfusion and Diffusion Abnormalities of Multiple Sclerosis Lesions and Relevance of Classified Lesions to Disease Status. *J Neurol Neurophysiol.* 2014;2014(Suppl 12):12.
156. Adhya S, Johnson G, Herbert J, Jaggi H, Babb JS, Grossman RI, et al. Pattern of hemodynamic impairment in multiple sclerosis: dynamic susceptibility contrast perfusion MR imaging at 3.0 T. *Neuroimage.* 2006;33(4):1029-35.
157. Debernard L, Melzer TR, Van Stockum S, Graham C, Wheeler-Kingshott CA, Dalrymple-Alford JC, et al. Reduced grey matter perfusion without volume loss in early relapsing-remitting multiple sclerosis. *J Neurol Neurosurg Psychiatry.* 2014;85(5):544-51.
158. Law M, Saindane AM, Ge Y, Babb JS, Johnson G, Mannon LJ, et al. Microvascular abnormality in relapsing-remitting multiple sclerosis: perfusion MR imaging findings in normal-appearing white matter. *Radiology.* 2004;231(3):645-52.
159. Narayana PA, Zhou Y, Hasan KM, Datta S, Sun X, Wolinsky JS. Hypoperfusion and T1-hypointense lesions in white matter in multiple sclerosis. *Mult Scler.* 2014;20(3):365-73.
160. Steen C, D'haeseleer M, Hoogduin JM, Fierens Y, Cambron M, Mostert JP, et al. Cerebral white matter blood flow and energy metabolism in multiple sclerosis. *Mult Scler.* 2013;19(10):1282-9.
161. Rashid W, Parkes LM, Ingle GT, Chard DT, Toosy AT, Altmann DR, et al. Abnormalities of cerebral perfusion in multiple sclerosis. *J Neurol Neurosurg Psychiatry.* 2004;75(9):1288-93.
162. Doche E, Lecocq A, Maarouf A, Duhamel G, Soulier E, Confort-Gouny S, et al. Hypoperfusion of the thalamus is associated with disability in relapsing remitting multiple sclerosis. *J Neuroradiol.* 2017;44(2):158-64.
163. Inglese M, Park SJ, Johnson G, Babb JS, Miles L, Jaggi H, et al. Deep gray matter perfusion in multiple sclerosis: dynamic susceptibility contrast perfusion magnetic resonance imaging at 3 T. *Arch Neurol.* 2007;64(2):196-202.
164. Ota M, Sato N, Nakata Y, Ito K, Kamiya K, Maikusa N, et al. Abnormalities of cerebral blood flow in multiple sclerosis: a pseudocontinuous arterial spin labeling MRI study. *Magn Reson Imaging.* 2013;31(6):990-5.
165. Varga AW, Johnson G, Babb JS, Herbert J, Grossman RI, Inglese M. White matter hemodynamic abnormalities precede sub-cortical gray matter changes in multiple sclerosis. *J Neurol Sci.* 2009;282(1-2):28-33.
166. Papadaki EZ, Mastorodemos VC, Amanakis EZ, Tsekouras KC, Papadakis AE, Tsavalas ND, et al. White matter and deep gray matter hemodynamic changes in multiple sclerosis patients with clinically isolated syndrome. *Magn Reson Med.* 2012;68(6):1932-42.
167. Amann M, Achtnichts L, Hirsch JG, Naegelin Y, Gregori J, Weier K, et al. 3D GRASE arterial spin labelling reveals an inverse correlation of cortical perfusion with the white matter lesion volume in MS. *Mult Scler.* 2012;18(11):1570-6.

168. Bester M, Forkert ND, Stellmann JP, Stürner K, Aly L, Drabik A, et al. Increased perfusion in normal appearing white matter in high inflammatory multiple sclerosis patients. *PLoS One*. 2015;10(3):e0119356.
169. Feys P, Lamers I, Francis G, Benedict R, Phillips G, LaRocca N, et al. The Nine-Hole Peg Test as a manual dexterity performance measure for multiple sclerosis. *Mult Scler*. 2017;23(5):711-20.
170. Hyland M, Rudick RA. Challenges to clinical trials in multiple sclerosis: outcome measures in the era of disease-modifying drugs. *Curr Opin Neurol*. 2011;24(3):255-61.
171. Zhong G, Lou M. Multimodal imaging findings in normal-appearing white matter of leucoaraiosis: a review. *Stroke Vasc Neurol*. 2016;1(2):59-63.
172. Varatharaj A, Galea I. The blood-brain barrier in systemic inflammation. *Brain Behav Immun*. 2017;60:1-12.
173. Barnes SR, Ng TS, Montagne A, Law M, Zlokovic BV, Jacobs RE. Optimal acquisition and modeling parameters for accurate assessment of low Ktrans blood-brain barrier permeability using dynamic contrast-enhanced MRI. *Magn Reson Med*. 2016;75(5):1967-77.
174. Patlak CS, Blasberg RG, Fenstermacher JD. Graphical evaluation of blood-to-brain transfer constants from multiple-time uptake data. *J Cereb Blood Flow Metab*. 1983;3(1):1-7.
175. Tofts PS. Modeling tracer kinetics in dynamic Gd-DTPA MR imaging. *J Magn Reson Imaging*. 1997;7(1):91-101.
176. Brix G, Kiessling F, Lucht R, Darai S, Wasser K, Delorme S, et al. Microcirculation and microvasculature in breast tumors: pharmacokinetic analysis of dynamic MR image series. *Magn Reson Med*. 2004;52(2):420-9.
177. Jelescu IO, Leppert IR, Narayanan S, Araújo D, Arnold DL, Pike GB. Dual-temporal resolution dynamic contrast-enhanced MRI protocol for blood-brain barrier permeability measurement in enhancing multiple sclerosis lesions. *J Magn Reson Imaging*. 2011;33(6):1291-300.
178. Silver NC, Tofts PS, Symms MR, Barker GJ, Thompson AJ, Miller DH. Quantitative contrast-enhanced magnetic resonance imaging to evaluate blood-brain barrier integrity in multiple sclerosis: a preliminary study. *Mult Scler*. 2001;7(2):75-82.
179. Kwon EE, Prineas JW. Blood-brain barrier abnormalities in longstanding multiple sclerosis lesions. An immunohistochemical study. *J Neuropathol Exp Neurol*. 1994;53(6):625-36.
180. Zhang CE, Wong SM, Uiterwijk R, Backes WH, Jansen JFA, Jeukens CRLP, et al. Blood-brain barrier leakage in relation to white matter hyperintensity volume and cognition in small vessel disease and normal aging. *Brain Imaging Behav*. 2019;13(2):389-95.
181. Xiong H, Yin P, Li X, Yang C, Zhang D, Huang X, et al. The features of cerebral permeability and perfusion detected by dynamic contrast-enhanced magnetic resonance imaging with Patlak model in relapsing-remitting multiple sclerosis. *Ther Clin Risk Manag*. 2019;15:233-40.
182. Yin P, Xiong H, Liu Y, Sah SK, Zeng C, Wang J, et al. Measurement of the permeability, perfusion, and histogram characteristics in relapsing-remitting multiple sclerosis using dynamic contrast-enhanced MRI with extended Tofts linear model. *Neurol India*. 2018;66(3):709-15.
183. Lund H, Krakauer M, Skimminge A, Sellebjerg F, Garde E, Siebner HR, et al. Blood-brain barrier permeability of normal appearing white matter in relapsing-remitting multiple sclerosis. *PLoS One*. 2013;8(2):e56375.
184. Cramer SP, Modvig S, Simonsen HJ, Frederiksen JL, Larsson HB. Permeability of the blood-brain barrier predicts conversion from optic neuritis to multiple sclerosis. *Brain*. 2015;138(Pt 9):2571-83.

185. Varatharaj A, Liljeroth M, Darekar A, Larsson HBW, Galea I, Cramer SP. Blood-brain barrier permeability measured using dynamic contrast-enhanced magnetic resonance imaging: a validation study. *J Physiol*. 2019;597(3):699-709.
186. Armitage PA, Farrall AJ, Carpenter TK, Doubal FN, Wardlaw JM. Use of dynamic contrast-enhanced MRI to measure subtle blood-brain barrier abnormalities. *Magn Reson Imaging*. 2011;29(3):305-14.
187. van de Haar HJ, Jansen JFA, Jeukens CRLP, Burgmans S, van Buchem MA, Muller M, et al. Subtle blood-brain barrier leakage rate and spatial extent: Considerations for dynamic contrast-enhanced MRI. *Med Phys*. 2017;44(8):4112-25.
188. Gaitán MI, Shea CD, Evangelou IE, Stone RD, Fenton KM, Bielekova B, et al. Evolution of the blood-brain barrier in newly forming multiple sclerosis lesions. *Ann Neurol*. 2011;70(1):22-9.
189. Soon D, Tozer D, Altmann D, Tofts P, Miller D. Quantification of subtle blood-brain barrier disruption in non-enhancing lesions in multiple sclerosis: a study of disease and lesion subtypes. *Mult Scler*. 2007;13(7):884-94.
190. Shinohara RT, Crainiceanu CM, Caffo BS, Gaitán MI, Reich DS. Population-wide principal component-based quantification of blood-brain-barrier dynamics in multiple sclerosis. *Neuroimage*. 2011;57(4):1430-46.
191. Jackson A, O'Connor JP, Parker GJ, Jayson GC. Imaging tumor vascular heterogeneity and angiogenesis using dynamic contrast-enhanced magnetic resonance imaging. *Clin Cancer Res*. 2007;13(12):3449-59.
192. Øvrebø KM, Hompland T, Mathiesen B, Rofstad EK. Assessment of hypoxia and radiation response in intramuscular experimental tumors by dynamic contrast-enhanced magnetic resonance imaging. *Radiother Oncol*. 2012;102(3):429-35.
193. Li X, Zhu Y, Kang H, Zhang Y, Liang H, Wang S, et al. Glioma grading by microvascular permeability parameters derived from dynamic contrast-enhanced MRI and intratumoral susceptibility signal on susceptibility weighted imaging. *Cancer Imaging*. 2015;15:4.
194. De Naeyer D, Verhulst J, Ceelen W, Segers P, De Deene Y, Verdonck P. Flip angle optimization for dynamic contrast-enhanced MRI-studies with spoiled gradient echo pulse sequences. *Phys Med Biol*. 2011;56(16):5373-95.
195. Kershaw LE, Cheng HL. Temporal resolution and SNR requirements for accurate DCE-MRI data analysis using the AATH model. *Magn Reson Med*. 2010;64(6):1772-80.
196. Aerts HJ, van Riel NA, Backes WH. System identification theory in pharmacokinetic modeling of dynamic contrast-enhanced MRI: influence of contrast injection. *Magn Reson Med*. 2008;59(5):1111-9.
197. Just N, Koh DM, D'Arcy J, Collins DJ, Leach MO. Assessment of the effect of haematocrit-dependent arterial input functions on the accuracy of pharmacokinetic parameters in dynamic contrast-enhanced MRI. *NMR Biomed*. 2011;24(7):902-15.
198. Heilmann M, Kiessling F, Enderlin M, Schad LR. Determination of pharmacokinetic parameters in DCE MRI: Consequence of nonlinearity between contrast agent concentration and signal intensity. *Invest Radiol*. 2006;41(6):536-43.
199. Dale BM, Jesberger JA, Lewin JS, Hillenbrand CM, Duerk JL. Determining and optimizing the precision of quantitative measurements of perfusion from dynamic contrast enhanced MRI. *J Magn Reson Imaging*. 2003;18(5):575-84.
200. Ordidge RJ, Gibbs P, Chapman B, Stehling MK, Mansfield P. High-speed multislice T1 mapping using inversion-recovery echo-planar imaging. *Magn Reson Med*. 1990;16(2):238-45.
201. Henderson E, McKinnon G, Lee TY, Rutt BK. A fast 3D look-locker method for volumetric T1 mapping. *Magn Reson Imaging*. 1999;17(8):1163-71.

202. Cheng HL, Wright GA. Rapid high-resolution T(1) mapping by variable flip angles: accurate and precise measurements in the presence of radiofrequency field inhomogeneity. *Magn Reson Med*. 2006;55(3):566-74.
203. Yuan J, Chow SK, Yeung DK, Ahuja AT, King AD. Quantitative evaluation of dual-flip-angle T1 mapping on DCE-MRI kinetic parameter estimation in head and neck. *Quant Imaging Med Surg*. 2012;2(4):245-53.
204. Yang X, Liang J, Heverhagen JT, Jia G, Schmalbrock P, Sammet S, et al. Improving the pharmacokinetic parameter measurement in dynamic contrast-enhanced MRI by use of the arterial input function: theory and clinical application. *Magn Reson Med*. 2008;59(6):1448-56.
205. Parker GJ, Roberts C, Macdonald A, Buonaccorsi GA, Cheung S, Buckley DL, et al. Experimentally-derived functional form for a population-averaged high-temporal-resolution arterial input function for dynamic contrast-enhanced MRI. *Magn Reson Med*. 2006;56(5):993-1000.
206. Larsson HB, Stubgaard M, Frederiksen JL, Jensen M, Henriksen O, Paulson OB. Quantitation of blood-brain barrier defect by magnetic resonance imaging and gadolinium-DTPA in patients with multiple sclerosis and brain tumors. *Magn Reson Med*. 1990;16(1):117-31.
207. Hansen AE, Pedersen H, Rostrup E, Larsson HB. Partial volume effect (PVE) on the arterial input function (AIF) in T1-weighted perfusion imaging and limitations of the multiplicative rescaling approach. *Magn Reson Med*. 2009;62(4):1055-9.
208. Peeters F, Annet L, Hermoye L, Van Beers BE. Inflow correction of hepatic perfusion measurements using T1-weighted, fast gradient-echo, contrast-enhanced MRI. *Magn Reson Med*. 2004;51(4):710-7.
209. Zhang JL, Rusinek H, Bokacheva L, Chen Q, Storey P, Lee VS. Use of cardiac output to improve measurement of input function in quantitative dynamic contrast-enhanced MRI. *J Magn Reson Imaging*. 2009;30(3):656-65.
210. Lüdemann L, Wust P, Gellermann J. Perfusion measurement using DCE-MRI: implications for hyperthermia. *Int J Hyperthermia*. 2008;24(1):91-6.
211. Fedorov A, Fluckiger J, Ayers GD, Li X, Gupta SN, Tempny C, et al. A comparison of two methods for estimating DCE-MRI parameters via individual and cohort based AIFs in prostate cancer: a step towards practical implementation. *Magn Reson Imaging*. 2014;32(4):321-9.
212. Loveless ME, Halliday J, Liess C, Xu L, Dortch RD, Whisenant J, et al. A quantitative comparison of the influence of individual versus population-derived vascular input functions on dynamic contrast enhanced-MRI in small animals. *Magn Reson Med*. 2012;67(1):226-36.
213. Weinmann HJ, Laniado M, Mützel W. Pharmacokinetics of GdDTPA/dimeglumine after intravenous injection into healthy volunteers. *Physiol Chem Phys Med NMR*. 1984;16(2):167-72.
214. Kovar DA, Lewis M, Karczmar GS. A new method for imaging perfusion and contrast extraction fraction: input functions derived from reference tissues. *J Magn Reson Imaging*. 1998;8(5):1126-34.
215. Yang C, Karczmar GS, Medved M, Stadler WM. Estimating the arterial input function using two reference tissues in dynamic contrast-enhanced MRI studies: fundamental concepts and simulations. *Magn Reson Med*. 2004;52(5):1110-7.
216. Yang C, Karczmar GS, Medved M, Stadler WM. Multiple reference tissue method for contrast agent arterial input function estimation. *Magn Reson Med*. 2007;58(6):1266-75.
217. Spanakis M, Marias K. In silico evaluation of gadofosveset pharmacokinetics in different population groups using the Simcyp® simulator platform. *In Silico Pharmacol*. 2014;2(1):2.

218. Rowland M, Balant L, Peck C. Physiologically based pharmacokinetics in drug development and regulatory science: a workshop report (Georgetown University, Washington, DC, May 29-30, 2002). *AAPS PharmSci.* 2004;6(1):E6.
219. Barboriak DP, MacFall JR, Viglianti BL, Dewhirst Dvm MW. Comparison of three physiologically-based pharmacokinetic models for the prediction of contrast agent distribution measured by dynamic MR imaging. *J Magn Reson Imaging.* 2008;27(6):1388-98.
220. Spanakis M, Sakkalis V, Marias K. Application of Simcyp® simulator platform for the assessment of the pharmacokinetic profile of Gd-DOTA regarding its disposition in brain tumors lesions with different vasculature. 24th Annual Meeting of the Population Approach Group in Europe (PAGE2015).
221. Spanakis M, Sakkalis V, Marias K. Application of Simcyp simulator platform for the assessment of the pharmacokinetic profile of Gd-DOTA regarding its disposition in brain tumors lesions with different vasculature. 24th Annual Meeting of the Population Approach Group in Europe (PAGE2015).
222. Tofts PS, Brix G, Buckley DL, Evelhoch JL, Henderson E, Knopp MV, et al. Estimating kinetic parameters from dynamic contrast-enhanced T(1)-weighted MRI of a diffusible tracer: standardized quantities and symbols. *J Magn Reson Imaging.* 1999;10(3):223-32.
223. Bergamino M, Bonzano L, Levrero F, Mancardi GL, Roccatagliata L. A review of technical aspects of T1-weighted dynamic contrast-enhanced magnetic resonance imaging (DCE-MRI) in human brain tumors. *Phys Med.* 2014;30(6):635-43.
224. Sourbron SP, Buckley DL. On the scope and interpretation of the Tofts models for DCE-MRI. *Magn Reson Med.* 2011;66(3):735-45.
225. St Lawrence KS, Lee TY. An adiabatic approximation to the tissue homogeneity model for water exchange in the brain: I. Theoretical derivation. *J Cereb Blood Flow Metab.* 1998;18(12):1365-77.
226. Johnson JA, Wilson TA. A model for capillary exchange. *Am J Physiol.* 1966;210(6):1299-303.
227. Zhou J, Wilson DA, Ulatowski JA, Traystman RJ, van Zijl PC. Two-compartment exchange model for perfusion quantification using arterial spin tagging. *J Cereb Blood Flow Metab.* 2001;21(4):440-55.
228. Koh TS, Zeman V, Darko J, Lee TY, Milosevic MF, Haider M, et al. The inclusion of capillary distribution in the adiabatic tissue homogeneity model of blood flow. *Phys Med Biol.* 2001;46(5):1519-38.
229. Jain RK. Determinants of tumor blood flow: a review. *Cancer Res.* 1988;48(10):2641-58.
230. Schabel MC. A unified impulse response model for DCE-MRI. *Magn Reson Med.* 2012;68(5):1632-46.
231. Brix G, Ravesh MS, Zwick S, Griebel J, Delorme S. On impulse response functions computed from dynamic contrast-enhanced image data by algebraic deconvolution and compartmental modeling. *Phys Med.* 2012;28(2):119-28.
232. Kim JK, Hong SS, Choi YJ, Park SH, Ahn H, Kim CS, et al. Wash-in rate on the basis of dynamic contrast-enhanced MRI: usefulness for prostate cancer detection and localization. *J Magn Reson Imaging.* 2005;22(5):639-46.
233. Preziosi P, Orlacchio A, Di Giambattista G, Di Renzi P, Bortolotti L, Fabiano A, et al. Enhancement patterns of prostate cancer in dynamic MRI. *Eur Radiol.* 2003;13(5):925-30.
234. Padhani AR, Gapinski CJ, Macvicar DA, Parker GJ, Suckling J, Revell PB, et al. Dynamic contrast enhanced MRI of prostate cancer: correlation with morphology and tumour stage, histological grade and PSA. *Clin Radiol.* 2000;55(2):99-109.
235. Eyal E, Degani H. Model-based and model-free parametric analysis of breast dynamic-contrast-enhanced MRI. *NMR Biomed.* 2009;22(1):40-53.

236. Jolliffe IT, Cadima J. Principal component analysis: a review and recent developments. *Philos Trans A Math Phys Eng Sci.* 2016;374(2065):20150202.
237. Bell AJ, Sejnowski TJ. An information-maximization approach to blind separation and blind deconvolution. *Neural Comput.* 1995;7(6):1129-59.
238. Lucht RE, Knopp MV, Brix G. Classification of signal-time curves from dynamic MR mammography by neural networks. *Magn Reson Imaging.* 2001;19(1):51-7.
239. Levman J, Leung T, Causer P, Plewes D, Martel AL. Classification of dynamic contrast-enhanced magnetic resonance breast lesions by support vector machines. *IEEE Trans Med Imaging.* 2008;27(5):688-96.
240. Fritz-Hansen T, Rostrup E, Larsson HB, Søndergaard L, Ring P, Henriksen O. Measurement of the arterial concentration of Gd-DTPA using MRI: a step toward quantitative perfusion imaging. *Magn Reson Med.* 1996;36(2):225-31.
241. Bergamino M, Saitta L, Barletta L, Bonzano L, Mancardi GL, Castellani L, et al. Measurement of blood-brain barrier permeability with t1-weighted dynamic contrast-enhanced MRI in brain tumors: a comparative study with two different algorithms. *ISRN Neurosci.* 2013;2013:905279.
242. Ferlay J, Soerjomataram I, Dikshit R, Eser S, Mathers C, Rebelo M, et al. Cancer incidence and mortality worldwide: sources, methods and major patterns in GLOBOCAN 2012. *Int J Cancer.* 2015;136(5):E359-86.
243. Liu SV, Melstrom L, Yao K, Russell CA, Sener SF. Neoadjuvant therapy for breast cancer. *J Surg Oncol.* 2010;101(4):283-91.
244. Clark K, Vendt B, Smith K, Freymann J, Kirby J, Koppel P, et al. The Cancer Imaging Archive (TCIA): maintaining and operating a public information repository. *J Digit Imaging.* 2013;26(6):1045-57.
245. Li X, Abramson RG, Arlinghaus LR, Kang H, Chakravarthy AB, Abramson VG, et al. Multiparametric magnetic resonance imaging for predicting pathological response after the first cycle of neoadjuvant chemotherapy in breast cancer. *Invest Radiol.* 2015;50(4):195-204.
246. Li X, Abramson RG, Arlinghaus LR, Chakravarthy AB, Abramson VG, Sanders M, et al. Data From QIN-Breast [Data set]. The Cancer Imaging Archive 2016 [Data set].
247. Kontopodis E, George MV, Katerina N, Maria V, Kostas M, Thomas MG, et al. Incremental diagnostic information obtained via novel Dynamic Contrast Enhanced MRI framework applied on Multiple Sclerosis patients: a preliminary study. 2018 IEEE EMBS International Conference on Biomedical & Health Informatics (BHI)2018.
248. Sataloff DM, Mason BA, Prestipino AJ, Seinige UL, Lieber CP, Baloch Z. Pathologic response to induction chemotherapy in locally advanced carcinoma of the breast: a determinant of outcome. *J Am Coll Surg.* 1995;180(3):297-306.
249. Kontopodis E, Karatzanis I, Sakkalis V, Buffa F, Marias K, editors. A DCE analysis workflow. *Proceedings of the 33rd Computer Graphics International; 2016; Heraklion, Greece: ACM New York.*
250. Li X, Arlinghaus LR, Ayers GD, Chakravarthy AB, Abramson RG, Abramson VG, et al. DCE-MRI analysis methods for predicting the response of breast cancer to neoadjuvant chemotherapy: pilot study findings. *Magn Reson Med.* 2014;71(4):1592-602.
251. Jenkinson M, Bannister P, Brady M, Smith S. Improved optimization for the robust and accurate linear registration and motion correction of brain images. *Neuroimage.* 2002;17(2):825-41.
252. Jenkinson M, Smith S. A global optimisation method for robust affine registration of brain images. *Med Image Anal.* 2001;5(2):143-56.
253. Spiess AN, Neumeyer N. An evaluation of R2 as an inadequate measure for nonlinear models in pharmacological and biochemical research: a Monte Carlo approach. *BMC Pharmacol.* 2010;10:6.
254. Ezekiel M. *Methods of correlation analysis.* Wiley; 1941.

255. Loch-Neckel G, Koeppe J. [The blood-brain barrier and drug delivery in the central nervous system]. *Rev Neurol*. 2010;51(3):165-74.
256. Kirk J, Plumb J, Mirakhur M, McQuaid S. Tight junctional abnormality in multiple sclerosis white matter affects all calibres of vessel and is associated with blood-brain barrier leakage and active demyelination. *J Pathol*. 2003;201(2):319-27.
257. Vos CM, Geurts JJ, Montagne L, van Haastert ES, Bö L, van der Valk P, et al. Blood-brain barrier alterations in both focal and diffuse abnormalities on postmortem MRI in multiple sclerosis. *Neurobiol Dis*. 2005;20(3):953-60.
258. Bae J, Zhang J, Wadghiri YZ, Minhas AS, Poptani H, Ge Y, et al. Measurement of blood-brain barrier permeability using dynamic contrast-enhanced magnetic resonance imaging with reduced scan time. *Magn Reson Med*. 2018;80(4):1686-96.
259. Rao SM, Leo GJ, Bernardin L, Unverzagt F. Cognitive dysfunction in multiple sclerosis. I. Frequency, patterns, and prediction. *Neurology*. 1991;41(5):685-91.
260. Panou T, Mastorodemos V, Papadaki E, Simos PG, Plaitakis A. Early signs of memory impairment among multiple sclerosis patients with clinically isolated syndrome. *Behav Neurol*. 2012;25(4):311-26.
261. Benedict RH, Weinstock-Guttman B, Fishman I, Sharma J, Tjoa CW, Bakshi R. Prediction of neuropsychological impairment in multiple sclerosis: comparison of conventional magnetic resonance imaging measures of atrophy and lesion burden. *Arch Neurol*. 2004;61(2):226-30.
262. Papadaki EZ, Simos PG, Mastorodemos VC, Panou T, Maris TG, Karantanas AH, et al. Regional MRI perfusion measures predict motor/executive function in patients with clinically isolated syndrome. *Behav Neurol*. 2014;2014:252419.
263. Papadaki EZ, Simos PG, Panou T, Mastorodemos VC, Maris TG, Karantanas AH, et al. Hemodynamic evidence linking cognitive deficits in clinically isolated syndrome to regional brain inflammation. *Eur J Neurol*. 2014;21(3):499-505.
264. Pinter D, Khalil M, Pichler A, Langkammer C, Ropele S, Marschik PB, et al. Predictive value of different conventional and non-conventional MRI-parameters for specific domains of cognitive function in multiple sclerosis. *Neuroimage Clin*. 2015;7:715-20.
265. Feuillet L, Reuter F, Audoin B, Malikova I, Barrau K, Cherif AA, et al. Early cognitive impairment in patients with clinically isolated syndrome suggestive of multiple sclerosis. *Mult Scler*. 2007;13(1):124-7.
266. Pelosi L, Geesken JM, Holly M, Hayward M, Blumhardt LD. Working memory impairment in early multiple sclerosis. Evidence from an event-related potential study of patients with clinically isolated myelopathy. *Brain*. 1997;120 ( Pt 11):2039-58.
267. Achiron A, Barak Y. Cognitive impairment in probable multiple sclerosis. *J Neurol Neurosurg Psychiatry*. 2003;74(4):443-6.
268. Feinstein A, Kartsounis LD, Miller DH, Youl BD, Ron MA. Clinically isolated lesions of the type seen in multiple sclerosis: a cognitive, psychiatric, and MRI follow up study. *J Neurol Neurosurg Psychiatry*. 1992;55(10):869-76.
269. Grant I, McDonald WI, Trimble MR, Smith E, Reed R. Deficient learning and memory in early and middle phases of multiple sclerosis. *J Neurol Neurosurg Psychiatry*. 1984;47(3):250-5.
270. Constantinidou F, Zaganas I, Papastefanakis E, Kasselimis D, Nidos A, Simos PG. Age-related decline in verbal learning is moderated by demographic factors, working memory capacity, and presence of amnesic mild cognitive impairment. *J Int Neuropsychol Soc*. 2014;20(8):822-35.
271. Zalonis I, Kararizou E, Triantafyllou NI, Kapaki E, Papageorgiou S, Sgouropoulos P, et al. A normative study of the trail making test A and B in Greek adults. *Clin Neuropsychol*. 2008;22(5):842-50.

272. Kosmidis MH, Vlahou CH, Panagiotaki P, Kiosseoglou G. The verbal fluency task in the Greek population: normative data, and clustering and switching strategies. *J Int Neuropsychol Soc.* 2004;10(2):164-72.
273. Simos PG PE, T Panou T, Kasselimis D, editor *The Greek memory scale.* Laboratory of Applied Psychology; 2011; Rethymno, Crete, Greece: University of Crete.
274. Michopoulos I, Douzenis A, Kalkavoura C, Christodoulou C, Michalopoulou P, Kalemi G, et al. Hospital Anxiety and Depression Scale (HADS): validation in a Greek general hospital sample. *Ann Gen Psychiatry.* 2008;7:4.
275. Geffen G GL. *Auditory Verbal Learning Test (AVLT): Computerised Scoring Program and Population Norms*2000.
276. Filippi M, Tortorella C, Rovaris M, Bozzali M, Possa F, Sormani MP, et al. Changes in the normal appearing brain tissue and cognitive impairment in multiple sclerosis. *J Neurol Neurosurg Psychiatry.* 2000;68(2):157-61.
277. Lund H, Jønsson A, Andresen J, Rostrup E, Paulson OB, Sørensen PS. Cognitive deficits in multiple sclerosis: correlations with T2 changes in normal appearing brain tissue. *Acta Neurol Scand.* 2012;125(5):338-44.
278. Iannucci G, Tortorella C, Rovaris M, Sormani MP, Comi G, Filippi M. Prognostic value of MR and magnetization transfer imaging findings in patients with clinically isolated syndromes suggestive of multiple sclerosis at presentation. *AJNR Am J Neuroradiol.* 2000;21(6):1034-8.
279. Saindane AM, Law M, Ge Y, Johnson G, Babb JS, Grossman RI. Correlation of diffusion tensor and dynamic perfusion MR imaging metrics in normal-appearing corpus callosum: support for primary hypoperfusion in multiple sclerosis. *AJNR Am J Neuroradiol.* 2007;28(4):767-72.